공학박사 학위논문

Efficient Vacuum-Deposited Organic Solar Cells by Novel Designs of Device Structures with Analysis of Working Mechanisms

새로운 소자구조 설계 및 구동원리 분석을 통한 고효율 진공증착 유기태양전지

2016년 2월

서울대학교 대학원

재료공학부 하이브리드재료전공

심 현 섭

Abstract

Efficient Vacuum-Deposited Organic Solar Cells by Novel Designs of Device Structures with Analysis of Working Mechanisms

Hyun-Sub Shim
Department of Materials Science and Engineering
The Graduate School
Seoul National University

Organic photovoltaics (OPVs) has shown large progress in the past several years. Unfortunately, however, the power conversion efficiency (PCE) is still lower than inorganic counterparts. One of the main reasons is the narrow absorption window of organic materials, which can only partially use solar photon flux. Therefore, extending the absorption into the near-infrared region is a critical factor to enhance device performance in OPVs. In this thesis, the novel designs of devices structures with analysis of their working mechanisms are reported to broaden spectral response to the solar photon flux.

The templating effect on the device performance is introduced using copper iodide (CuI) as a templating layer to control the crystal structure of lead phthalocyanine (PbPc). The templating layer inserted between ITO and the PbPc layer induces the increase of crystallinity with the preferred orientation and enhanced exciton

diffusion length of the PbPc molecules, resulting in the increased short circuit current density (J_{SC}). Moreover, Fill factor (FF) is also enhanced due to the better contact between ITO and the PbPc layer by insertion the templating layer. As the results, the absorption range of the device is extended into the wavelength of 1000 nm with almost twice enhancement of the PCE.

Tandem organic photovoltaics (TOPVs) having two identical sub-cells connected by the interconnection unit (ICU) are reported. The TOPVs can cover broad spectrum if the two sub-cells have complementary absorption. To realize efficient TOPVs, the ICU is the most important part because it affect device performance optically as well as electrically. The requirements of the ICU are transparency in the active region of the TOPVs to reduce optical losses, energy level alignment between two sub-cells to eliminate voltage losses and tunable thickness with electrical properties maintained for the current matching. New design of the ICU (electron-transporting layer/metal/*p*-doped hole-transporting layer) for the TOPVs is introduced, which fulfills all the requirements. Moreover, its working mechanisms are discussed with the analysis of the ICU by systematically varying the doping concentration of the *p*-HTL in the ICU. The difference between the Fermi level and the highest ocuupied molecular orbital (HOMO) level of the *p*-HTL is a key factor to influence the open circuit voltage (V_{OC}) in the TOPVs. The FF is related with the conductivity of the *p*-HTL and the depletion width at the interface between Ag and the *p*-HTL. The requirement of the *p*-HTL is also investigated. Dopants with higher charge generation efficiency results in higher V_{OC} due to the reduction of the difference between the Fermi level and the HOMO level of the *p*-HTL, and higher FF due to the efficient hole transport at the interface

between Ag and *p*-HTL through the tunneling process. Based on the understanding of the new ICU, efficient vacuum-deposited TOPVs, composed of pristine fullerenes as the acceptors and two complementary absorbing donors, 2-((2-(5-(4-(diphenylamino)phenyl)thieno[3,2-b] thiophen-2-yl)thiazol-5-yl)methylene)malononitrile (DTTz) for the visible absorption and 2-((7-(5-(dip-tolylamino)thiophen-2-yl)benzo[c]-[1,2,5]thiadiazol-4-yl)methylene)malononitrile (DTDCTB) for the near-infrared absorption, are realized. The PCE of 9.2% is achieved with higher FF of 0.62 than that of single-junction sub-cells (0.54, 0.57), J_{SC} of 8.7 mA cm^{-2} and V_{OC} of 1.71 V using 80 nm thick active layers in both sub-cells.

Another device concept of ternary blend OPVs to extend absorption of the active layer using two donors, DTTz for the visible absorption and DTDCTB for the near-infrared absorption, co-deposited with C_{70} in the ternary layer is reported. The PCE of 8.02% for the ternary device is achieved, which is 23% higher than that of the binary OPVs. This enhancement originates from incorporating two donors with the complementary absorption covering from the wavelength of 350 nm to 900 nm with higher hole mobility in the ternary layer than one of the binary layers consisting of one donor and C_{70}, combined with the energy transfer from the donor (DTTz) with lower hole mobility to the one with higher mobility (DTDCTB). This structure fulfills all the requirements for efficient ternary OPVs.

Keywords: organic solar cells, templating layer, interconnection units, tandem organic solar cells, ternary organic solar cells.

Student Number: 2010-22760

Contents

List of Tables

List of Figures

Chapter 1. Introduction

1.1 Introduction to organic solar cells

The rapid growth in the consumption of the energy requires to find alternative energy sources due to the limited quantity of resources, mainly fossil fuels, and environmental pollution. One of the alternatives is to use sun light, so called solar cells or photovoltaics (PVs), because it is an environmental-friendly process, no limitation of the place to set up and the use of a permanent resource. So far, inorganic PVs based on silicon or compound semiconductors such as GaAs are available in the commercial market. However, the fabrication process is relatively complicated and the number of materials to form PVs are limited, which means that it is difficult to develop device performance by replacing newly designed materials. To solve these problems, organic materials can be one of the best candidates because they are easy to form films by the spin-coating or thermal-vacuum evaporation and various types of molecular structure can be easily synthesized. Moreover, organic materials can be adopted in the flexible applications due to its flexibility.

In the past several years, organic photovoltaics (OPVs) have shown large progress since the first OPV was reported by C. W. Tang.[1] The power conversion efficiency (PCE) has reached up to ~10% for single donor-acceptor blended structure.[2-5] However, it is still lower than that of inorganic PVs. One of the main reasons is the narrow absorption window although the absorption coefficient is larger than inorganic materials. Figure 1.1 shows some examples of the absorption spectra of organic and inorganic materials.[6] Typically, organic materials have several

absorption peaks, corresponding to the transition of π-π* or charge transfer between

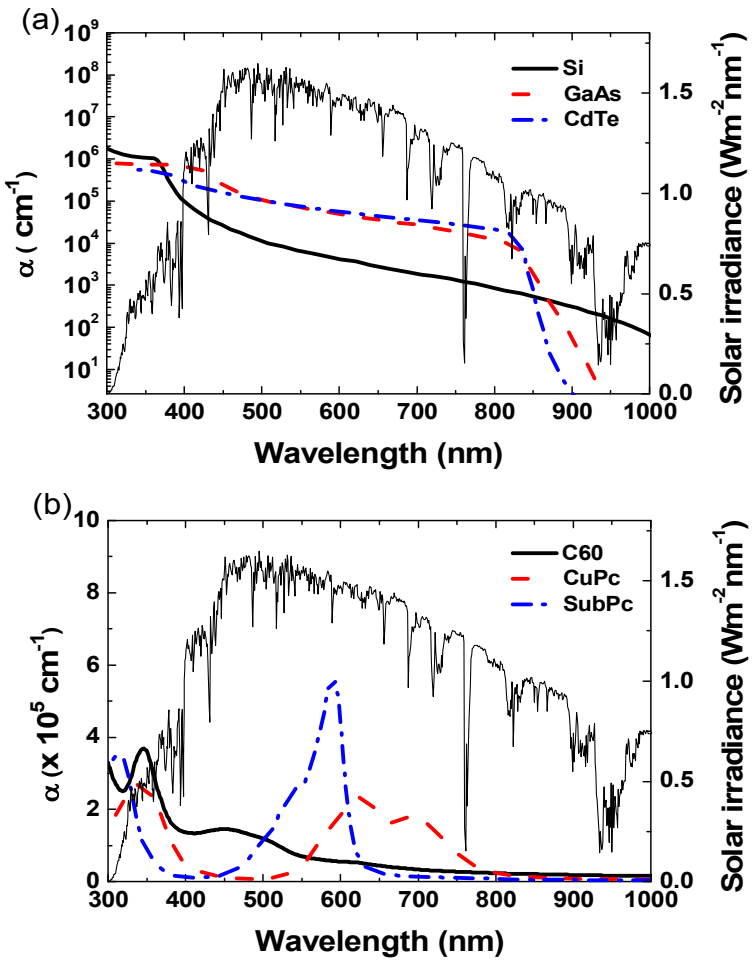

Figure 1.1 Absorption coefficient of (a) inorganic and (b) organic materials with solar irradiance

donor and acceptor unit in the molecules with narrow absorption band due to the discrete energy levels. On the other hands, inorganic materials has continuous absorption spectra at the wavelength over their band-gap due to the formation of the band structure. Therefore, the mismatch between the absorption of organic materials and solar irradiance results in reduced short-circuit current density (J_{SC}).

Various attempts have been made to enhance the J_{SC}, such as the synthesis of low-bandgap materials,[7-9] control of molecular orientation or crystal structure,[10-13] and development of device structures.[14-18] The absorption can be extended to near-infrared (NIR) region if the low-bandgap materials are used in the OPVs. However, open circuit voltage (V_{OC}) is reduced at the same time due to the lower highest occupied molecular orbital (HOMO) levels of the donor material in the OPVs. Another way to broaden or extend absorption into NIR region is to control the molecular orientation or crystal structure by heating,[19, 20] solvent annealing,[21, 22] and insertion of the templating layer.[11, 23] If the molecular transition dipole moment is matched with the electric field of the incident light, the absorption of the devices can be larger. Moreover, the absorption spectra can be extended into NIR due to the structural transition.

The device concepts of tandem or ternary blend OPVs have been widely studied with the same reasons.[14, 17, 18, 24] The tandem OPVs (TOPVs) consist of more than two identical sub-cells, which have similar structure to the single OPVs, connected by interconnection units (ICUs). In contrast, ternary blend OPVs have two donors or acceptors with an acceptor or donor in the active layer. Both concepts can efficiently use solar photon flux from UV to NIR region to generate the energy if materials having complementary absorptions are used in the sub-cells of TOPVs.

1.2 Principle of organic solar cells

1.2.1 Operation mechanism of organic solar cells

The working mechanism of OPVs is shown in Figure 1.2. The basic structure is similar to the p-n junction of inorganic semiconductors. The current generation from the absorption in the devices can be explained by four steps. (1) When the light comes into the device, tightly bound electron-hole pairs, so called exciton, are generated. The binding energy of excitons in organic materials is 0.3~0.5 eV, which is much higher than inorganic materials (~10 meV). Therefore, the generated excitons in the OPVs cannot be separated into free carrier directly. (2) The generated excitons diffuse to the interface between the donor and acceptor. To fully absorb solar photon flux, the thickness of the active layer should be over 100 nm. However, the thickness of the donor or acceptor layer in the planar heterojunction (PHJ), that is the sandwiched structure of the donor and acceptor layer, is 20-60 nm because the diffusion length of excitons in organic materials is only ~10 nm. The bulk heterojunction (BHJ), that is mixed layer of the donor and acceptor, is introduced to avoid this trade-off. (3) The generated excitons are dissociated into free carriers due to the energetic preference. The lowest unoccupied molecular orbital (LUMO) levels of the acceptor should be higher than that of the donor to form charge-transfer complex (CT complex). The driving force of the internal electric field is needed for the dissociation because the CT complex is still bounded by the Coulombic force. In the short-circuit condition, the built-in potential which is the difference of work functions between two electrodes facilitate the dissociation. (4) The dissociated charges are transported to the electrodes. In this

step, the electrical properties of the

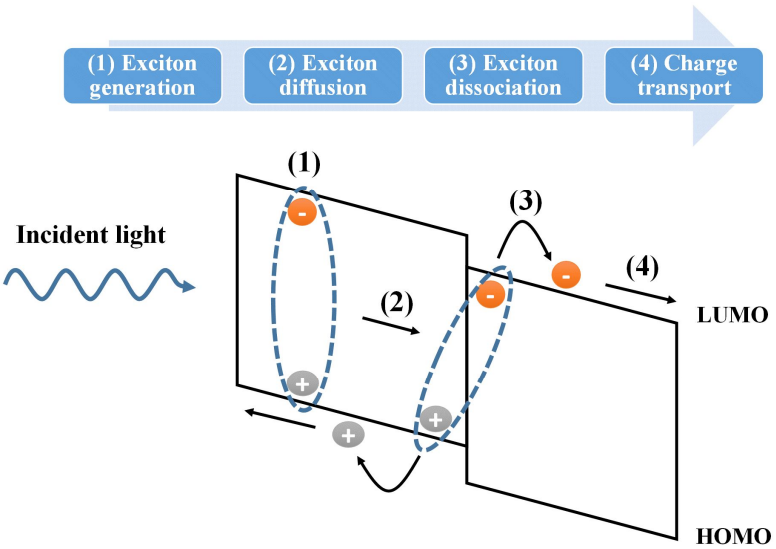

Figure 1.2 Schematic energy band diagram of organic solar cells with its working mechanism

active layer is important. If there are resistive sources, such as energetic barriers and traps, the charges cannot be transported and recombined without the contribution to the generation of the current.

1.2.2 Characterization of organic solar cells

The current density-voltage (*J-V*) characteristics is one of the common methods to evaluate the solar cell performance as shown in Figure 1.3. The behavior of the current under applying the voltage shows typical diode characteristics in the dark condition. Under the illumination of the light, the additional current is generated in the devices. The J_{SC} is the generated current at the zero bias where the built-in potential is the driving force. The V_{OC} is the maximum voltage available from the OPVs at the zero current. The V_{OC} is directly related to the difference between the HOMO level of the donor and the LUMO level of the acceptor. The maximum power (P_{Max}) is the product of the voltage and current density, indicating the maximum power obtainable from the devices. The fill factor (FF) is the ratio between P_{MAX} (grey area) and the product of J_{SC} and V_{OC} (the area of dashed line).

$$FF = \frac{P_{\mathrm{Max}}}{J_{\mathrm{SC}} V_{\mathrm{OC}}} \tag{1-1}$$

The PCE is defined as the ratio of the maximum output power from the device to the input power from the incident light (P_{in}).

$$PCE = \frac{P_{\mathrm{Max}}}{P_{\mathrm{in}}} = \frac{J_{\mathrm{SC}} V_{\mathrm{OC}} FF}{P_{\mathrm{in}}} \tag{1-2}$$

The incident photon-to-electron conversion efficiency (IPCE) represents how

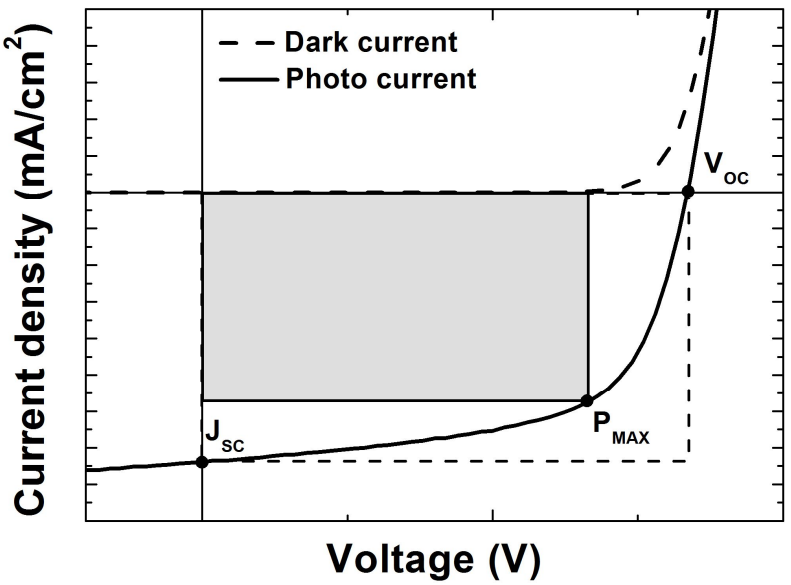

Figure 1.3 Typical current density-voltage characteristics of organic solar cells in the dark (dashed lines) and under light illumination (solid lines)

efficiently the device convert the incident light into the current at the certain wavelength, which is described by

$$IPCE = \frac{\#of\ generated\ electrons}{\#of\ incident\ photons} \tag{1-3}$$

The Shockley diode equation is commonly used to analyze the *J-V* characteristics of the OPVs.

$$J = J_S\left[\exp\left(\frac{V - JR_S}{nkT/q}\right) - 1\right] + \frac{V - JR_S}{R_P} - J_{ph} \tag{1-4}$$

where J_S, n, J_{ph} are the dark saturation current density, ideality factor and photo current respectively. The resistances of the device such, as the series (R_S) and parallel (R_P) resistances, also included in the equation. The R_S and R_P are related with the contact and bulk resistance and leakage current, respectively. In the ideal case, the R_S goes to zero and the R_P to infinite. In the real devices, however, the resistances exist due to the low mobility and energetic barriers between organic layers or organic layers and electrodes. Therefore, it is important to know the origin of the resistance in the devices. The quantity of the resistance of R_S and R_P can be obtained by fitting the Shockley diode equation with the dark current density of the devices.

1.3 Device structures of organic solar cells

1.3.1 Single junction structure

The first demonstration of the OPVs was the layer-by-layer structure of the donor and acceptor layers, so called the planar heterojunction (PHJ) as shown in Figure 1.4.[1] In this structure, the generated excitons by the absorption from the illuminated light should diffuse to the D/A interface to be dissociated. However, the diffusion length of the organic materials is very short with ~10 nm. Therefore, the thickness of the active layer is limited although the thick layer over ~100 nm is required to fully absorb solar spectra. To overcome this trade-off, the mixture of the donor and acceptor layers, so called the bulk heterojunction (BHJ) was suggested.[25] The generated excitons reach the D/A interfaces more easily than the PHJs due to the shorter distance to diffuse, resulting in the enhancement of the J_{SC}.

1.3.2 Tandem structure

The basic structure of TOPVs consists of two sub-cells connected by ICUs as shown in Figure 1.5. The absorption of the devices can be extended to NIR region from UV if the materials used in each sub-cell have the complementary absorption. In addition, the V_{OC} or J_{SC} can be larger up to the sum of each sub-cell if they are connected in the series or parallel configuration, respectively. One of the most important parts in the TOPVs is the design of the ICU where holes and electrons are recombined because it affects the device performance electrically and optically. A few requirements of the ICU needs to be fulfilled for efficient TOPVs. Firstly, it should be transparent in the absorption range of the sub-cells to avoid optical losses. Secondly, it should align the energy levels between sub-cells as shown in Figure

1.5b.

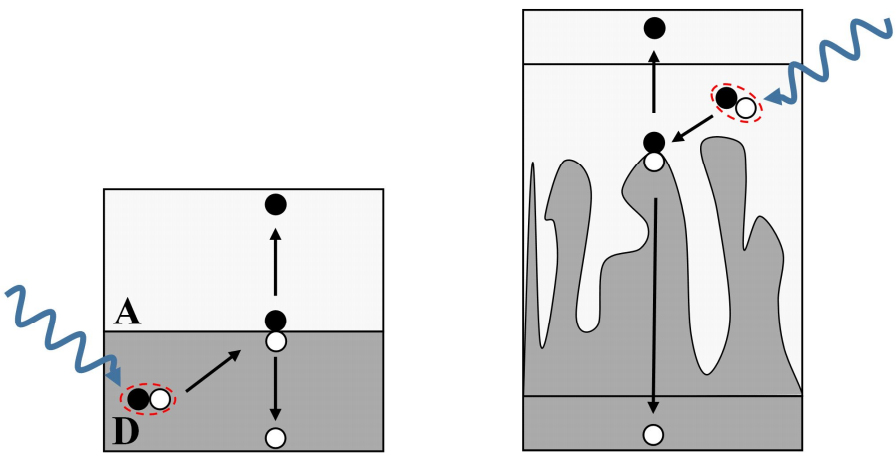

Figure 1.4 Schematic drawings of a planar structure (left side) and bulk-heterojunction (right side) organic solar cells. The regions of A and B represent the acceptor and donor layer, respectively. The generated excitons by the absorption of the light are dissociated at the interface of the donor and acceptor layer

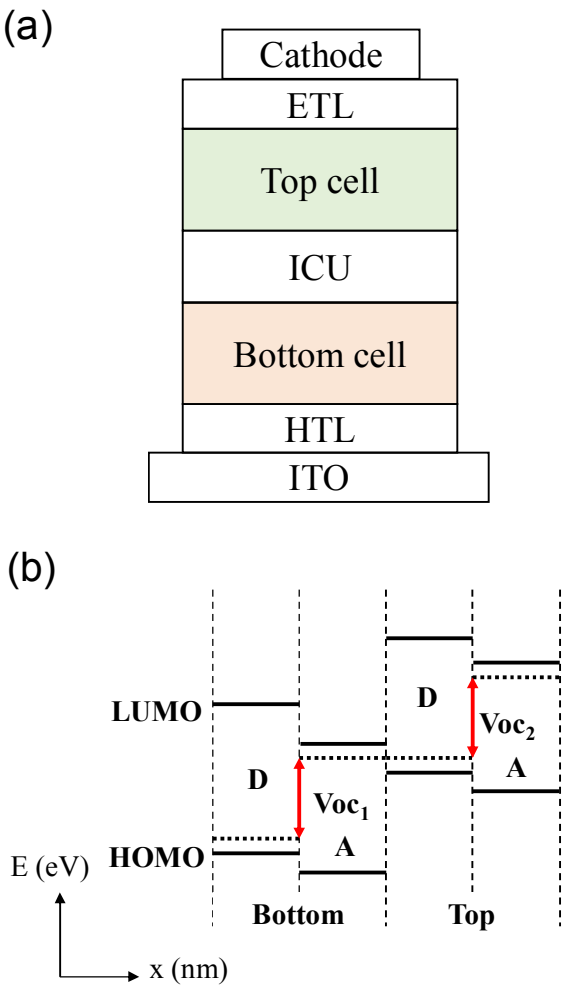

Figure 1.5 (a) Conventional device structure of tandem organic solar cells. (b) Schematic energy levels of tandem OPVs

If there is a voltage drop in the ICU, the V_{OC} of the TOPVs become much smaller than the sum of the V_{OC}s of the sub-cells. Moreover, the FF is reduced dramatically if there is an energetic barrier in the ICU. In addition, it should act as an optical spacer for matching the current level between sub-cells because the J_{SC} of the TOPVs is determined by the lower J_{SC} between sub-cells in the series connection. In the literature, two different structures (metal/metal oxide and *p-n* junction using *p*- and *n*-doped layers) have been used as the ICUs in the TOPVs fabricated by the vacuum deposition as shown in Figure 1.6.[14, 26] Each structure has shown the possibility to enhance the device performance of the TOPVs compared with single junction OPVs. However, they have disadvantages which might affect device negatively. The metal/metal oxide based ICU do not work properly as the optical spacer because the conductivity of the metal oxide is decreased with increasing its thickness, resulting in the reduction of the FF or J_{SC}. In the p-n junction based ICU, the diffusion of the n-dopant into the pre-deposited layers or instability of the dopants can be problems. Moreover, the absorption loss can occur in the ICU because the acceptor material needs to be used as a host in the *n*-doped layers for the efficient electron transport from the acceptor to the recombination contact. Therefore, new design of the ICU is required to fulfil all the requirements for efficient TOPVs.

1.3.3 Ternary blend structure

Another method to broaden absorption spectra of the OPVs is a ternary system which has two donors or acceptors in the active layer. This structure is much simpler than the tandem device because no additional layer, such as the ICU, is

needed for the device operation. However, it is more difficult to select proper materials because the

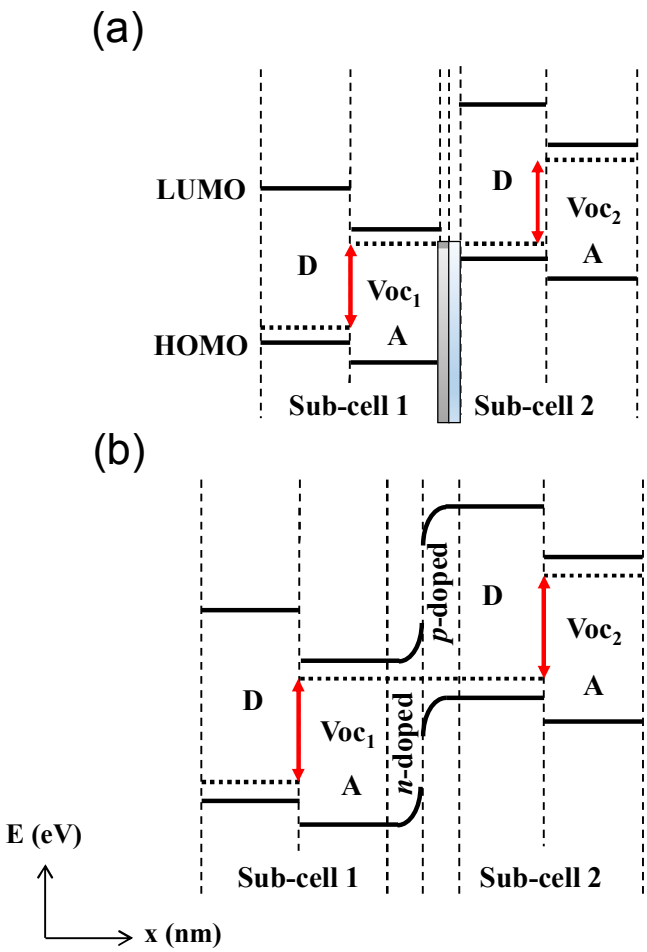

Figure 1.6 Schematic energy levels of tandem organic solar cells with the inter-connection units of (a) metal with metal oxide and (b) *p-n* junction

additional material in the active layer can induce negative effects such as forming trap sites induced by the interaction with other materials or energetic barriers due to the mismatch of the energy levels among the materials. Therefore, the selection of the materials is a key point in the Ternary OPVs. To improve the device performance in ternary OPVs compared to binary devices, a few requirements need to be fulfilled. Firstly, two donors or acceptors should have the complementary absorption to efficiently use solar photon flux with broad spectra. If the absorption overlap is large, the enhancement of the J_{SC} would be limited due to the optical losses. Secondly, cascade energy levels are needed to ensure efficient charge transports. If not, the charges can be trapped and recombined in the active layer due to the energetic barriers, resulting in the reduction of the J_{SC} and FF. In addition, the energy transfer to the molecules having higher mobility between two donors or acceptors in the ternary layer is favored to enhance electrical properties of the devices because charges can be transported to the electrode via the molecules with higher mobility.

1.4 Outline of thesis

The most important point to improve the device performance of the OPVs is to extend absorption of the active layer into the NIR region as mentioned in **chapter 1**. In this thesis, three different concepts are introduced with novel design and analysis of the device structure.

In **chapter 2**, the templating effect on the device performance is discussed using copper iodide (CuI) as a templating layer to control the crystal structure of lead phthalocyanine (PbPc). Devices with CuI inserted between the ITO and PbPc layers exhibit a two times enhancement of the J_{SC} compared to the case in the absence of the CuI layer. This is explained by the increase of crystallinity in the molecules grown on the CuI templating layer, which is investigated via an X-ray diffraction study. Moreover, fill factor is also enhanced to 0.63 from 0.57 due to low series resistance although the additional CuI layer is inserted between the ITO and the PbPc layer. As a result, the corrected power conversion efficiency of 2.5% was obtained, which is the highest one reported up to now among the PbPc based solar cells.

In **chapter 3**, new design of the ICU (electron-transporting layer/metal/*p*-doped hole-transporting layer) for the TOPVs is introduced. The ICU satisfies all the requirements of optical transparency and low voltage loss and for functioning as an optical spacer. The variation of the J_{SC} and V_{OC} of the TOPV cells with increasing thickness of the *p*-HTL in the ICU followed the theoretical predictions, proving that the ICU does not disturb the electrical characteristics of the TOPV cells up to a *p*-HTL thickness of 100 nm with minimal V_{OC} loss (~3%).

More detailed analysis of the ICU by systematically varying the doping

concentration of the *p*-HTL in the ICU is performed in **chapter 4**. The V_{OC} is significantly increased as the doping concentration of the *p*-HTL increases due to the reduction of the difference between the Fermi level and the HOMO level of the *p*-HTL. The FF is also enhanced with increases in the doping concentration of the *p*-HTL due to the enhancement of the conductivity in the *p*-HTL and efficient hole transport at the interface between Ag and the *p*-HTL through the tunneling process, rather than through the thermionic process.

In **chapter 5**, the effect of different *p*-dopants (ReO_3, MoO_3 and CuI) used in the ICU on the performance of the TOPVs is investigated. Dopants with higher charge generation efficiency resulted in higher V_{OC} due to the reduction of the difference between the Fermi level and the HOMO level of the *p*-HTL, and higher FF due to the efficient hole transport at the interface between Ag and *p*-HTL through the tunneling process.

Based on the understanding of the new ICU, efficient vacuum-deposited TOPVs, composed of pristine fullerenes as the acceptors and two complementary absorbing donors, 2-((2-(5-(4-(diphenylamino)phenyl)thieno[3,2-b] thiophen-2-yl)thiazol-5-yl)methylene)malononitrile for the visible absorption and 2-((7-(5-(dip-tolylamino)thiophen-2-yl)benzo[c]-[1,2,5]thiadiazol-4-yl) methylene)malononitrile for the near-infrared absorption, are fabricated in **chapter 6**. Two sub-cells are connected by the ICU composed of electron-transporting layer/metal/*p*-doped hole-transporting layer. The *p*-doped layer in the ICU enables increasing the J_{SC} of the TOPVs by tuning the relative position of sub-cells in the tandem devices to have the maximum optical field distribution response, which is well matched with theoretical calculation. Moreover, the introduction of the doped layer benefits to

the higher FF of the consisting sub-cells without losing V_{OC} even with the thick active layers. As a result, the PCE of 9.2% is achieved with higher FF of 0.62 than that of single-junction sub-cells (0.54, 0.57), J_{SC} of 8.7 mA cm^{-2}, and V_{OC} of 1.71 V using 80 nm thick active layers in both sub-cells.

Another device concept of ternary blend OPVs to extend absorption of the active layer using two donors, DTTz for the visible absorption and DTDCTB for the near-infrared absorption, co-deposited with C_{70} in the ternary layer is discussed in **chapter 7**. The PCE of 8.02% for the ternary device is achieved, which is 23% higher than that of the binary OPVs. This enhancement originates from incorporating two donors with the complementary absorption covering from the wavelength of 350 nm to 900 nm with higher hole mobility in the ternary layer than one of the binary layers consisting of one donor and C_{70}, combined with the energy transfer from the donor (DTTz) with lower hole mobility to the one with higher mobility (DTDCTB). This structure fulfills all the requirements for efficient ternary OPVs.

Chapter 2. Enhancement of near-infrared absorption with high fill factor in lead phthalocyanine-based organic solar cells

2.1 Introduction

Organic photovoltaics (OPVs) show lower power conversion efficiencies (PCEs) compared with inorganic solar cells. One of the reasons is the limited absorption matching of active materials in OPVs with solar spectra. Over 60% of the total solar photon flux is located at wavelengths greater than 600 nm, with 50% in the red and near-infrared (NIR) spectra (600–1000 nm), where organic materials exhibit a low absorption coefficient, resulting in a low short circuit current (J_{SC}).[27] To overcome this problem, new organic materials sensitive to the NIR spectrum, or processing techniques for extending the absorption to the NIR spectrum, are required to efficiently convert the solar photon flux into current. In tandem applications, for instance, long-range absorption from wavelengths of 300 nm to 1000 nm can be achieved when one of the cells is sensitive to the NIR spectrum.

Lead phthalocyanine (PbPc) has been used in OPVs due to its high absorption coefficient in the NIR region, and it is also a good candidate for tandem applications.[28-31] PbPc has two peaks in the red and NIR regions located at the wavelengths of 740 nm and 900 nm, related to the amorphous or the monoclinic phases, and the triclinic phases, respectively. Therefore, the formation of the triclinic phases and increasing the crystallinity are critical factors for PbPc to enhance its NIR absorption. Two methods have been reported to form the triclinic phase. One method is to control the deposition conditions such as the film

thickness, evaporation rate, substrate temperature, and the materials of substrate or post-thermal annealing of the deposited film.[32-34] This method was applied to PbPc based planar heterojunction solar cells to get the significantly enhanced J_{SC}.[20] Since a thick layer is required to increase the triclinic phase in the film by the method, a relatively thick (~40 nm) layer was used in the solar cells. Unfortunately, the thick layer leads to the lowering of the fill factor (FF) probably due to the low hole mobility in the film.[35] The other method to control the crystal structures is by using templating layers such as oxovanadium phthalocyanine (VOPc), sexithiophene (6T), para-sexiphenylene (p-6P), copper phthalocyanine (CuPc), zinc phthalocyanine (ZnPc), and pentacene between the ITO and PbPc layer.[28, 36, 37] This method can enlarge J_{SC} due to the structural change of the PbPc layer, resulting in the enhancement of the NIR absorption using a thin PbPc layer (~20 to 30 nm). This method supplements the drawbacks of controlling the evaporation conditions. Especially for tandem applications, increasing the temperature for structural control can negatively affect previously evaporated layers, resulting in a degradation of the solar cell performance. Unfortunately, FF is reduced in the solar cells even with the thin PbPc layer probably due to the increased series resistance coming from the templating interfacial layers. Up to now there are few reports of increasing the J_{SC} and FF at the same time using the methods to the best of our knowledge. We need a templating layer which can increase the triclinic phase in the film without increasing the series resistance to obtain enhanced J_{SC} and FF at the same time. Here, we report enhanced J_{SC} and FF at the same time using copper iodide (CuI) as the interfacial layer between the ITO and the PbPc layer to control the crystal structures of PbPc and to form Ohmic contact with ITO in planar heterojunction

solar cells with C_{60} used as an acceptor. CuI leads the PbPc layer to a more crystalline formation, so that J_{SC}, FF, and power conversion efficiency (PCE) are remarkably enhanced, from 4.6 mA cm^{-2} to 8.9 mA cm^{-2} (solar spectrum corrected J_{SC} of 8.7 mA cm^{-2}), 0.57 to 0.63 and 1.3% to 2.6% (solar spectrum corrected PCE of 2.5%), respectively, without changing any fabricating conditions such as the film thickness, evaporation rate, substrate temperature, and additional processes. The corrected PCE is the highest one reported up to now among the PbPc based solar cells to the best of our knowledge. CuI was first introduced as a *p*-dopant in organic light emitting diodes by our group.[38] Recently, CuI was also used as an interfacial layer in planar heterojunction solar cells, leading to a significant enhancement of the solar cell performance. Planar-shaped copper phthalocyanine molecules have been used in the devices.[39] However, CuI has not been applied in the non-planar-shaped phthalocyanines to control the crystal structure, especially, for the purpose of enhancing the NIR absorption.

2.2 Experimental

To fabricate the devices discussed here, CuI, BCP (purchased from Lumtec), PbPc (purchased from Jilin OLED Optoelectronic Materials Co.), and C_{60} (purchased from SES Research) were used without performing any purification process before use. The devices have the structure of ITO/(CuI)/PbPc/C_{60}/BCP/Al. All the materials were thermally evaporated under a base pressure of $<10^{-7}$ Torr on ITO pre-coated glass substrates which were cleaned with acetone and isopropyl alcohol, and exposed to UV-O_3 for 10 min before use. The evaporation rate was 1 Å s^{-1} for all the organic materials except for CuI (0.1 Å s^{-1}). The UV-vis absorption spectra

of the films were recorded with a VARIAN Cary 5000 UV-vis spectrophotometer. The current density-voltage (*J-V*) characteristics were measured under AM 1.5G solar simulator illumination (Oriel, 91160), and recorded with a Keithley 237 source measurement unit. The light intensity was calibrated to the wavelength of 650 nm by using a standard Si-solar cell with KG-5 filter. In the IPCE set up, a 1000 W Xe lamp was used with a monochromator and its intensity was calibrated with a Si photodiode. The IPCE data were used to correct the measured J_{SC} using the AM1.5G solar spectrum. More than 4 devices with the cell area of 2x2 mm^2 were averaged to calculate the cell performance. X-ray diffraction (XRD) measurements were performed on a D8 Advance diffractometer (Bruker) using Cu Kα radiation. PbPc was deposited on the CuI film to investigate the structural changes of the PbPc. The reference data were used in the analysis of the peak position of the monoclinic and triclinic phases.[20]

2.3 Results and Discussion

Figure 2.1 shows the absorption coefficient of PbPc as a function of the PbPc thickness on the quartz substrate and on the CuI layer (0.5 nm) inserted between the quartz substrate and the PbPc layer. The absorption peaks are located at λ=350 nm and 740 nm in the 20-nm-thick PbPc film deposited on the substrate without the CuI layer. Above a thickness of 20 nm, the absorption shoulder appears at a wavelength of 900 nm, which increases with increasing PbPc thickness. This is due to the increase of the triclinic phase which is dependent on the thickness.[20] In the CuI inserted film, however, the absorption shoulder at around a wavelength of 900 nm is dramatically enhanced more than twice compared to the film in the absence

of CuI, although the thickness of the PbPc is only 20 nm. This indicates that only the 0.5-nm-thick CuI affects the formation of the PbPc crystal structures regardless of the

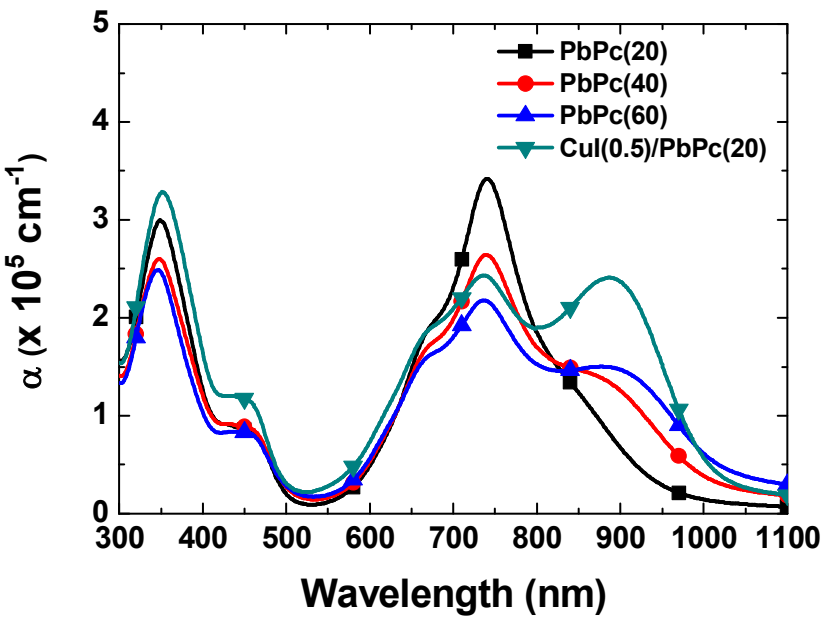

Figure 2.1 The absorption coefficient as a function of the PbPc thickness with and without the CuI templating layer deposited on the glass. The thickness is indicated in the brackets.

PbPc thickness.

Figure 2.2a displays the *J-V* characteristics of an ITO/PbPc(20 nm)/C_{60}(40 nm)/BCP (8 nm)/Al(100 nm) PV cell, and an ITO/CuI(0.5 nm)/PbPc(20 nm)/C_{60}(40 nm)/BCP (8 nm)/Al (100 nm) PV cell. Table 2.1 summarizes the solar cell performance of J_{SC} open circuit voltage (V_{OC}), FF, and PCE. The series resistance (R_S) and parallel resistance (R_P) obtained by fitting the dark *J-V* curve with the Shockley diode equation are also indicated. The PV cell without the CuI templating layer shows comparably high FF up to 0.57 which is consistent with previous reports.[20] This result is originated from the low R_S of 2.4 Ω cm^2, indicating that good electric contact between the ITO and the PbPc layer is formed. Under the condition of AM 1.5G illumination, J_{SC} is dramatically enhanced from 4.6 mA cm^{-2} to 8.6 mA cm^{-2} using CuI as the templating layer. FF is also enhanced from 0.57 to 0.62. Therefore, PCE significantly increases up to 2.5% in the CuI using device, from 1.3% in the absence of CuI (See Table 2.1). The enhanced FF indicates that the electrical contact between the ITO and the PbPc layer is not deteriorated by the CuI layer. The incident-photon-to-electron conversion efficiency (IPCE) of the OPV with and without the CuI templating layer is also measured as shown in Figure 2.2b. The IPCE remarkably increases from an excitation wavelength of 500 nm to 1100 nm. An IPCE result of 28.7% was obtained in the CuI-inserted OPV at the excitation wavelength of 732 nm, compared to 18.6% for the OPV without the CuI buffer layer. However, even more importantly, the IPCE at the excitation wavelength of 900 nm is 4.8 timeshigher, with an increase from 5.9% to 28.8%, when using the CuI templating layer. The IPCE data were used to correct J_{SC} using the AM1.5G solar spectrum. The resulting

J_{SC} of the CuI-inserted OPV was 8.4 mA cm^{-2}, resulting in the corrected PCE of 2.4%.

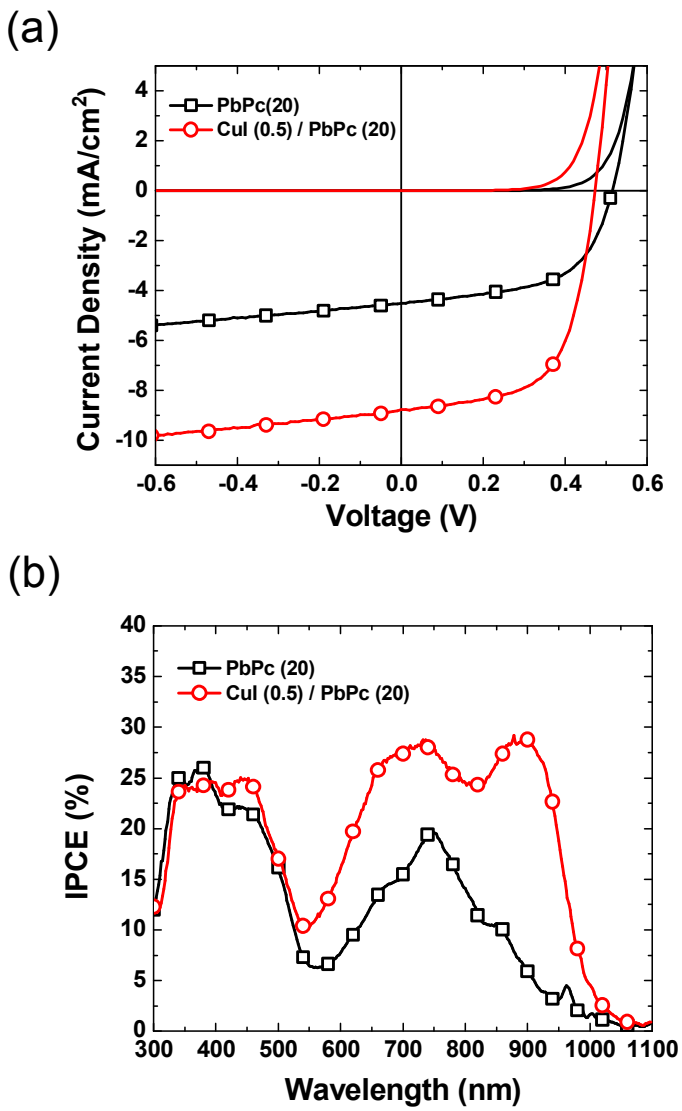

Figure 2.2 (a) The *J–V* characteristics with and without the CuI templating layer under AM 1.5G illumination. The device structures are ITO/PbPc (20 nm)/C_{60} (40 nm)/BCP (8 nm)/Al and ITO/CuI (0.5 nm)/PbPc (20 nm)/C_{60} (40 nm)/BCP (8 nm)/Al. (b) The IPCE data for the devices from (a)

Table 2.1 The solar cell performance with and without the CuI templating layer. Series resistance (R_S), and parallel resistance (R_P) are obtained by fitting the dark *J-V* curve with the Shockley diode equation. The corrected J_{SC} are obtained by integrating the IPCE spectrum of the cells with the standard AM 1.5G spectrum for a representative one in each structure.

	Measured PCE (%)	Corrected PCE (%)	Measured J_{SC} (mA/cm^2)	Corrected J_{SC} (mA/cm^2)	FF	V_{OC} (V)	R_S (Ωcm^2)	R_P (10^5 Ωcm^2)
PbPc (20)	1.34 ± 0.01	1.41	4.57 ± 0.06	4.86	0.57	0.51	2.40	5.16
CuI (0.5)/PbPc (20)	2.54 ± 0.04	2.44	8.61 ± 0.14	8.39	0.62	0.47	2.40	7.32
CuI (0.5)/PbPc (30)	2.58 ± 0.02	2.51	8.85 ± 0.04	8.67	0.63	0.46	1.94	10.94

The PCE is the highest among the PbPc based OPVs reported up to now to our best knowledge. It is worth noting that the difference between the measured and corrected J_{SC} is rather small in our measurements.

The performance of OPV cells depends on morphology and crystalline structure of consisting materials even in small molecule based solar cells.[40-43] In order to investigate the crystalline phase of PbPc deposited on the CuI templating layer, XRD measurements were performed as shown in Figure 2.3. Vasseur *et al.* showed that the diffraction peak positions of 12.12°, 12.35°, and 12.52° represent the triclinic (020), triclinic (11-1), and monoclinic (320) peaks, respectively. Moreover, 16.49°, 16.52°, and 16.64° correspond to the triclinic structures whose reflection planes are (11-2), (1-30), and (2-21), respectively.[20] All the films have no diffraction peaks under 11°, and over 18°. The low intense diffraction peak is measured at 12.47° in the 20-nm-thick film on ITO pre-coated glass, indicating that the film is composed of an amorphous phase and a monoclinic phase. In contrast, an additional diffraction peak is obtained at 16.4° when the thickness of the PbPc on ITO pre-coated glass is 50 nm, implying that a triclinic phase is additionally formed. This is in consistent with the previously reported result that the portion of triclinic increases with increasing thickness in the PbPc films.[20] However, the 20-nm-thick PbPc film grown on the CuI layer shows no peak at around 16.4°. All of the films have a diffraction peak at around 12.45°, representing the triclinic phase with the reflection plane of (11-1) or the monoclinic phase with the reflection plane of (320). In this case, it is difficult to distinguish between the monoclinic and triclinic phases due to the close peak positions. However, it is certain that the CuI acts as a template for the PbPc

molecules so that they have a preferred orientation. Most importantly, the full width

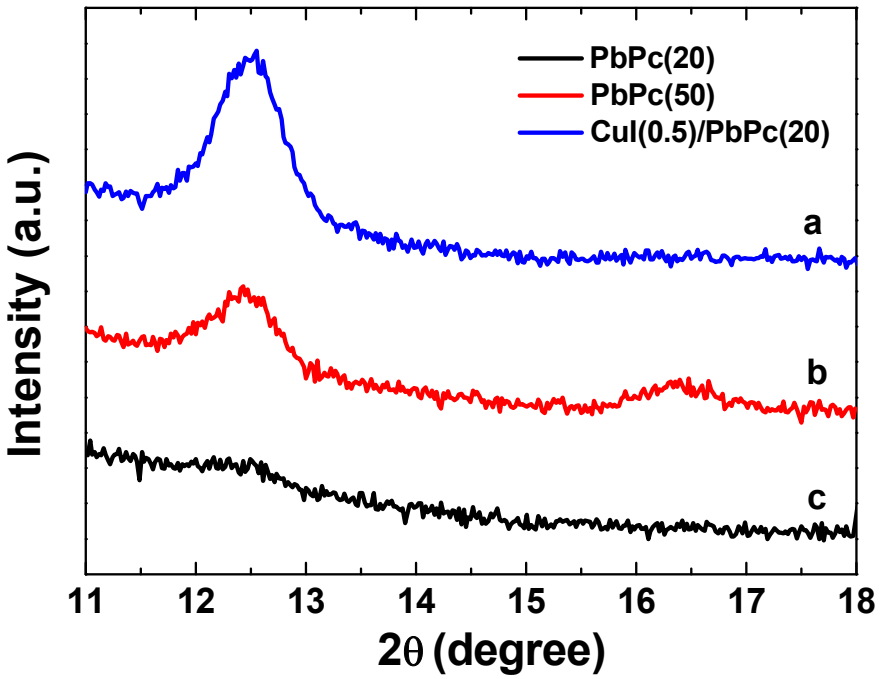

Figure 2.3 The X-ray diffraction profiles of (a) CuI (0.5 nm)/PbPc (20 nm), (b) PbPc (50 nm), and (c) PbPc (20 nm) deposited on the ITO pre-coated glass

at half maximum (FWHM) values are 1.03º, 0.72º, and 0.73º, when the thicknesses of the PbPc layer are 20 nm and 50 nm on ITO pre-coated glass, and 20 nm on CuI, corresponding to crystallite sizes of 7.7 nm, 11.01 nm, and 10.82 nm, respectively. Moreover, the diffraction peak intensity is the highest in the CuI inserted film. These facts suggest that the templating CuI layer leads PbPc molecules to form long-range ordering of high crystallinity.

To investigate the correlation between the crystallinity and the exciton diffusion length (L_D), the transfer matrix method was used to calculate L_D, extracted from the measured IPCE data shown in Figure 2.4.[44] In this calculation, we referred to the refractive index of the 60-nm-thick PbPc film from the literature for the 20-nm-thick PbPc film deposited on the 0.5-nm-thick CuI film because the overall absorption spectrum is similar.9 From the simulation, L_D increases from 6.2 nm to 8.8 nm when the CuI templating layer is inserted, implying that L_D increases with increasing crystalline order and size which is consistent with previous reports.[45, 46] Therefore, the increase of L_D leads to the enhancement of J_{SC}.

The enhanced FF can be explained by the increase of J_{SC} and the low series resistance (R_S).[47] When the CuI templating layer is inserted, R_S and R_P are not significantly changed (See Table 2.1). It means that the contact resistance between the ITO and the organic layer is still low although the additional layer is inserted between the ITO

and the PbPc layer. Therefore, the slope of the *J-V* curve is maintained whether the CuI templating layer is inserted, indicating that increasing J_{SC} leads the *J-V* curve to the parallel translation by the amount of photocurrent without any change of the slope in the *J-V* curve, resulting in the increase of FF.[48]

To investigate the effect of the thickness on the OPV performances, the PbPc

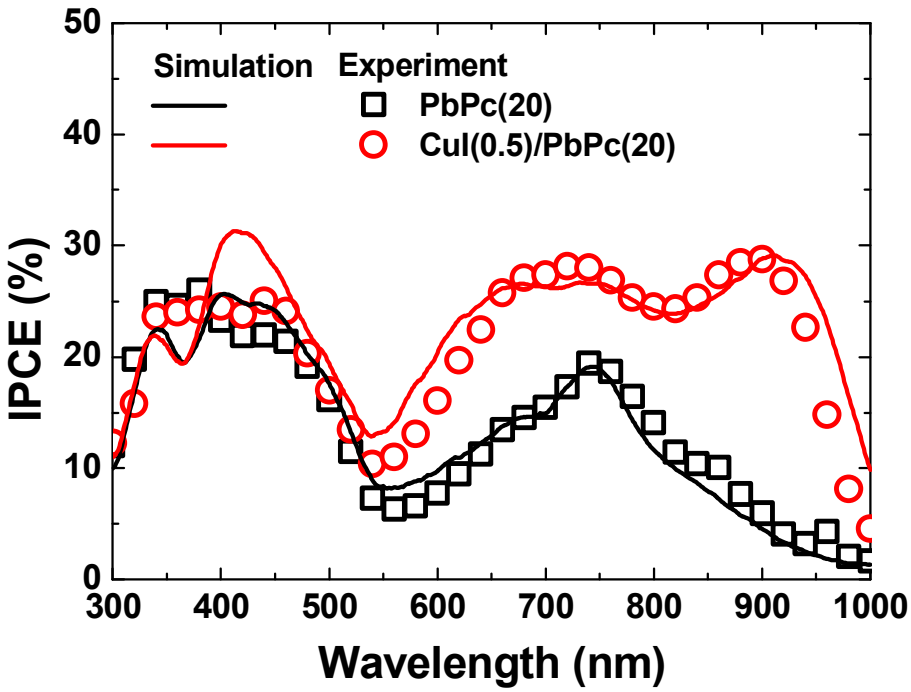

Figure 2.4 The simulation (solid lines) and experimental (symbols) IPCE spectra of the devices with and without the CuI layer

thickness is varied from 20 nm to 50 nm in increasing steps of 10 nm, as shown in Figure 5. Four cells were measured, and the average values with the respective standard deviations are indicated for each device. From Figure 2.5a, V_{OC} does not significantly change with increasing PbPc thickness because it is more related to the gap between the highest occupied molecular orbital (HOMO) level of the donor and the lowest unoccupied molecular orbital (LUMO) level of the acceptor. From Figure 2.5b, FF also does not change significantly; this is due to no change in the contact resistance. However, J_{SC} increases up to 8.9 mA cm^{-2} when the PbPc thickness is changed from 20 nm to 30 nm (see Table 2.1), and it decreases as the thickness of the PbPc layer increases further. Therefore, the PCE is maximized when the PbPc thickness is 30 nm.

Figure 2.6 displays the IPCE spectrum as a function of the PbPc thickness. In the measurement of the IPCE, the best performing solar cells were used among the four devices. There is no certain difference in the whole wavelength when the PbPc thickness is changed from 20 nm to 30 nm. Further increase of the PbPc thickness from 30 nm reduces the IPCE in the wavelength region corresponding to the PbPc absorption. This can be explained by the decreasing electric field within the exciton diffusion length from the PbPc/C_{60} interface, resulting in the reduced charge generation efficiency at the interface.[44]

2.4 Conclusion

In summary, we have demonstrated remarkable enhancement of the NIR absorption by using a CuI templating layer in PbPc-based organic solar cells. The IPCE result was 4.8 times higher, from 5.9% to 28.8% at the excitation wavelength of 900 nm,

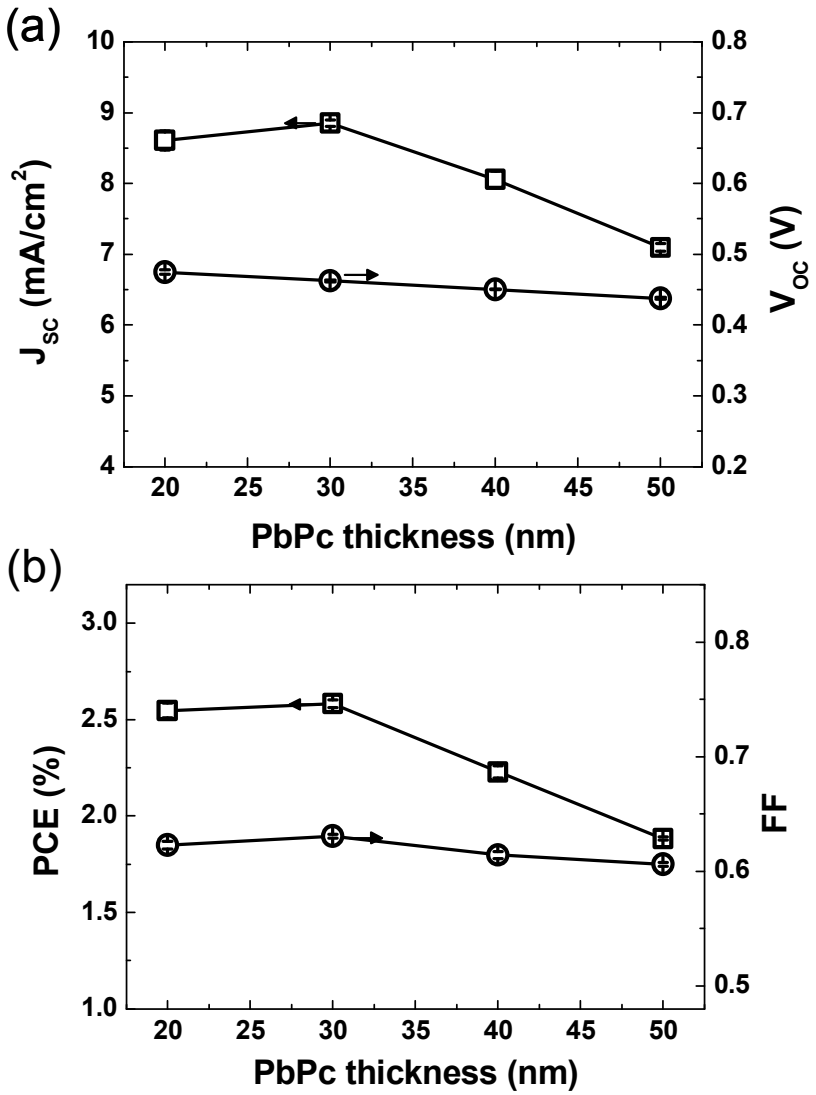

Figure 2.5 (a) Short circuit current (J_{SC}), and open circuit voltage (V_{OC}). (b) Power conversion efficiency (PCE), and fill factor (FF) of the devices as a function of the PbPc thickness

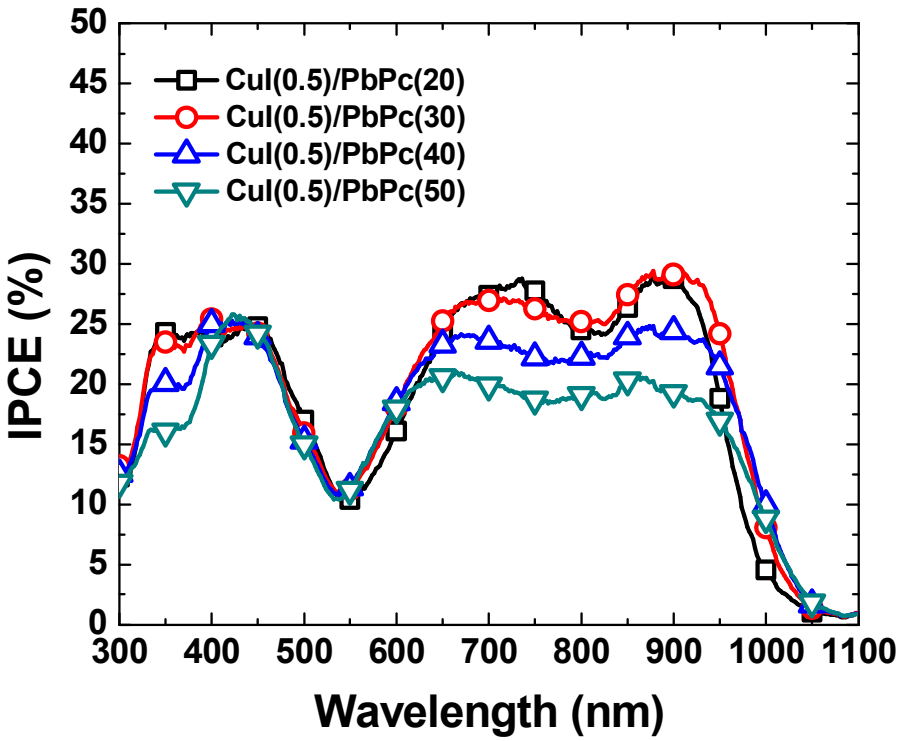

Figure 2.6 IPCE spectra as a function of the wavelength with different PbPc thicknesses, 20 nm (rectangular), 30 nm (circle), 40 nm (up triangle), and 50 nm (down triangle)

when using the CuI templating layer. This is due to the fact that CuI leads the PbPc molecules to forming a more crystalline structure with a preferred orientation. Furthermore the contact resistance between the ITO and the organic layer is still low although the additional CuI layer is inserted between the ITO and the PbPc layer, which resulted in an increase of J_{SC} from 4.6 mA cm^{-2} to 8.9 mA cm^{-2}, FF from 0.57 to 0.63, and PCE from 1.3% to 2.6% when the thickness of PbPc was 30 nm deposited on the 0.5-nm-thick CuI, when compared with the device in the absence of CuI. These results can be applied to tandem structures for the efficient use of the solar photon flux for light with a broad range of wavelengths.

Chapter 3. An efficient interconnection unit composed of electron-transporting layer/metal/p-doped hole-transporting layer for tandem organic photovoltaics

3.1 Introduction

Extending the absorption window in organic photovoltaics (OPVs) is a remaining task for the efficient use of the solar photon flux. Tandem organic photovoltaics (TOPVs) composed of sub-cells with a minimized absorption overlap and connected with interconnection units (ICUs) are a promising strategy to overcome the narrow absorption band of organic materials. Since the ICUs influence the cell performance electrically and optically, they have to be designed carefully for efficient TOPVs. The ICUs should be transparent in the absorption range of sub-cells to reduce optical losses and ensure the suitable energy level alignment between sub-cells to minimize voltage losses.[49, 50] In addition, it would be desirable if it works as an optical spacer to match current between the top and bottom cell.[24, 51]

Various structures have been reported as the ICUs up to now in vacuum deposited OPVs and can be categorized into two systems: *p*-*n* junctions using *p*- and *n*-doped layers and thin metal combined with organic or metal oxide layer.[14, 52-57] *p*-*n* junctions have an advantage of the energy level alignment between sub-cells.[14] However, they also have drawbacks of the diffusion of *n*-dopants into the pre-deposited layer and its instability for oxygen.[58] Moreover, the absorption loss occurs at the ICUs because the acceptor material is used as a host for the *n*-doping for the efficient electron transport from the acceptor to the recombination contact.[59] In contrast, the absorption loss can be minimized in case of using thin metal with

metal oxide because the absorption of the metal layer can be negligible due to the very thin layer (~0.5 nm) and the metal oxides such as rhenium oxide (ReO_3) and molybdenum oxide (MoO_3) are transparent in the active window of the TOPVs.[60, 61] Moreover, the carrier recombination can occur efficiently in the metal layer, resulting in the open circuit voltage (V_{OC}) loss of ~3% as compared to the sum of the V_{OC} of the top and bottom cells.[52, 53] Unfortunately, however, the metal/metal oxide based ICUs do not work properly as an optical spacer due to the decrease of conductivity with increasing the thickness of the metal oxide layer which results in the reduction of fill factor (FF).[57] The role of the ICU as an optical spacer is important in TOPVs to match current between the top and bottom cell,[24] microcavity OPVs to maximize optical interference,[62] and organic photodetectors to tune the active wavelength.[63]

In this study, we report a novel ICU structure consisting of an organic electron-transporting layer (ETL)/thin metal/*p*-doped hole-transporting layer (*p*-HTL) for efficient TOPVs. By using bathocuproine (BCP), Ag and ReO_3 doped 1,1-bis-(4-bis(4-methyl-phenyl)-amino-phenyl)-cyclohexane (TAPC) as the ETL, metal and *p*-HTL in the ICU, respectively, we demonstrate that the ICU satisfies all the requirements of optical transparency, little voltage loss, and functioning as an optical spacer at the same time based on the FF, V_{OC} and short circuit current density (J_{SC}) of the TOPVs as a function of the thickness of *p*-HTL and the comparison with theoretical calculations.

3.2 Experimental

The 150nm-thick ITO coated glass substrate was cleaned with acetone and

isopropyl alcohol, and exposed to UV-O_3 for 10 min before use. All the materials were thermally evaporated at the base pressure of $<10^{-7}$ Torr without breaking the vacuum. The 25 mol% *p*-doped layer in the ICU was formed using the co-evaporation of the TAPC and ReO_3. The evaporation rate of the organic layers was 1 Å s^{-1} except MoO_3 (0.1 Å s^{-1}), ReO_3 (0.125 Å s^{-1}) and Al (0.2 Å s^{-1} for the ICU and 4 Å s^{-1} for the cathode). The active area of devices was 4 mm^2 and more than four devices were fabricated to average the cell performance. After evaporation, the devices were encapsulated using an epoxy resin with glass cans in an N_2 environment. The UV-vis absorption spectra of the films were recorded with a VARIAN Cary 5000 UV-vis spectrophotometer. The current density-voltage (*J-V*) characteristics were measured under AM 1.5G solar simulator illumination (Newport, 91160A), and recorded in a Keithley 237 source measurement unit. The light intensity was calibrated using a standard Si-solar cell (NREL).

3.3 Results and Discussion

Figure 3.1 shows the device structures of the single and TOPVs. The single cells are composed of 150 nm thick ITO, 1 nm copper iodide (CuI), 20 nm lead phthalocyanine (PbPc), 40 nm C_{60}, 8 nm BCP and Al for the PbPc-based OPV, and 150 nm thick ITO, 3 nm MoO_3, 8 nm boron subphthalocyanine chloride (SubPc), 35 nm C_{60}, 8 nm BCP and Al for the SubPc-based OPV, respectively, which were experimentally optimized. In the PbPc-based OPV, CuI was inserted between ITO and the PbPc layer to control the crystallinity of the PbPc layer.[64] The TOPV consisted of 10 nm thick SubPc, 15 nm thick PbPc as donors and 15 nm thick C_{60} and 10 nm thick C_{60} as the acceptors for the bottom and top cell, respectively. In

the ICU, 3 nm BCP, 0.3 nm Ag and 25 mol% TAPC:ReO_3 are used as the ETL, recombination layer and *p*-HTL, respectively. The thickness of the TAPC:ReO_3 layer

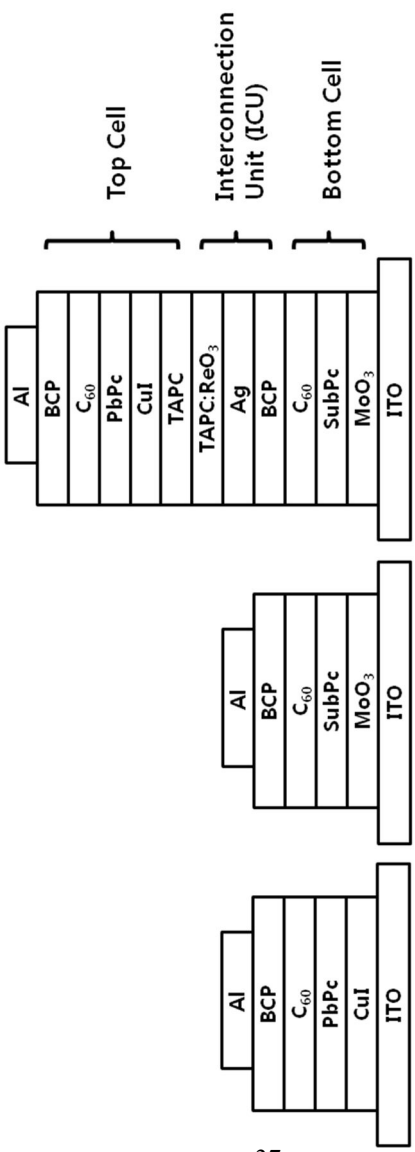

Figure 3.1 The device structures of (a) PbPc-based cell, (b) SubPc-based cell, and (c) tandem cells

was systematically varied from 0 nm to 130 nm to investigate the effect as the optical spacer. The ReO_3 doped TAPC layer has been applied as the efficient hole injection layer and charge generation units (CGUs) in organic light emitting diodes (OLEDs).[65, 66] It was also used as the efficient hole extraction layer in OPVs, inserted between ITO and the donor layer whose the highest occupied molecular orbital (HOMO) level is 5.6 eV.[67] Here, the TAPC:ReO_3 layer in the ICU works as the efficient charge recombination contact and the optical spacer. An additional neat TAPC layer was inserted between the TAPC:ReO_3 and CuI layer to prevent the exciton quenching at the interface.

Figure 3.2 displays the absorption coefficient of the donor and acceptor materials used in the top and bottom cells and the transmittance of the ICUs with different thicknesses of the *p*-HTL deposited on the glass. The absorption overlap of SubPc and PbPc is relatively small, indicating that the solar photon flux can be absorbed separately in the top and bottom cell with the minimized energy loss. The PbPc absorption is extended into the near-infrared (NIR) region as compared to the reported one,[20] due to the enhanced crystallinity with preferred orientation, which originates from the templating effect of CuI.[64, 68] The transmittance of the ICU is over 95% in the active range, fulfilling the requirement for the ICUs when the *p*-doped layer is 5 nm. A new absorption peak appears at the wavelength of 691 nm when the thickness of the *p*-HTL is 100 nm, originating from the charge transfer (CT) complexes formed between the TAPC and ReO_3 molecules.[69] The formation of the CT complex indicates that holes are generated by doping to increase the conductivity in the layer. Even though the layer is 100 nm thick , the transmittance of the ICU is over 85 % in the active wavelength range, which is higher than

MoO3 and ITO

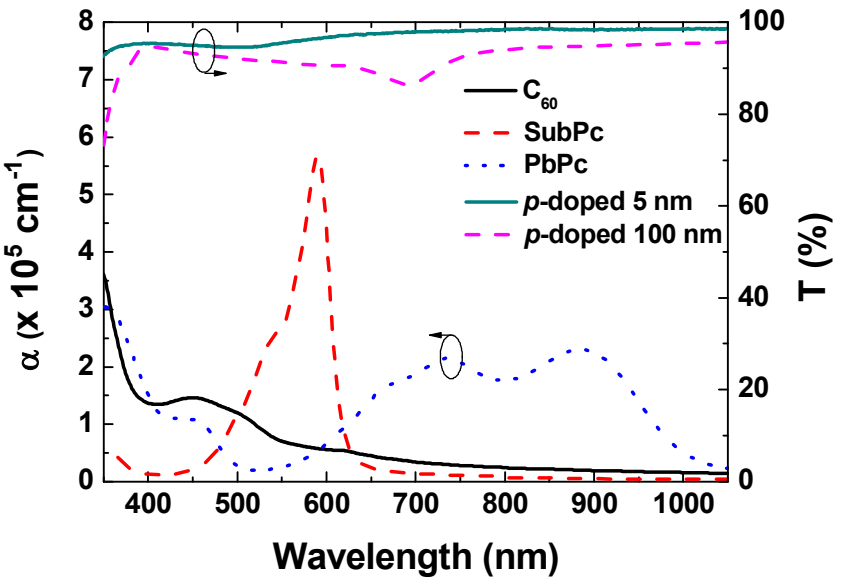

Figure 3.2 The absorption coefficient of materials used as donors and acceptors and the transmittance of ICUs with different *p*-doped layer thicknesses. All the layers are deposited on the glass

commonly used as the hole injection layer and anode in organic electronics, respectively.[61, 70] This indicates that the p-doped layer in the ICU can work as an optical spacer with minimized optical loss.

Figure 3.3a displays the current density-voltage (*J-V*) characteristics of the top and bottom cells as well as the tandem cell with the ICU, composed of BCP (3 nm)/Ag (0.3 nm)/TAPC:ReO_3 (25 mol%, 5 nm). The solar cell performance is summarized in **Table 3.1**. The single devices show the FF of 0.61, V_{OC} of 0.46 V, the power conversion efficiency (PCE) of 2.03% for the PbPc-based OPV, and the FF of 0.66, V_{OC} of 1.06 V, PCE of 2.87% for the SubPc-based OPV, respectively. The TOPV with the 5-nm-thick ICU shows the FF of 0.6 and V_{OC} of 1.47 V. The V_{OC} value of the TOPV is very close to the sum of the top and bottom cell with the V_{OC} loss of 3%, indicating that there is a negligible energetic barrier for holes and electrons to transport into the recombination contact. PCE of TOPV is 3.19%, which is comparable with the previous report using PbPc and SubPc as the top and bottom cell, respectively.[56]

In order to investigate the role of the ICU as the optical spacer, the thickness of the *p*-doped layer is systematically varied from 0 nm to 130 nm with the fixed doping concentration of 25 mol%, and the results are shown in Figure 3.3b. When the *p*-doped layer is 0 nm, an S-curve is generated with the reduced FF of 0.48 and V_{OC} of 1.37 V. This fact indicates that there is an energetic barrier between the top cell and the ICU, resulting in the resistance to transport holes from the donor layer of the top cell to the metal layer in the ICU.[67] This S-shape is removed by inserting the *p*-HTL, increasing the FF and V_{OC} at the same time. Interestingly, J_{SC} is significantly changed with increasing the thickness of the *p*-doped layer.

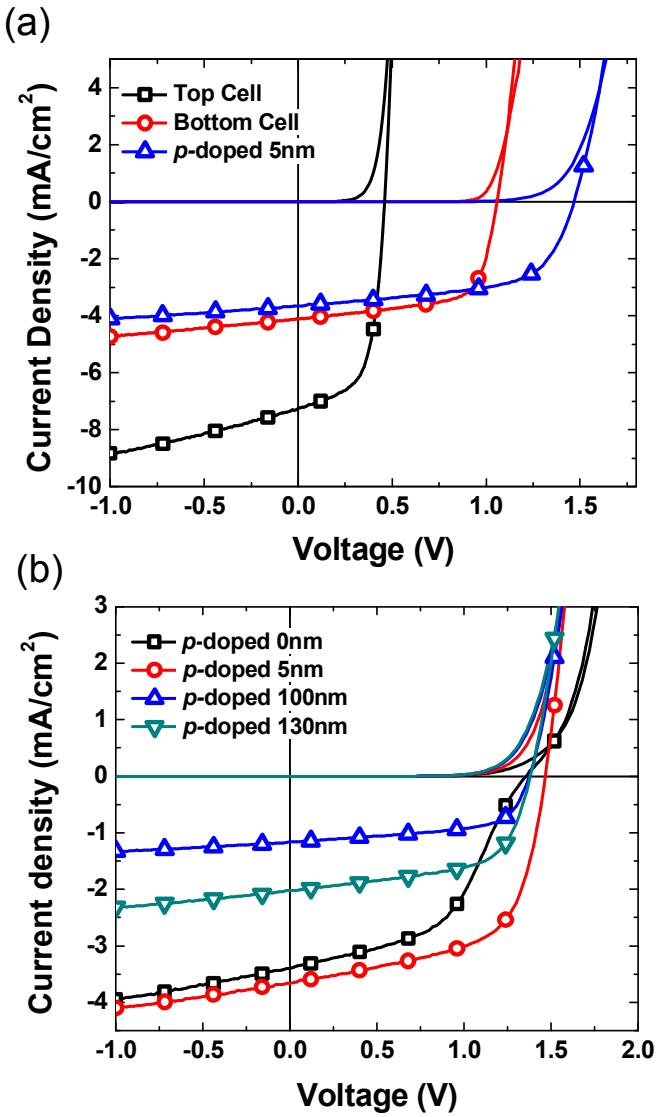

Figure 3.3 *J-V* characteristics of (a) the top cell, bottom cell and tandem cell with the 5-nm-thick *p*-doped layer in the ICU, and (b) the tandem cells with different *p*-doped layer thicknesses in the ICUs

Table 3.1 Solar cell performance with different *p*-doped layer thicknesses in the ICU. The ideality factor (n) and dark saturation current density (J_S) are obtained by fitting the dark *J-V* curve with the Shockley diode equation. The calculated V_{OC} is obtained by using eq. (3-1).

	PCE (%)	J_{SC} (mA/cm^2)	V_{OC} (V)	FF	n	J_S (nA/cm^2)	Calculated V_{OC} (V)
Top Cell	2.03 ± 0.01	7.25 ± 0.01	0.46 ± 0.01	0.61	1.54	47.3	0.47
Bottom Cell	2.87 ± 0.01	4.11 ± 0.01	1.06 ± 0.01	0.66	2.08	2.91 x 10^{-3}	1.12
p-doped 5 nm	3.19 ± 0.03	3.62 ± 0.05	1.47 ± 0.01	0.60	3.96	1.14	1.52
p-doped 100 nm	0.96 ± 0.01	1.16 ± 0.01	1.35 ± 0.01	0.61	4.00	1.82	1.37
p-doped 130 nm	1.68 ± 0.01	2.03 ± 0.01	1.37 ± 0.02	0.59	4.01	2.08	1.42

To understand this behavior, J_{SC} of the top and bottom cell is theoretically analyzed as a function of the thickness of the *p*-HTL using the transfer matrix method coupled with exciton diffusion equation.[44, 62, 71, 72] The theoretical results are compared with the experimental ones as shown in Figure 3.4a. The complex refractive indices of the materials were obtained from the literature for the simulation.[20, 44] The exciton diffusion lengths (L_D) of 9.94 nm, 8.8 nm, 14.4 nm were used for SubPc, PbPc and C_{60}, respectively, which were extracted from fitting the measured incident photon-to-electron conversion efficiency (IPCE) data.[44, 62] The simulation predicts that while the top cell shows small variation in J_{SC} with increasing the thickness of the *p*-HTL, J_{SC} of the bottom cell changes significantly with a sinusoidal pattern. The simulation results can be easily understood based on the interference effect of the incident light in the TOPVs shown in Figure 4(b), which displays the distributions of the optical intensity at the wavelengths of 580 nm and 740 nm, representing the selective absorption for SubPc and PbPc, respectively. The intensity of the light with 740 nm wavelength in the top cell does not change with increasing the thickness of the *p*-HTL from 5 nm to 100 nm because the active layer position of the top cell from the metal cathode is independent of the thickness of the *p*-HTL. In contrast, the intensity of the 580 nm light in the bottom cell is drastically reduced as the thickness of the *p*-HTL increases. Therefore only J_{SC} of the bottom cell is critically dependent on the thickness of the p-doped layer. This simulation results predict that J_{SC} will vary sinusoidally in the TOPV because J_{SC} in a TOPV is dictated by the smaller one of the sub-cells. The very good match between the experimental data and the simulation clearly demonstrates that the p-doped layer works as the optical spacer

very well with negligible optical loss and resultantly negligible loss in J_{SC}, In other words, the

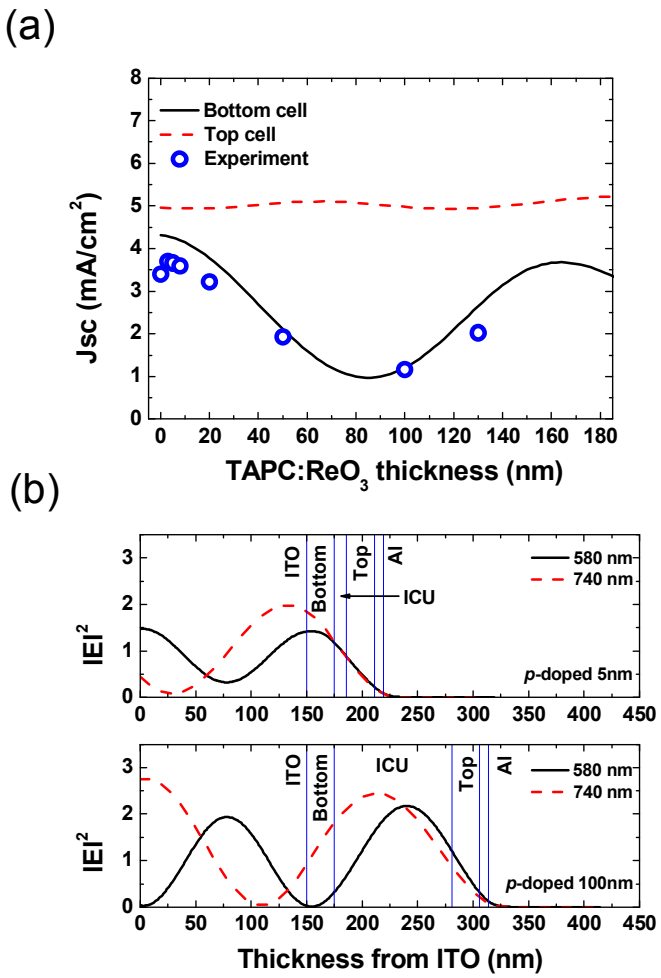

Figure 3.4 (a) The short circuit current density (J_{SC}) as a function of the TAPC:ReO_3 thickness obtained from the optical simulation and experiments. (b) Schematic device structures of tandem devices with different *p*-doped layer thicknesses of 5 and 100 nm. Optical intensity distributions at wavelengths of 580 nm and 740 nm are presented with an ITO thickness of 150nm

current matching between the top and bottom cell can be optimized by varying the thickness of the *p*-HTL in the ICU easily without disturbing the electrical characteristics.

Figure 3.5 displays the dependence of V_{OC} and FF on the thickness of the *p*-HTL. FF is enhanced when the *p*-doped layer is used in the ICU and it is not deteriorated as the thickness of the *p*-HTL increases, implying that there is little potential drop in the ICU for the electrons and holes to reach the recombination layer. V_{OC} is also increased when the *p*-doped layer is introduced in the ICU and it is slightly decreased with increasing the thickness of the *p*-HTL. V_{OC} can be expresses as follow:

$$V_{oc} = \frac{nkT}{q} \ln\left(\frac{J_{sc}}{J_s}\right) \tag{3-1}$$

where n is the ideality factor, k is the Boltzmann constant, q is the elementary charge and J_S is the dark saturation current. In this system, J_{SC} is changed due to the optical spacer effect, while n and J_S are not significantly changed as the thickness of the *p*-HTL increases. This indicates that the reduction of V_{OC} is related to the change of J_{SC}, which is consistent with the calculated V_{OC} as shown in table 3.1.

3.4 Conclusion

We have demonstrated a novel structure of the ICU composed of ETL/thin metal/*p*-HTL for efficient TOPVs. BCP, Ag and TAPC:ReO_3 were used as the ETL, metal and *p*-HTL, respectively. FF of the TOPVs employing the ICU does not change with increasing the thickness of the *p*-HTL and V_{OC} loss was minimal (~3%). The

variation of J_{SC} and V_{OC} with increasing the thickness of the *p*-HTL followed the theoretical prediction based on the exciton continuity equation without considering

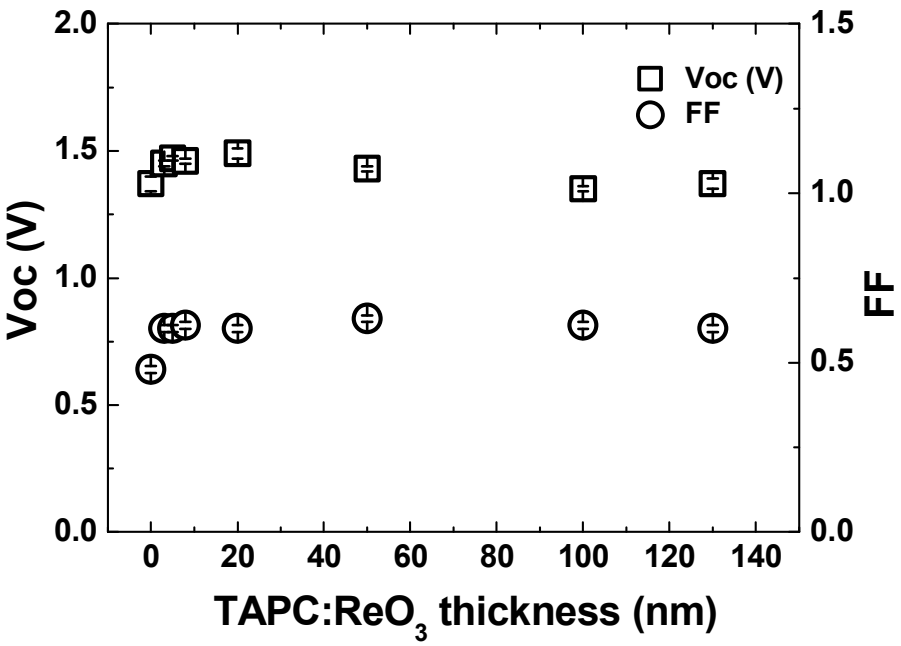

Figure 3.5 Open circuit voltage (V_{OC}) and fill factor (FF) as a function of the TAPC:ReO_3 thickness in the ICUs

the electrical loss, indicating that the ICU up to the thickness of 100 nm does not disturb the electrical characteristics of the TOPVs. All the facts clearly prove that the ICU satisfies the requirements of optical transparency and negligible extra electrical resistance for recombination up to 100 nm to be used as an optical spacer as well. This ICU structure has large potential to use in TOPVs, mocrocavity OPVs and wavelength-tunable organic photodetectors as the optical spacer to optimize the cell performance without the electrical losses.

Chapter 4. Correlation of the electronic structure of an interconnection unit with the device performance of tandem organic solar cells

4.1 Introduction

Organic photovoltaic (OPV) cells have been shown to have lower efficiency than inorganic solar cells.[73, 74] One of the reasons is the narrow absorption band of the organic materials used as active layers in OPVs. Tandem organic photovoltaic (TOPV) cells are a potential candidate to extend the absorption range of the solar spectrum in the devices.[14, 15, 54, 75-77] TOPVs are composed of more than two subcells whose absorption overlap is minimized for the efficient use of solar photon flux and the interconnection unit (ICU), which should be transparent in the absorption range of subcells to reduce optical losses and ensure suitable energy level alignments between the subcells to minimize voltage losses. In addition, it would be desirable if they worked as optical spacers to match the current between the top and bottom cells.[24, 51, 52, 77, 78]

Various structures have been reported for the vacuum deposited ICUs, which can be classified into two systems: thin metal combined with metal oxide, or the *p*-doped layer and *p*-*n* junctions using *p*- and *n*-doped layers.[53, 55-57, 59, 77, 78] Both techniques show efficient charge recombination in the ICUs with minimized open circuit voltage (V_{OC}) loss. In terms of the optical spacer, however, metal oxide in the ICU does not work properly due to the decrease in the conductivity with increasing thickness of the metal oxide layer, resulting in the reduction of the fill factor (FF).[57] In contrast, the doped layer can be used as an optical spacer because it does not affect the device's performance electrically.[14, 24, 51, 77, 78] In other words,

the generated carriers in the subcells can reach the recombination contact through the doped layers with few energetic barriers.

Electrical doping is widely used for efficient charge injection or extraction in organic electronics.[38, 58, 60, 66, 67, 79, 80] It is also in use for the charge generating units (CGUs) in tandem organic light emitting diodes.[66, 80] The mechanisms of charge generation by electrical doping in the CGUs are well established.[66, 80] For instance, the charge carrier generation layers in the CGUs consisting of *p*-doped hole-transporting layer (*p*-HTL)/1,4,5,8,9,11-hexaazatriphenylene hexacarbonitrile (HATCN)/*n*-doped electron-transporting layer (*n*-ETL) depends on the vacuum level shift at the HATCN/*n*-ETL and the free carrier density of the ETL rather than the lowest unoccupied molecular orbital (LUMO) level of the ETL.[66] In the TOPV cells, however, the operation mechanism of the doped layer in the ICUs has not been systematically investigated yet.

In this paper, we systematically investigated the effect of the electrical properties of the *p*-doped layer in the ICU composed of ETL/metal/*p*-HTL on the performance of a TOPV cell. V_{OC} is enhanced as the doping concentration increases due to the reduction of the difference between the Fermi level and the highest occupied molecular orbital (HOMO) level of the *p*-HTL. FF is also enhanced as the doping concentration increases due to the lowering of the energetic barrier between the metal and the *p*-HTL for the hole transport and the increase of the conductivity in the *p*-HTL. Moreover, the depletion width is reduced as the doping concentration increases due to the increased carrier density in the doped layer, facilitating the tunneling process at the interface.

4.2 Experimental

The 150 nm-thick ITO coated glass substrate was cleaned with acetone and isopropyl alcohol, and exposed to UV-O_3 for 10 min. before use. All the materials were thermally evaporated at a base pressure of $<10^{-7}$ Torr without breaking the vacuum. The *p*-doped layer in the ICU was formed using the co-evaporation of the 1,1-bis-(4-bis(4-methyl-phenyl)-amino-phenyl)-cyclohexane (TAPC) and rhenium oxide (ReO_3). The evaporation rate was varied from 0.01 Å s^{-1} to 0.25 Å s^{-1} for ReO_3 with a fixed rate of 1 Å s^{-1} for TAPC. The active area of each device was 4 mm^2 and more than four devices were fabricated to average the cell performance. After evaporation, the devices were encapsulated using an epoxy resin with glass cans in an N_2 environment. The UV-vis absorption spectra of the films were recorded with a VARIAN Cary 5000 UV-vis spectrophotometer. The current density-voltage (*J-V*) characteristics were measured under AM 1.5G solar simulator illumination (Newport, 91160A), and recorded using a Keithley 237 source measurement unit. The light intensity was calibrated using a standard Si-solar cell (NREL).

4.3 Results and Discussion

Figure 4.1a shows the device structure of the TOPV cell. The bottom cell is composed of 10 nm boron subphthalocyanine chloride (SubPc)/15 nm C_{60} and the top cell is composed of 3 nm 1,1-bis-(4-bis(4-methyl-phenyl)-amino-phenyl)-cyclohexane (TAPC)/15 nm lead phthalocyanine (PbPc)/10 nm C_{60}. A 3 nm thick molybdenum oxide (MoO_3) layer was inserted between the ITO and SubPc layer to secure good hole injection through the

junction. A 1 nm thick copper iodide (CuI) layer was deposited on the TAPC layer of the top

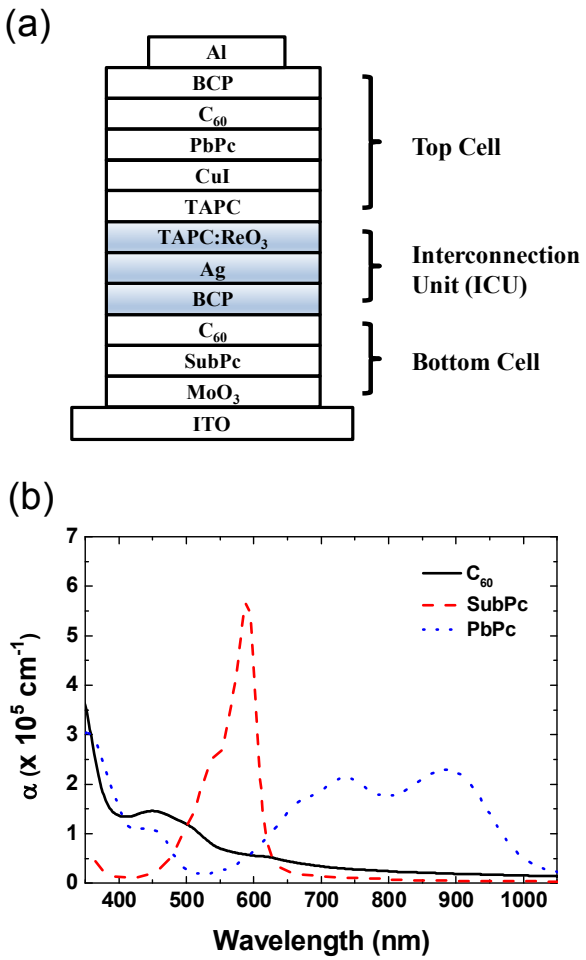

Figure 4.1 (a) The device structure of a tandem organic photovoltaic cell composed of a bottom cell, a top cell and an interconnection unit. (b) The absorption coefficient of organic materials used as donors and acceptors in the TOPV cell, which were deposited on glass

cell to increase the absorption of the PbPc layer in the near-infrared region.[64, 68] The subcells are connected by the ICU, consisting of 3 nm bathocuproine (BCP)/0.3 nm Ag/8 nm rhenium oxide (ReO_3) doped TAPC where the BCP, Ag and ReO_3 doped TAPC layers are used as the ETL, recombination layer and the *p*-HTL, respectively. The doping concentration of the *p*-HTL is systematically varied from 0 to 40 mol.% in order to investigate the effect of the doping concentration on the TOPV cell. The absorption overlap between the donors in the top and bottom cell is minimized, as shown in Figure 1b. The absorption of PbPc is extended into the near-infrared region because the copper iodide (CuI) inserted between TAPC and PbPc leads the PbPc molecules to form a more crystalline structure with a preferred orientation.[64, 68] The transmittance of the ICU is over 90%, fulfilling the requirement for optical transparency of the ICU.[77] In this study, the thicknesses of the layers in the TOPV cell are fixed and only the doping concentration of the *p*-HTL was systematically varied to exclude any optical effect on the performance of the TOPV cells.

Figure 4.2 displays the photo-current density-voltage (*J-V*) characteristics with different doping concentrations measured under AM 1.5G solar illumination. Interestingly enough, the solar cell performances are significantly affected by the doping concentration of the *p*-HTL in the ICU. In this system, the theoretically simulated short circuit current density (J_{SC}) is 4.19 mA cm^{-2}, which was determined by using the transfer matrix method coupled with the exciton diffusion equation.[77]

When an undoped layer is used in the ICU, an S-curve is generated with a J_{SC} value

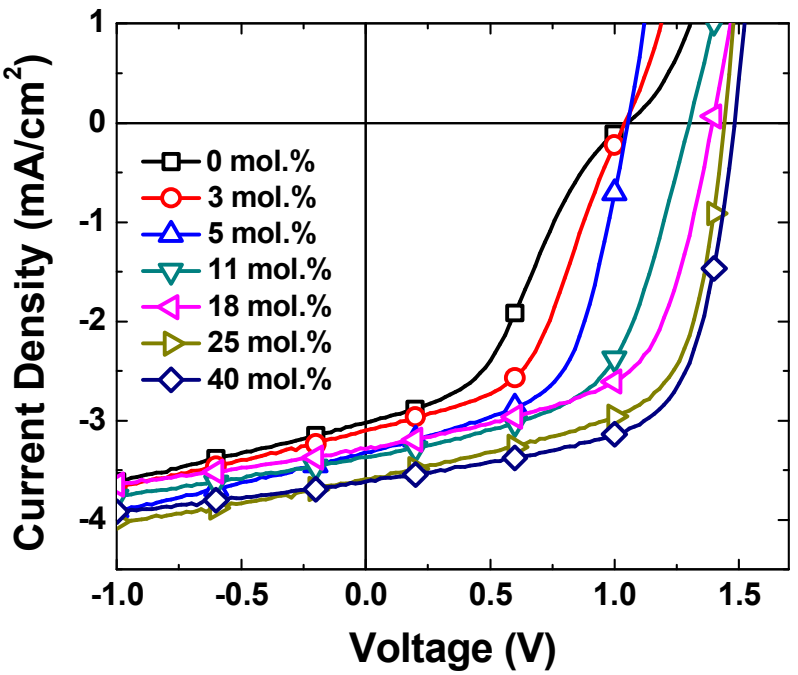

Figure 4.2 The *J-V* characteristics of tandem organic photovoltaic cells with varying doping concentrations of the *p*-HTL in the interconnection unit under AM 1.5G illumination

of 3 mA cm^{-2}, V_{OC} of 1.05 V, FF of 0.38 and a power conversion efficiency (PCE) of 1.19%, due to the resistance to the transportation of holes from the top cell to the recombination contact.[67, 77] The cell performance gradually improves as the doping concentation increases in the *p*-HTL up to a J_{SC} value of 3.57 mA cm^{-2}, V_{OC} of 1.49 V, FF of 0.64 and a PCE of 3.38%, when the 40 mol.% ReO_3 doped TAPC layer is used in the ICU. The doping concentration dependent performance of the TOPV cells are summarized in Table 4.1. The performances of the optimized single devices for the top and bottom cell are a J_{SC} value of 4.11 mA cm^{-2}, V_{OC} of 1.06 V, FF of 0.66 and PCE of 2.87% for the bottom cell, and a J_{SC} value of 7.25 mA cm^{-2}, V_{OC} of 0.46 V, FF of 0.61 and PCE of 2.03% for the top cell. The V_{OC} loss in the TOPV cell is less than 2% compared to the sum of the top and bottom cell, indicating that the energy levels between the top and bottom cell are well aligned, which is the one of the main requirements of the ICU.

To understand the dependence of the V_{OC} on the doping concentration of the *p*-HTL, ultraviolet photoelectron spectroscopy (UPS) measurements were performed using the He I (21.2 eV) as an excitation source under an ultra high vacuum of 10^{-10} torr. Figure 3a-d displays the energy level alignment at thermal equilibrium for different doping concentrations. The vacuum level and the HOMO levels of each layer were obtained from the UPS spectra (Fig. 4.3) and the LUMO levels were determined using the reported band-gap.[81] The vacuum level shift between BCP and Ag is in the range of 0.34 eV~0.4 eV, and the Fermi level (E_F)-HOMO level of BCP is around 2.78 eV for all the doping concentrations. There is no vacuum level shift at the Ag/TAPC when the neat TAPC layer is used, as shown in Figure 4.4a. As the doping level increases, the Fermi level in the *p*-HTL becomes closer to the HOMO

level of

Table 4.1 Summary of solar cell performances with different doping concentrations of the *p*-HTL in the interconnection unit. The series resistance (R_S) is obtained by fitting the dark J-V curve with the Shockley diode equation.

	PCE (%)	J_{SC} (mA/cm^2)	V_{OC} (V)	FF	R_S (Ωcm^2)
0 mol.%	1.19 ± 0.04	3.00 ± 0.03	1.05 ± 0.01	0.38 ± 0.01	30.34 ± 1.15
5 mol.%	1.95 ± 0.05	3.29 ± 0.04	1.06 ± 0.02	0.56 ± 0.02	9.81 ± 0.23
11 mol.%	2.41 ± 0.01	3.36 ± 0.01	1.28 ± 0.01	0.56 ± 0.02	8.32 ± 0.23
18 mol.%	2.62 ± 0.03	3.23 ± 0.03	1.39 ± 0.01	0.58 ± 0.01	6.76 ± 0.25
25 mol.%	3.15 ± 0.03	3.57 ± 0.03	1.46 ± 0.01	0.61 ± 0.01	4.47 ± 0.08
40 mol.%	3.38 ± 0.02	3.57 ± 0.03	1.49 ± 0.02	0.64 ± 0.01	4.96 ± 0.07

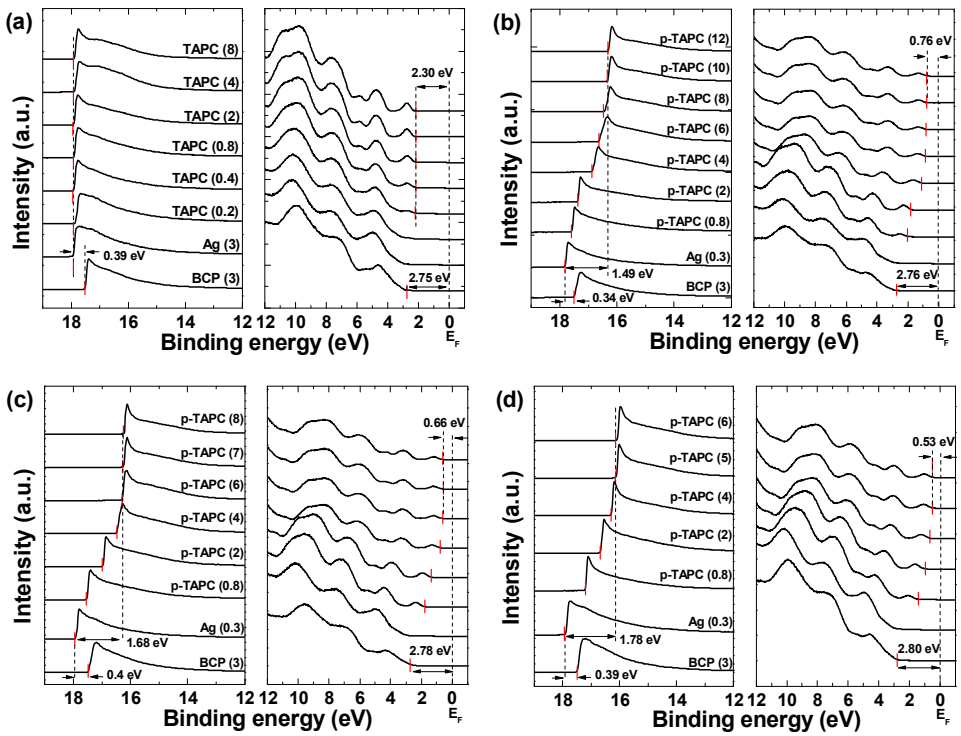

Figure 4.3 UPS measurements of BCP (3 nm)/Ag (0.3 nm)/*p*-TAPC with different doping concentrations of (a) 0 mol.%, (b) 11 mol.%, (c) 18 mol.% and (d) 25 mol.%. The vertical lines represent the changes in the vacuum level and the HOMO level. The thickness of each layer is indicated in the brackets with a nm scale

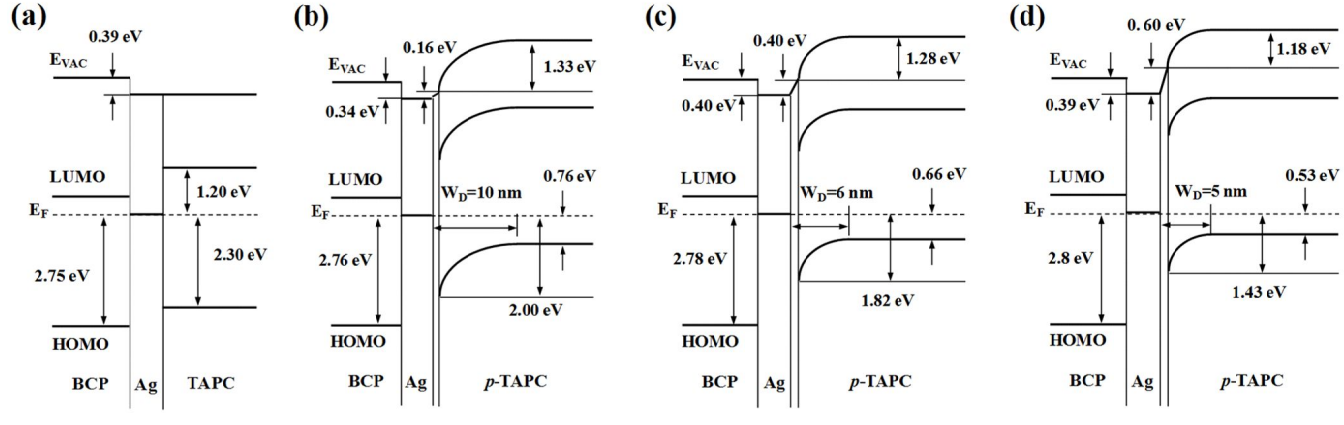

Figure 4.4 The schematic energy level alignment of BCP (3 nm)/Ag (0.3 nm)/*p*-TAPC with different doping concentrations of (a) 0 mol%, (b) 11 mol%, (c) 18 mol% and (d) 25 mol%

the TAPC, as expected. This shift in the Fermi level must be related to the V_{OC} of the TOPV cell as manifested in Figure 4.5 where the variation of V_{OC} and the E_F-HOMO level are plotted on the same scale against the doping concentration. Even though it is difficult to directly correlate the change in V_{OC} with the E_F-HOMO level of the *p*-TAPC layer because of the possibility of a vacuum level shift at the interface between the *p*-TAPC and the intrinsic TAPC layer, the increase in V_{OC} with the doping concentration can be interpreted based on the Fermi level shift of the *p*-HTL in the ICU. When the *p*-HTL is deposited on the Ag layer, a depletion layer is formed at the Ag/*p*-HTL and the depletion width becomes narrower as the doping concentration increases. It is interesting to note that there is a vaccum level shift at the Ag/*p*-HTL and its amount increases from 0.16 eV at the doping concentration of 11 mol.% to 0.6 eV at 25 mol.% doping, resulting in a reduced built-in potential at the *p*-HTL with increasing doping concentration, from 1.33 eV at a doping concentration of 11 mol.% to 1.18 eV at 25 mol.% doping, as shown in Figure 3b-d. Therefore, the EF-HOMO level of the *p*-HTL is reduced from 0.76 eV to 0.53 eV as the doping concentration increases from 11 mol.% to 25 mol.%., indicating that the energy level between the bottom cell and the top cell is more aligned with reduced the voltage loss in the ICU.

Another important parameter is the depletion width (W_D), which is expressed as follows

$$W_D = \sqrt{\frac{2\varepsilon_0 \varepsilon_r V_{bi}}{qp}} \tag{4-1}$$

where p is the free hole density in the *p*-HTL, V_{bi} is the built-in potential and ε_0 and

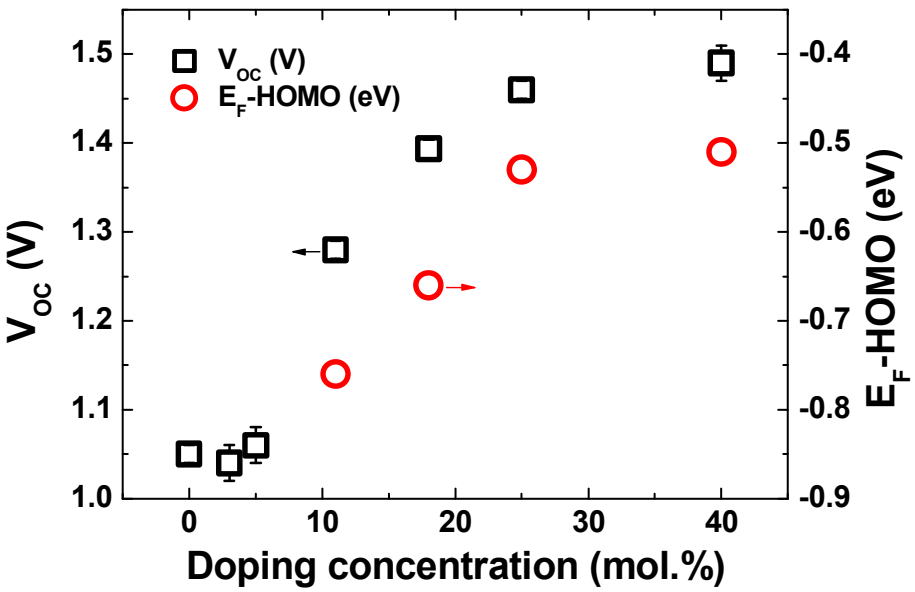

Figure 4.5 The V_{OC} dependence (left side) and the difference between the Fermi level (E_F) and the HOMO level of the *p*-HTL (right side) as a function of the doping concentration of the *p*-HTL

ε_r are the absolute and relative dielectric constants, respectively. W_D is inversely proportional to the free hole density in the *p*-HTL. Therefore, it becomes narrower as the doping concentration increases due to the increase of the free hole density in the *p*-HTL. W_D is 10 nm in the 11 mol.% ReO_3 doped TAPC layer, which is longer than its thickness of 8 nm in the TOPV cell. Therefore, the HOMO level is not fully shifted, resulting in an increase in the E_F-HOMO level of the *p*-HTL from 0.76 eV to 0.84 eV. This fact indicates that the the thickness of the doped layer in the ICU should be thicker than its depletion width to minimize the V_{OC} loss.

In order to investigate the relationship between the doping concentration of the *p*-HTL in the ICU and the FF of the TOPV cells, the series resistance (R_S) is obtained by fitting the dark *J-V* curve with the Shockley diode equation, as shown in Figure 4.7a. The FF value is enhanced up to 0.64 from 0.38 as the doping concentration increases from 0 to 40 mol.% in the *p*-HTL, which is inversely proportional to the R_S value. In this study, the doping concentration of the *p*-HTL is only changed with a fixed thickness of all the layers in the TOPV cell. Therefore, the change in the R_S value is directly related to the change in the conductivity in the *p*-HTL and the interface properties between the recombination contact and the top cell. The conductivity of the *p*-HTL is obtained by using $Mp^{++}p^{+}p^{++}M$ structures of ITO/TAPC: 50 mol.% ReO_3 (10 nm)/ TAPC: X mol.% ReO_3 (100 nm) [X = 0, 5, 11, 18, 25, 40]/ TAPC: 50 mol.% ReO_3 (10 nm)/Al (100 nm), as shown in Figure 4.7b (See Figure 4.6 for the original data).[82] The conductivity is enhanced from 1.43×10^{-8} S cm^{-1} to 5.19×10^{-7} S cm^{-1} as the doping concentration increases from 5 mol.% to 40 mol.%, respectively, which is at least two orders of magnitude greater than that of the intrinsic TAPC layer (~10^{-10} S cm^{-1}). This fact indicates that holes can be

transported

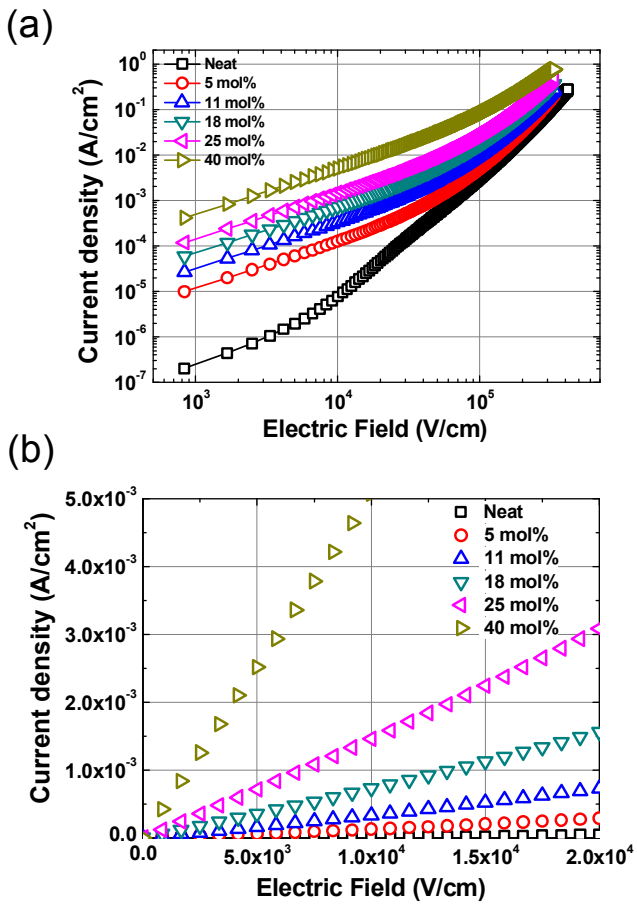

Figure 4.6 (a) The *J-F* characteristics of $Mp^{++}p^{+}p^{++}M$ devices with different doping doping concentrations of *p*-TAPC in the full scale and (b) linear *J-F* characteristics with different doping concentrations in the Ohmic region. The open symbols represent measured values and the solid lines indicate linear fits

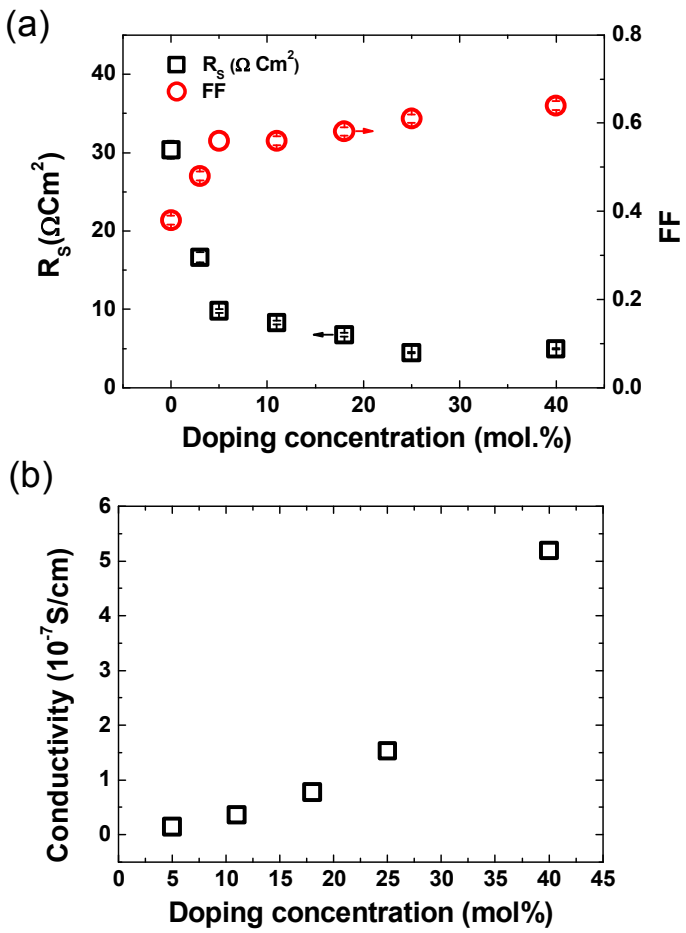

Figure 4.7 (a) The dependence of the series resistance (left side) and fill factor (right side) as a function of the doping concentration of the *p*-HTL. (b) The conductivity of the *p*-HTL as a function of the doping concentration, obtained from the current density–electric field (*J*-*F*) characteristics

efficiently to the recombination contact through the bulk of the *p*-HTL with an increasing doping concentration of *p*-HTL.

The interface property between Ag and the *p*-HTL is also an important factor affecting the FF in the TOPV cells. When neat TAPC is used in the ICU, the energetic barrier for holes to overcome for transport at the Ag/TAPC interface is 2.3 eV. This indicates that holes cannot be injected from Ag to the TAPC layer and be accumulated at Ag/TAPC, resulting in an S-curve with a reduced FF.[67, 83] When the *p*-HTL is used in the ICU, the energetic barrier, shown in Figure 3a-d, which is estimated for a *p*-HTL thickness of 0.8 nm in the UPS data, is reduced from 2 eV to 1.43 eV as the doping concentration increases from 5 mol.% to 25 mol.%, as shown in Figure 4.4. However, this barrier is too large for holes to overcome for transport at the interface. In this system, W_D is reduced from 10 nm at the doping concentration of 5 mol.% to 5 nm at 25 mol.% doping as shown in Figure 4.4. This fact represents that the possibility of the tunneling process is enhanced as the doping concentration increases. Therefore, holes can be transported more efficiently at the Ag/*p*-HTL interface through the tunneling process rather than the thermionic process as the doping concentration of the *p*-HTL increases, resulting in an enhanced FF.

4.4 Conclusion

In conclusion, we have demonstrated a correlation between the electrical properties of the *p*-HTL in the ICU and the device performance of TOPV cells by systematically varying the doping concentration of the *p*-HTL. The V_{OC} value in the TOPV cells increases with increases in the doping concentration due to the

reduction of the difference between the Fermi level and the HOMO level of the *p*-HTL. The FF is also enhanced with increases in the doping concentration, due to the enhancement of the conductivity in the *p*-HTL and efficient hole transport at the interface between Ag and the *p*-HTL through the tunneling process rather than the thermionic process.

Chapter 5. Effect of different p-dopants in an interconnection unit on the performance of tandem organic solar cells

5.1 Introduction

Tandem organic photovoltaics (TOPV) cells are a potential candidate to increase the solar cell performance by efficient use of solar photon flux with enhanced open circuit voltage (V_{OC}) in the series connection or short circuit current density (J_{SC}) in the parallel connection of individual sub-cells.[14, 15, 49, 84] TOPVs are composed of sub-cells with minimized absorption overlap and interconnection units (ICUs) which should be transparent in the absorption window of the sub-cells to reduce optical losses and ensure suitable energy level alignment between sub-cells to minimize voltage losses.[24, 50, 52, 53, 56, 57, 59, 77, 78, 85] It can be also functioned as an optical spacer to match the current between subcells.[24, 77, 85] Unfortunately, however, most research progresses in ICUs have only focused on the V_{OC} loss and current matching. The correlation between the ICU and fill factor (FF) of TOPV cells needs to be understood.

Recently, we reported efficient ICUs composed of electron-transporting layer (ETL)/metal/*p*-doped hole-transporting layer (*p*-HTL) which fulfill all the requirements for the efficient ICUs.[77] We also showed that the doping concentration in the *p*-doped layer in the ICU affects not only V_{OC} due to the change of the difference between the Fermi level and the highest occupied molecular orbital (HOMO) level (E_F-E_{HOMO}) of the *p*-doped layer, but also FF due to the enhancement of the conductivity in the *p*-doped layer and the efficient hole transport at the interface between metal and the *p*-doped layer through the

tunneling process rather than the thermionic process.[85] Also, the thickness of the *p*-HTL in the ICU can be tuned to match current between sub-cells without any optical and electrical losses.[77] However, the effect of different *p*-dopants in the ICU on the device performance has not been investigated yet, which will strongly affect the electrical properties in the *p*-doped layer because the different dopants have different charge generation efficiencies.[67, 69]

Even though various mechanisms of the electrical doping in organic semiconductors has been proposed,[38, 67, 69, 82, 86-88] charge generation efficiency, defined as the ratio of the carrier density to the number of dopant molecules in the doped film, is directly related to the energy difference between the HOMO level of a host and the Fermi level of the *p*-dopants.[38, 67, 69, 82] Therefore, it is worthwhile to investigate the effect of the *p*-dopants in the ICU on the device performance.

In this study, we report the effect of different *p*-dopants used in the ICU composed of electron-transporting layer (ETL)/metal/*p*-doped hole-transporting layer (*p*-HTL) on the performance of the TOPVs. ReO_3, MoO_3, and CuI were selected as the *p*-dopants for the purpose, whose charge generation efficiencies are in the sequence of ReO_3>MoO_3>CuI.[69] V_{OC} in the TOPV is enhanced with increasing the charge generation efficiency of the *p*-HTL under a same doping concentration due to the reduction of the difference between the Fermi level and the HOMO level of the *p*-HTL. FF is also enhanced with increasing the charge generation efficiency of the *p*-HTL due to the efficient hole transport at the interface between Ag and *p*-HTL.

5.2 Experimental

The 0.7 mm-thick glass substrate coated with the 150 nm-thick ITO was cleaned

with acetone and isopropyl alcohol, and exposed to UV-O_3 for 10 min before use. All the materials were used as received from the manufacturer and thermally evaporated at the base pressure of $<8\times10^{-7}$ Torr without breaking the vacuum. The *p*-doped layer in the ICU was formed using the co-evaporation of the 1,1-bis-(4-bis(4-methyl-phenyl)-amino-phenyl)-cyclohexane (TAPC) and one of the *p*-dopants of ReO_3, MoO_3, and CuI. The evaporation rate of the organic materials was 1 Å s^{-1} except ReO3 (0.125 Å s^{-1}), MoO3 (0.077 Å s^{-1}) and CuI (0.102 Å s^{-1}). The active area of each device was 4 mm^2 and more than four devices were fabricated to average the cell performance. After the evaporation, the devices were encapsulated with glass cans using an epoxy resin (Nagase ChemteX Corporation, XNR5570) in an N_2 environment. The UV-vis absorption spectra of the films were recorded with a VARIAN Cary 5000 UV-vis spectrophotometer. The current density-voltage (*J-V*) characteristics were measured under AM 1.5G solar simulator illumination (Newport, 91160A) using a Keithley 237 source measurement unit. The light intensity was calibrated using a Si-reference cell (NREL) with 100 mW cm^{-2} and kept constant for the measurement. The ultraviolet photoemission spectra (UPS) were measured via He I (21.2 eV) photons as an excitation source (SPECS, 10/35) under a base pressure of $<10^{-10}$ Torr. The kinetic energies of photoelectrons emitted from the sample were recorded by a hemispherical analyzer (Perkin-Elmer, model PHI 5400) with an overall resolution of 0.05 eV. The E_F of ITO was pinned to E_F of the system which was determined by a clean Au surface because of the clear Fermi edge of Au.

5.3 Results and Discussion

Figure 5.1 shows the device structure, consisting of 10 nm boron subphthalocyanine

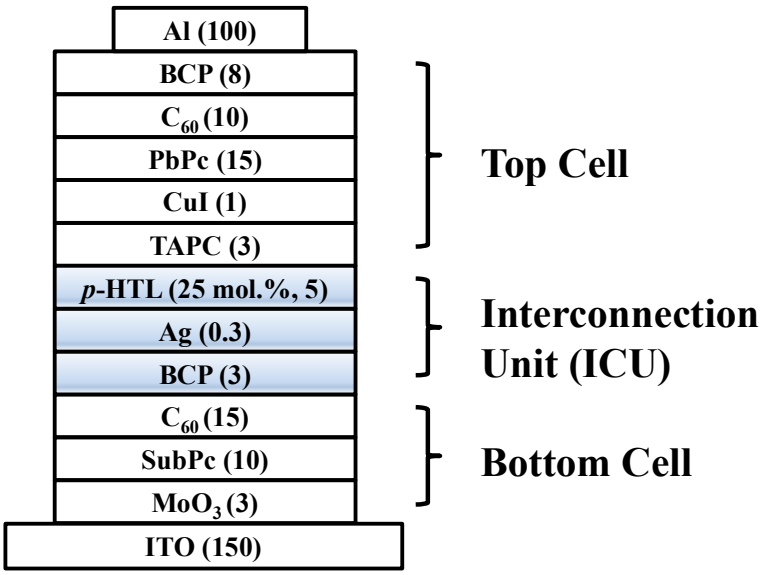

Figure 5.1 The device structure of tandem organic photovoltaic cells, composed of the top cell, bottom cell and interconnection unit with different p-dopants of the p-HTL. The thicknesses are indicated in the brackets with nm scale

chloride (SubPc)/15 nm C_{60} for the bottom cell and 3 nm TAPC/15 nm lead phthalocyanine (PbPc)/10 nm C_{60} for the top cell. A 1 nm thick copper iodide (CuI) was used in the top cell to extend the absorption of the PbPc layer into the near-infrared region.[64] The sub-cells are connected by the ICU, composed of 3 nm bathocuproine (BCP)/0.3 nm Ag/5 nm *p*-doped TAPC with the doping concentration of 25 mol.% where BCP, Ag and *p*-doped TAPC layers are used as the ETL, recombination layer and the *p*-HTL, respectively. Another role of Ag is to induce gap states in the BCP layer for electrons to be transported.[72] The structure of the solar cells is the optimized one as reported before.[77, 85] The optimized single devices for the top and bottom cells showed J_{SC} of 4.11 mA cm^{-2}, V_{OC} of 1.06 V, FF of 0.66 and power conversion efficiency (PCE) of 2.87% for the bottom cell and J_{SC} of 7.25 mA cm^{-2}, V_{OC} of 0.46 V, FF of 0.61 and PCE of 2.03% for the top cell, respectively.[77] The maximum J_{SC} in this system can be obtained when the thickness of the *p*-HTL is zero.[77] Unfortunately, however, the doped layer has to be used in the ICU to minimize the voltage loss and to reduce the resistance in the device.[85] Therefore, the experimentally obtained J_{SC} might be lower than the maximum J_{SC}.

Figure 5.2 displays the current density-voltage (*J-V*) characteristics with different *p*-dopants in the ICU, measured under an AM1.5G solar illumination by solar simulator with 100 mW cm^{-2}. The performance of the solar cells is summarized in Table 5.1. It is interesting to note that the solar cell performance is significantly affected by using the different *p*-dopants of the *p*-HTL in the ICU. When intrinsic TAPC layer is used in the ICU, S-curve is generated with reduced FF due to the resistance for holes to be transported from the top cell to the recombination contact.[67, 77, 85] V_{OC} is also reduced because the energy levels between the sub-cells

are not well

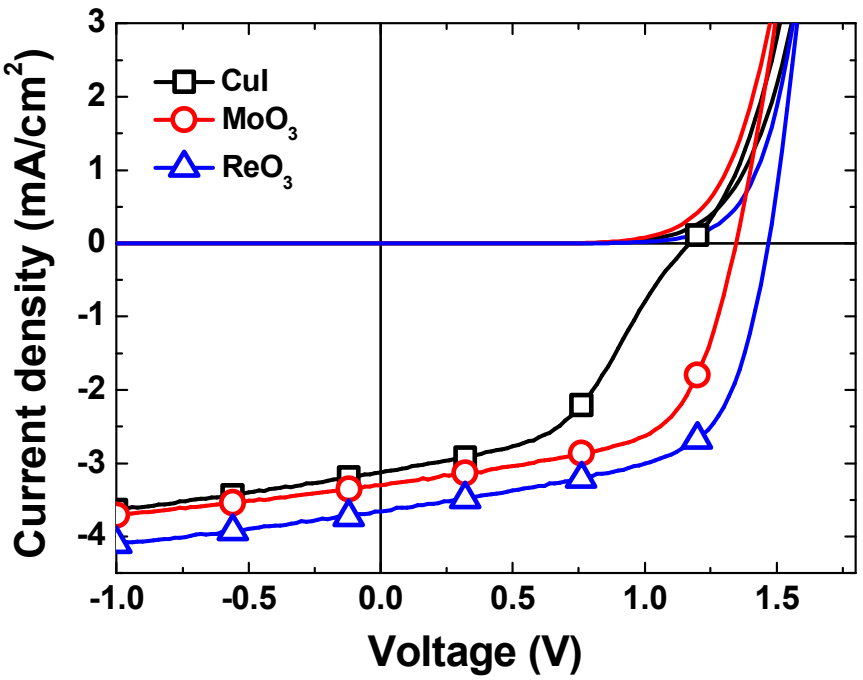

Figure 5.2 The current density-voltage (*J-V*) characteristics of tandem organic photovoltaic cells with different p-dopants in the ICU

Table 5.1 Solar cell performance with different p-dopants in the ICU. The series resistance (R_S) is obtained by fitting the dark *J-V* curve with the Shockley diode equation. The difference between the Fermi level and the HOMO level (E_F-E_{HOMO}) of the *p*-HTL and the depletion width (W_D) are obtained from the UPS data.

	PCE (%)	J_{SC} (mA/cm^2)	V_{OC} (V)	FF	R_S (Ωcm^2)	E_F-E_{HOMO} (eV)	W_D (nm)
None	1.19 ± 0.04	3.00 ± 0.03	1.05 ± 0.01	0.38 ± 0.01	30.34 ± 1.15	2.30	0
CuI	1.69 ± 0.01	3.13 ± 0.01	1.16 ± 0.01	0.38 ± 0.01	11.43 ± 0.35	1.31	~8
MoO_3	2.65 ± 0.02	3.31 ± 0.02	1.35 ± 0.02	0.56 ± 0.02	6.55 ± 0.21	0.68	~6
ReO_3	3.19 ± 0.03	3.62 ± 0.05	1.47 ± 0.01	0.60 ± 0.01	6.01 ± 0.24	0.57	~5

aligned, resulting in the voltage loss at the ICU.[85] By contrast, V_{OC} is significantly increased if the *p*-doped TAPC layer is used. The V_{OC} reaches 1.47 V when ReO_3 is used as the *p*-dopant and it is enhanced in the sequence of ReO_3 (1.47 V)>MoO_3 (1.35 V)>CuI (1.16 V) as summarized in Table 5.1. This result is in consistent with the sequence of the charge generation efficiency (ReO_3>MoO_3>CuI), whose free hole densities are 2.07×10^{18} cm^{-3}, 1.68×10^{18} cm^{-3}, 7.65×10^{17} cm^{-3} for ReO_3, MoO_3 and CuI, respectively, measured separately by the Schottky-Mott analysis of the *C-V* characteristics using metal/insulator/semiconductor structure (See Figure 5.3).[38] This is related to the work function of the *p*-dopants, ReO_3 (6.8 eV), MoO_3 (6.6 eV) and CuI (5.8 eV).[38, 67] FF is also enhanced up to 0.6 when the ReO_3 doped TAPC layer is used in the ICU and increases in the sequence of ReO_3 (0.6)>MoO_3 (0.56)>CuI (0.38), respectively.

The dependence of V_{OC} on the different *p*-dopants of the *p*-HTL can be understood from the ultraviolet photoelectron spectroscopy (UPS) measurements in Figure 5.4, which shows the evolution of the UPS spectra near the onset (left side) and the valence band region (right side) as a function of the thickness for different *p*-dopants. All binding energies are referenced to the Fermi level (E_F) of ITO. The vacuum level (E_{VAC}) shift, depletion width (W_D) of the *p*-HTL and the positions of the HOMO levels are analyzed with increasing the layer thickness and indicated using the vertical lines in the figures. The vacuum level and the HOMO level positions are determined by interpolating the shoulder of the each signal and background of the spectra.[65, 89] When intrinsic TAPC is used in the ICU, there was no vacuum level shift at the Ag/TAPC due to low free carrier density in the intrinsic TAPC layer.[85] In the case of using the *p*-doped layer with the different *p*-

dopants, however, the onset

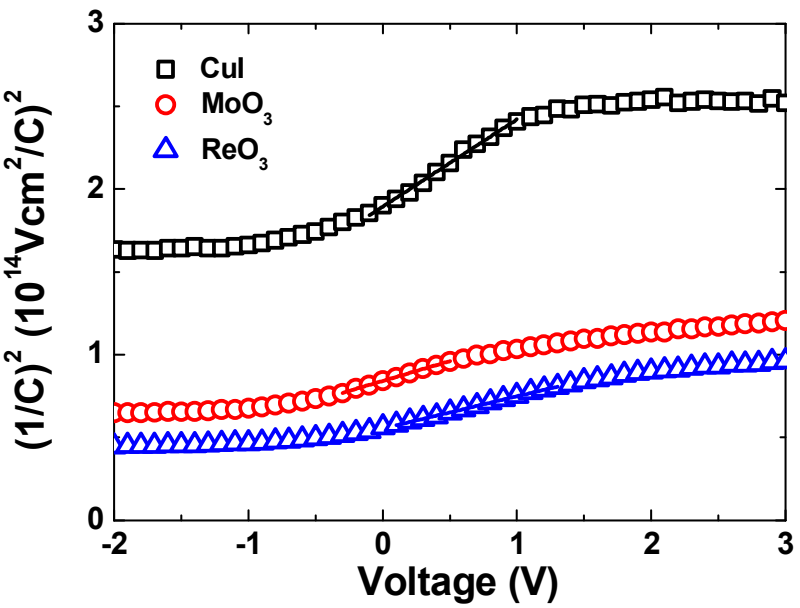

Figure 5.3 Linear C^{-2}-V characteristics of MIS devices at 300 K. The solid lines indicate the Schottky-Mott analysis

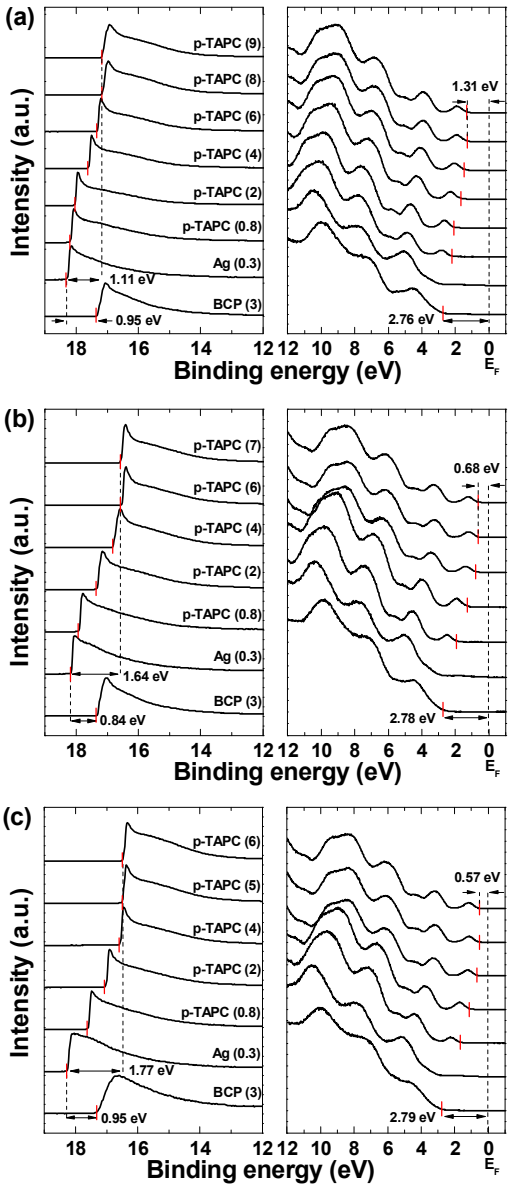

Figure 5.4 UPS data of BCP (3 nm)/Ag (0.3 nm)/*p*-TAPC with different *p*-dopants, (a) CuI, (b) MoO_3 and (c) ReO_3. The vertical lines represent the change of the vacuum level, HOMO level. The thicknesses of each layer are indicated with nm scale in the brackets

position moves toward lower binding energy and its amount is increased in the sequence of ReO_3 (1.77 eV)>MoO_3 (1.65 eV)>CuI (1.11 eV) due to the increase of the free carrier density in the *p*-HTL, which is directly related to the charge generation efficiency of the *p*-HTL. The HOMO position also moves toward lower binding energy and the saturation thickness of the *p*-HTL becomes narrower in the order of CuI>MoO_3>ReO_3.

Figure 5.5 displays the energy level alignment at the thermal equilibrium for different *p*-dopants used in the ICU. The E_{VAC} and the HOMO levels of each layer were obtained from the UPS spectra and the lowest unoccupied molecular orbital (LUMO) levels were determined by using the reported band-gap.[81] There was no vacuum level shift at the Ag/TAPC when the intrinsic TAPC layer was used in the ICU.[85] In the use of the *p*-HTL, however, there was vacuum level shift at the Ag/*p*-HTL interface due to the charge transfer from the *p*-HTL to Ag and its amount increased in the sequence of CuI (0.11 eV)<MoO_3 (0.32 eV)<ReO_3 (0.47 eV). This different vacuum level shifts originate from the different free carrier densities in the *p*-HTLs, which depend on the charge generation efficiency. Therefore, the E_F-E_{HOMO} of the *p*-HTL is changed with different *p*-dopants used in the ICU. When CuI is used in the ICU, the E_F-E_{HOMO} is 1.31 eV, resulting in reduced V_{OC} of 1.16 V with S-curve due to the energetic barrier at the Ag/*p*-HTL. The use of MoO_3 as the *p*-dopant in the ICU results in closer E_{HOMO} to the Fermi level up to 0.68 eV, leading to the reduced voltage loss of 11.2% compared to the sum between sub-cells. When ReO_3 is used in the ICU, the E_F-E_{HOMO} of the *p*-HTL is reduced to 0.57 eV due to the even higher free carrier density in the *p*-HTL. Therefore, V_{OC} is enhanced to 1.47 V, corresponding to only 3% voltage loss. Another *p*-

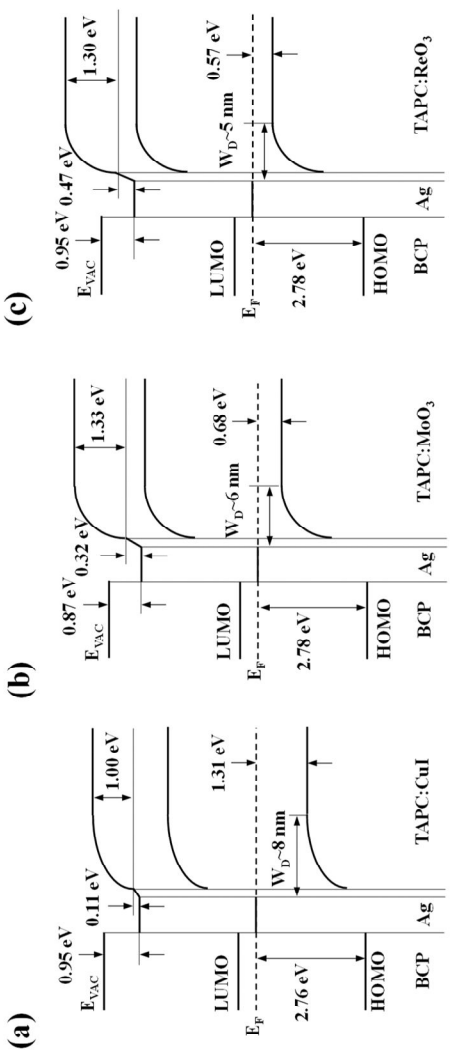

Figure 5.5 The schematic energy level alignment of BCP (3 nm)/Ag (0.3 nm)/*p*-TAPC with different p-dopants, (a) CuI, (b) MoO_3 and (c) ReO_3

affect the performance because the Fermi level of the intrinsic TAPC layer is higher than that of the *p*-doped TAPC layer. The vacuum level must be shifted downward at the interface of *p*-TAPC/TAPC and the HOMO level will also be bended downward in the intrinsic TAPC layer due to the charge transfer. This indicates that holes generated in the top cell can be extracted from the top cell to *p*-HTL in the ICU without any energetic barrier.

An injection barrier at the interface between electrodes and organic layers affects FF due to the charge accumulation at the interface inducing the change of internal electric field under forward bias.[83, 90, 91] In the ICU, electrons and holes are injected from Ag to BCP and *p*-HTL, respectively under forward bias. At the interface of BCP/Ag, electrons can be injected through the thermionic process because the injection barrier is relatively low. At the interface of Ag/*p*-HTL, in contrast, holes are expected to be injected through the tunneling process due to the high injection barrier. Since the tunneling probability is proportional to the barrier height and tunneling width at the Fermi level, the CuI doped HTL requires the highest voltage for tunneling of holes with the lowest tunneling probability among the three *p*-HTLs, resulting in the S-curve with the lowest FF.[83] The tunneling probability will be increased by using ReO_3 followed by MoO_3 as the dopants in the *p*-HTL due to the reduced energy barrier, resulting in high FF's, which are consistent with the experimental results.

5.4 Conclusion

We have systematically investigated the effect of the *p*-dopants in the ICU composed of electron-transporting layer (ETL)/metal/*p*-doped hole-transporting

layer (*p*-HTL) on the performance of TOPVs. ReO_3, MoO_3, and CuI were selected as the *p*-dopants for the purpose, whose charge generation efficiencies are in the sequence of ReO_3>MoO_3>CuI. Dopants with higher charge generation efficiency resulted in higher open circuit voltage (V_{OC}) due to the reduction of the difference between the Fermi level and the HOMO level of the *p*-HTL, and higher fill factor (FF) due to the efficient hole transport at the interface between Ag and *p*-HTL through the tunneling process rather than the thermionic process. These results show that the charge generation efficiency is an important parameter to select the *p*-dopant for the ICU and ReO_3 is a very effective *p*-dopant for the purpose. The use of ReO_3 in the ICU resulted in negligible loss of V_{OC} and FF in the tandem OPVs.

Chapter 6. Efficient vacuum-deposited tandem organic solar cells with fill factors higher than single-junction sub-cells

6.1 Introduction

Organic photovoltaic cells (OPVs) have shown large progress in the past several years. The power conversion efficiency (PCE) has reached up to ~9.6% for single junction solar cells with the donor-acceptor blended structure.[2, 3, 92-94] However, the efficiency of OPVs is still lower than those of inorganic solar cells mainly due to the narrow absorption windows of organic materials which can only partially response to the solar spectrum, resulting in large optical losses.[16, 64, 95] To overcome this limitation, ternary blend and tandem structures have been used. The ternary blend OPVs have two donors or acceptors possessing different absorption ranges in the active layers.[18, 96] In contrast, the tandem structures are formed using two or more active layers with different donor-acceptor pairs possessing complementary absorption spectra. Both concepts broaden the absorption range of the solar spectrum, thus to improve the light-harvesting ability of the device.[14, 15, 49] In tandem structures, however, open circuit voltage (V_{OC}) can be enhanced additionally if the sub-cells are connected in series. Based on this idea, the PCEs of tandem organic photovoltaic cells (TOPVs) have been enhanced up to ~10.7% for the solution-processed devices using polymers and ~10% for the vacuum-deposited devices using small molecules as active materials.[76, 97-99]

The vacuum deposition have several advantages over solution processes for the fabrication of TOPVs such as the possibility of purifying materials via sublimation, no use of solvents which might damage the pre-deposited layer, and the capability

to precisely control the thickness of respective layers in nanometer scale. Despite of these advantages, most vacuum-deposited OPVs still show lower efficiency than those of solution-processed OPVs. The solution-processed OPVs can be benefited from solvent additives and/or post-treatments such as solvent or thermal annealing to assist the formation of ideal nanostructures within the active layer for the better exciton separation and charge transportation. While vacuum-deposited OPVs are confronted by the difficulty in forming efficient charge transporting paths in blended active layers due to the limitation of the vacuum fabrication process, thus resulting in lower short circuit current density (J_{SC}) and fill factor (FF).[40, 100, 101] The thickness of the active layer in solution-processed polymer solar cells can be increased up to ~300 nm without the significant reduction of FF.[102] High FF of 0.66 was also demonstrated with a 400 nm thick donor layer in a vacuum-processed planar hetero-junction OPV where the donor and acceptor layers are separated.[103] However, the FF in the vacuum-deposited OPVs with mixed active layers decreases rapidly with increasing the active layer thickness.[100, 104, 105] Therefore, the thickness of the active layer in vacuum-deposited OPVs with mixed active layers is generally limited to ~60 nm to maximize the solar cell performance while maintaining a reasonable FF, although thicker active layers are typically favourable to ensure the better absorption of solar photon flux corresponding to the absorption spectrum of an active layer.[104, 105] It is inevitable for TOPVs to escape from this trade-off. Therefore, most vacuum-deposited TOPVs also have sub-cells with the active layer thinner than ~60 nm.[14, 26, 53, 57]

In this paper, we report efficient vacuum-deposited tandem organic solar cells employing thick active layers comprising of fullerenes as the acceptor and two

complementary absorbing donors. Two sub-cells are electrically connected by an interconnection unit (ICU) consisting of electron-transporting layer (ETL)/metal/*p*-doped hole-transporting layer (*p*-HTL). The introduction of the *p*-HTL in the ICU is beneficial for the higher FF of the consisting sub-cells without losing V_{OC} with the thick active layers. The *p*-HTL in the ICU also contributes to the fine tune of optical field distribution within TOPV devices, rendering the spectral responses more effective. As a result, PCE of 9.2% is achieved with higher FF of 0.62 than that of single junction sub-cells (0.54, 0.57) with relatively thick active layers of 80 nm.

6.2 Experimental

The 150 nm-thick ITO coated glass substrate with an insulator to define the active area was cleaned with acetone and isopropyl alcohol, and exposed to UV-O_3 before the film deposition. All the materials were thermally evaporated with a base pressure of $<10^{-7}$ Torr without breaking the vacuum. The evaporation rate was 0.3-0.5 Å s^{-1} except for Ag (0.05 Å s^{-1} for the recombination layer in the ICU and 4 Å s^{-1} for the cathode). The *p*-doped layer in the ICU was formed using the co-evaporation of TAPC and MoO_3 with the evaporation rate of 1 Å s^{-1} for TAPC and 0.54 Å s^{-1} for MoO_3. The evaporation rate and thickness were monitored using the quartz crystal monitor. The active area of each device was 4 mm^2 and twelve devices were fabricated to average the cell performance. After evaporation, the devices were encapsulated using an epoxy resin with glass cans in an N_2 environment before the test. The current density-voltage (*J-V*) characteristics were measured under AM 1.5G solar simulator illumination (Newport, 91160A), and

recorded using a Keithley 237 source measurement unit. The light intensity was calibrated using a standard Si-reference cell (NREL) with 100 mW cm^{-2} and kept constant for the measurement. A lock-in amplifier was used to measure the IPCE with monochromatic light from the chopped Xe lamp with 1 kHz. The intensity of the light was calibrated with a Si photodiode. For the tandem devices, two light sources, a 532 nm laser (Coherent, GLL 532 nm) and a collimated LED (Thorlabs, M735L3, wavelength of 735 nm) were used as the bias lights to excite individual sub-cells. The optical constants (*n, k*) were obtained using a spectroscopic ellipsometry.

6.3 Results and Discussion

We selected fullerenes as the acceptor and two complementary absorbing donors, 2-((2-(5-(4-(diphenylamino)phenyl)thieno[3,2-b]thiophen-2-yl)thiazol-5-yl)methylene)malononitrile (DTTz) for the visible absorption and 2-((7-(5-(dip-tolylamino)thiophen-2-yl)benzo[c]-[1,2,5]thiadiazol-4-yl)methylene)malononitrile (DTDCTB) for the near-infrared (NIR) absorption.[106, 107] Figure 6.1 shows the chemical structure of DTTz and DTDCTB and extinction coefficient (*k*) of the blended film with fullerenes in the ratio of 1:1 vol.%. To minimize absorption overlap between sub-cells, C_{70} is co-deposited with DTTz to mainly absorb the visible spectra and C_{60} blends with DTDCTB for the NIR absorption. The main absorption peak is located at the wavelength of 550 nm for the DTTz:C_{70} film and 694 nm for the DTDCTB:C_{60} film. Therefore, solar photon flux from 350 to 900 nm can be effectively utilized if the two sub-cells are efficiently connected into a tandem structure.

The current density-voltage (*J-V*) characteristics of single junction OPVs are shown in the Figure 6.2a. The device structures are configured as: ITO/MoO_3 (10

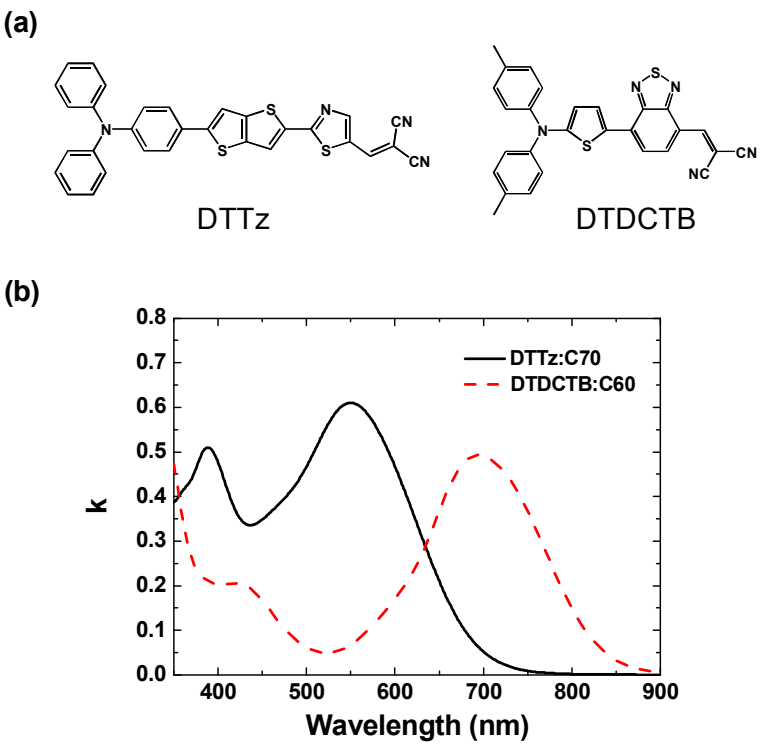

Figure 6.1 (a) Chemical structures of DTTz and DTDCTB and (b) extinction coefficients of blended films with 1:1 ratio

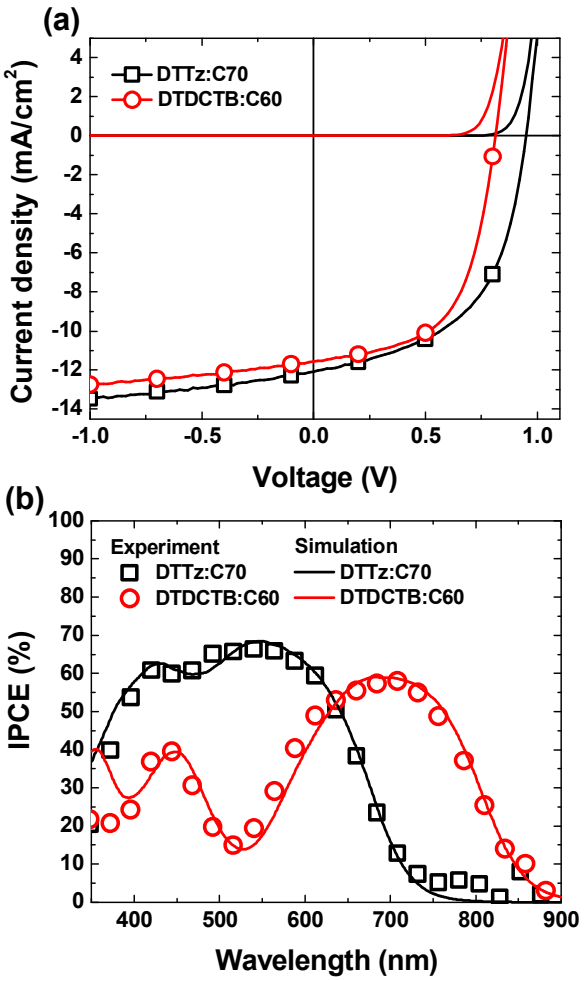

Figure 6.2 (a) The dark (solid lines) and photo (lines with symbol) current density-voltage characteristics of the single-junction solar cells and (b) the calculated (lines) and experimental (symbols) IPCE spectra of the single-junction devices

nm)/donor(5 nm)/donor:acceptor(1:1)/acceptor (5 nm)/bathocuproine (BCP):C_{60} (1:1, 5 nm)/BCP(5 nm)/Ag. The BCP:C_{60} mixed layer is used to enhance FF by suppressing the losses from bimolecular recombination and/or exciton-polaron quenching.[108] The optimized performances of the single junction OPVs are summarized in Table 6.1, which are consistent with the previously reported results.[106, 107] The efficiencies of the DTDCTB:C_{60}-based OPVs in literature are in the range of 4.4~6.1% depending on the device structure and the active layer thicknesses.[26, 99, 107] The optimum thicknesses of the active layer in the individual sub-cell devices are 50 nm for the DTTz:C_{70}-based OPV and 80 nm for the DTDCTB:C_{60}-based OPV. The incident-photon-to-electron conversion efficiencies (IPCEs) of the sub-cell devices are shown in Figure 6.2b. The DTTz:C_{70}-based OPV generates the photocurrent in the wavelength range from 350 to 700 nm, while the DTDCTB:C_{60}-based OPV harvests the photon flux mainly in the wavelength range from 500 to 900 nm. It is also noteworthy that the DTTz:C_{70}-based and DTDCTB:C_{60}-based single junction OPVs have complementary absorption ranges as shown in the IPCE spectra. Still they have similar output current values at their maximum power output point and high V_{OC}'s, which is an ideal combination for TOPVs.[109] On the contrary, the low FFs of 0.54 and 0.57 in the single junction OPVs may deteriorate the device performance of TOPVs.

The transfer matrix method coupled with the exciton diffusion equation is used to investigate the optical properties of the devices.[44, 71, 72] In the simulation, the generated excitons within the exciton diffusion lengths (L_D's) of the intrinsic DTTz, DTDCTB, C_{60} and C_{70} layers as well as the co-deposited layer are considered to contribute to the current . The L_D's of 5 nm are used for the calculation, which are

Table 6.1 Performance of the single junction solar cells. Series resistances (R_S) are obtained from the fitting of the dark *J-V* curves with the Shockley diode equation.

	PCE (%)	J_{SC} (mA/cm^2)	V_{OC} (V)	FF	R_S (Ωcm^2)
DTTz:C_{70}	6.02 ± 0.13	11.87 ± 0.13	0.95 ± 0.01	0.54 ± 0.01	4.54 ± 0.04
DTDCTB:C_{60}	5.37 ± 0.11	11.55 ± 0.19	0.81 ± 0.02	0.57 ± 0.02	5.44 ± 0.05
30 wt% TAPC:MoO_3 [1)]	5.41 ± 0.10	10.99 ± 0.14	0.81 ± 0.01	0.61 ± 0.01	3.06 ± 0.05
35 wt% TAPC:MoO_3 [1)]	5.47 ± 0.09	10.95 ± 0.18	0.81 ± 0.01	0.62 ± 0.01	2.43 ± 0.04
40 wt% TAPC:MoO_3 [1)]	5.47 ± 0.07	10.94 ± 0.14	0.80 ± 0.02	0.62 ± 0.01	2.43 ± 0.05

1) Solar cell performance of the DTDCTB:C_{60}-based OPVs with the TAPC:MoO_3 layer inserted between ITO and the intrinsic DTDCTB layer.

extracted by fitting the experimental IPCEs with the simulated results (Figure 6.3). The internal quantum efficiencies (IQEs) are obtained by matching the experimental and simulated results using the electrical losses in the devices as the parameters.[6, 26] The IQEs of the DTTz:C_{70}-based and DTDCTB:C_{60}-based OPVs are 87% and 70%, respectively. The IQE of the DTDCTB:C_{60}-based OPV is in consistency with the previous reported one.[26]

Replacing the 10 nm-thick MoO_3 layer by a 80 nm-thick of 1,1-bis-(4-bis(4-methyl-phenyl)-amino-phenyl)cyclohexane (TAPC) layer doped with MoO_3 with different doping concentrations of 30, 35 and 40 wt% between ITO and the intrinsic DTDCTB layer increases the FF from 0.57 to 0.62 with slightly reduced J_{SC} and no change in V_{OC}, as shown in Figure 6.4a and Table 6.1. The increased FF can be understood by the reduction of the series resistance (R_S) obtained from the dark J-V curves using the Shockley diode equation (Table 6.1). The replacement of the MoO_3 layer by the TAPC:MoO_3 layer reduces the R_S value of the DTDCTB:C_{60}-based OPV from 5.4 to 3.1 Ω cm^2, indicating that the TAPC:MoO_3 forms better electrical contact between ITO and the DTDCTB layer than the MoO_3 layer. The reduction of the J_{SC} originates from the reduction of IPCE near the wavelength of 700 nm (Figure 6.4b) due to the formation of the charge-transfer (CT) complexes between TAPC and MoO_3 as manifested in Figure 6.4c. The peak at the wavelength of around 300 nm in the extinction coefficient (k) spectrum originates from the intrinsic TAPC film and the peak at 690 nm is from the CT complex.[38, 69] The second peak is enlarged at the expense of the first peak with increasing the doping concentration of TAPC:MoO_3. Considering the absorption from the CT complex, the IQE is enhanced from 70 to 75% as shown in the IPCE

fitting.

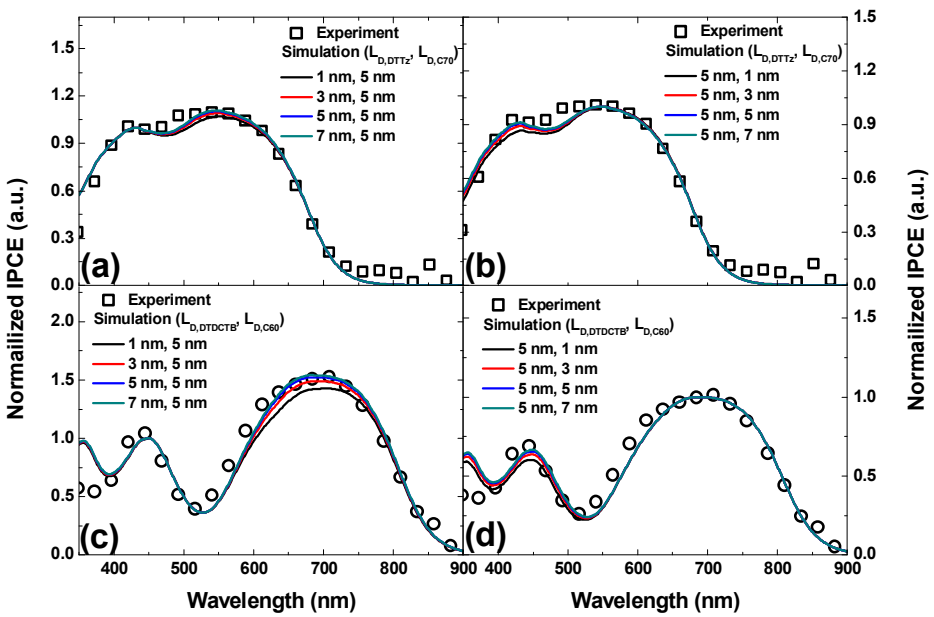

Figure 6.3 The experimental (symbols) and simulated (lines) IPCE spectra normalized at the wavelength of (a) 430 nm, (b) 550 nm, (c) 450 nm and (d) 690 nm

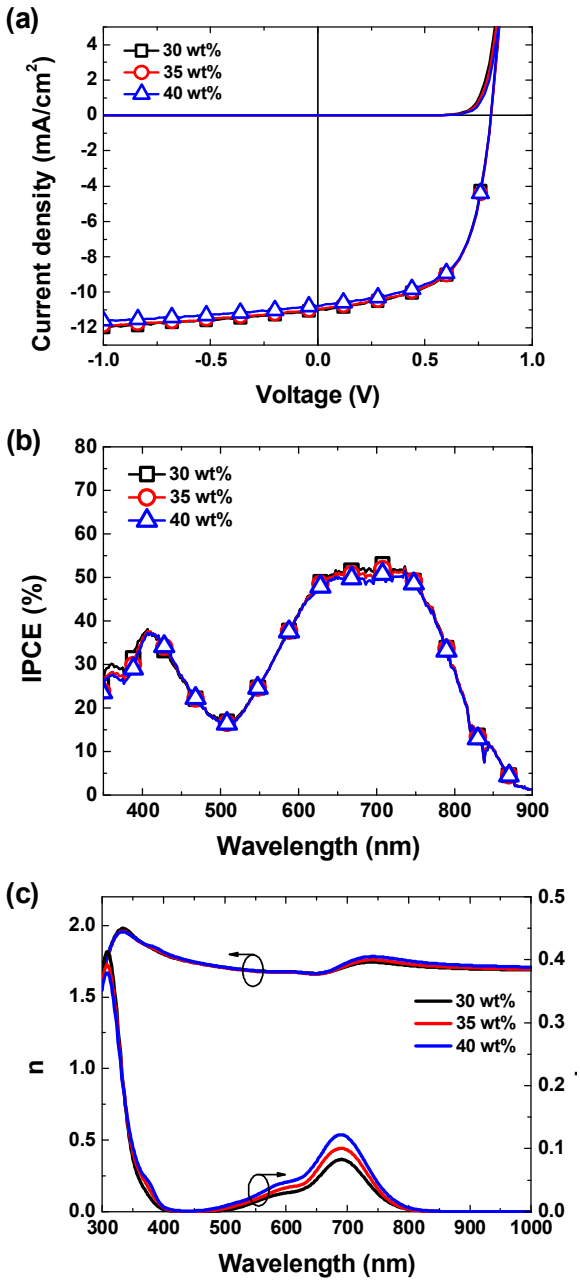

Figure 6.4 (a) The dark (solid lines) and photo (solid lines with symbol) current density-voltage characteristics of the DTDCTB:C_{60}-based OPVs with the 80 nm thick TAPC:MoO_3 layer inserted between ITO and the intrinsic DTDCTB layer with different doping concentrations and (b) their IPCE spectra. (c) The refractive indexes of the MoO_3-doped TAPC films with different doping concentrations

The ICU is one of the most important components for the design of TOPVs to maximize the performance of the consisting sub-cells. A previously reported ICU consisting of ETL/metal/*p*-HTL is used to connect the sub-cells because this structure fulfils all the requirements of optical transparency, minimized voltage losses and working as an optical spacer to match the current between the sub-cells.[77, 78, 85, 110, 111] In this work, BCP (3 nm) was used as the ETL, Ag (0.5 nm) as the metal and TAPC:MoO_3 as the *p*-HTL, respectively, in the ICU. The J_{SC} of TOPVs was calculated using the transfer matrix method as a function of the thickness of the TAPC:MoO_3 layer in the ICU for different thicknesses of the active layers of the sub-cells (See Figure 6.5) before the fabrication of devices. The simulated results reveal that rather thick active layers over 80 nm are required for both sub-cells to maximize J_{SC}. Moreover, all the TOPV devices with different thicknesses of the sub-cells require different optimized thicknesses of the TAPC:MoO_3 layer in the ICU, suggesting that this doped layer can act as an optical spacer to maximize the device performance without deteriorating the electrical characteristics.

Based on the simulation results, TOPVs with 80 nm-thick active layers of DTTz:C_{70} as the bottom cell and DTDCTB:C_{60} as the top cell are fabricated (Figure 6.6a). The *J-V* characteristics of the TOPVs are shown in Figure 4b for different thicknesses of the TAPC:MoO_3 layer in the ICU and the device performances are summarized in Table 6.2. All the devices show similar V_{OC}'s which are almost the same as the sum of the V_{OC}'s of the sub-cells although the thickness of the TAPC:MoO_3 layer is increased from 20 to 80 nm, indicating that the voltage drop in the ICU is negligible. In addition, the FF does not change as the

thickness of the TAPC:MoO_3 layer increases. To our surprise, the FF is the same as the DTDCTB:C_{60}-based OPV with

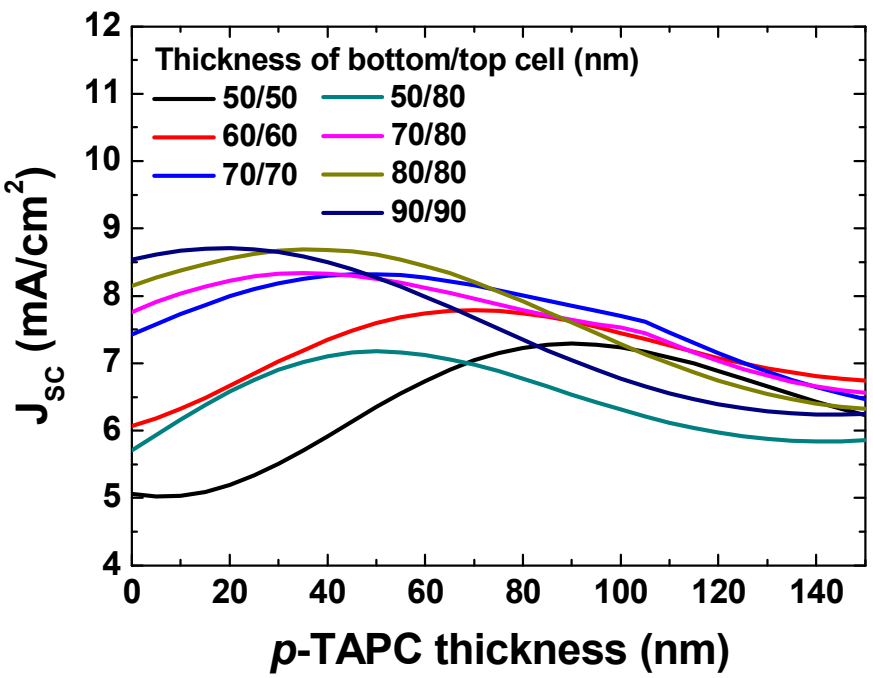

Figure 6.5 Optically calculated J_{SC} of TOPVs as a function of the thickness of the TAPC:MoO_3 layer for different thicknesses of sub-cells. The bottom cell and top cell represents DTTz:C_{70} and DTDCTB:C_{60}, respectively

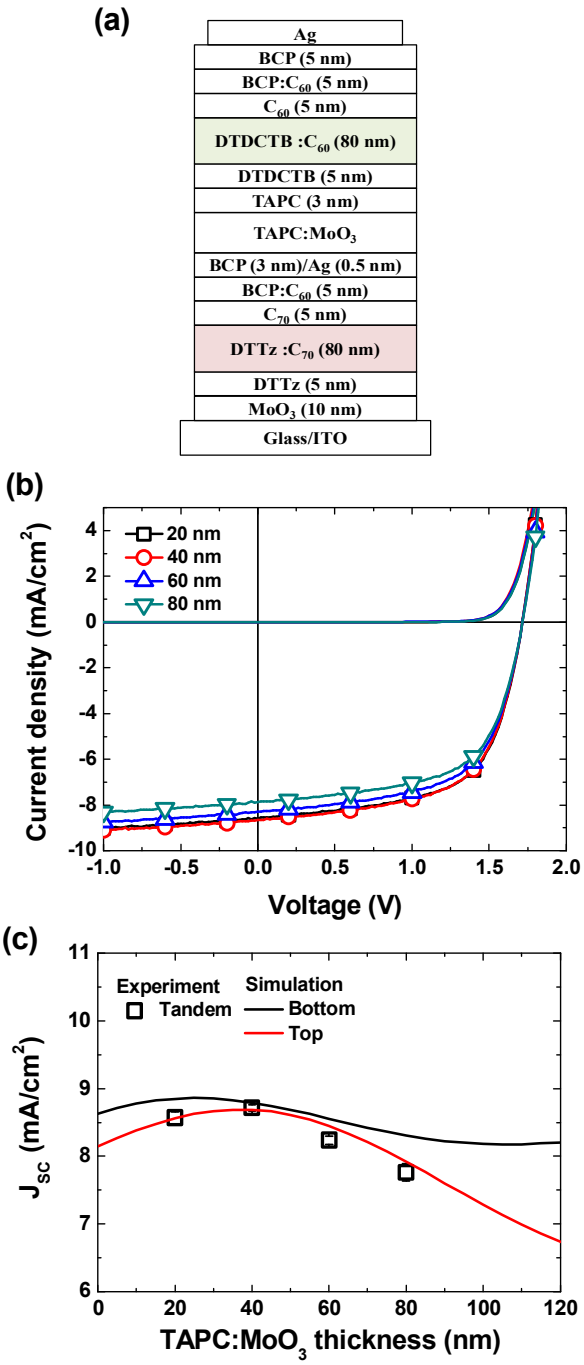

Figure 6.6 (a) The device structure of TOPVs, (b) the dark (solid lines) and photo (lines with symbol) current density-voltage characteristics of TOPVs with different thicknesses of the TAPC:MoO_3 layer in the ICU, and (c) the calculated (lines) and experimental (rectangles) J_{SC} as a function of the thickness of the TAPC:MoO_3

Table 6.2 Device performance of TOPVs with different thicknesses of the TAPC:MoO_3 layer in the ICU.

	PCE (%)	J_{SC} (mA/cm^2)	V_{OC} (V)	FF	R_S (Ωcm^2)
20 nm	9.12 ± 0.08	8.57 ± 0.09	1.71 ± 0.01	0.62 ± 0.01	8.06 ± 0.20
40 nm	9.17 ± 0.04	8.71 ± 0.05	1.71 ± 0.01	0.62 ± 0.01	7.94 ± 0.13
60 nm	8.55 ± 0.11	8.24 ± 0.06	1.70 ± 0.01	0.61 ± 0.01	7.59 ± 0.28
80 nm	8.12 ± 0.16	7.75 ± 0.13	1.71 ± 0.01	0.61 ± 0.01	8.51 ± 0.18

TAPC:MoO_3 layer which is higher than the FF of the another single junction DTTz:C_{70}-based OPV (0.54). That can be understood from the optical simulation shown in Figure 4c which predicts that the J_{SC} of the TOPV is limited by the top cell (DTDCTB:C_{60}). Figure 4c also shows that the theoretically predicted J_{SC} is well matched with the experimental J_{SC} even with the 80 nm-thick TAPC:MoO_3 layer in the ICU, revealing that there is no additional electrical losses from the ICU. In other words, the device performance of TOPVs can be optimized using the optical simulation without the consideration of the additional electrical losses of the ICU if the TAPC:MoO_3 layer is used in the ICU.

Figure 6.7 shows the IPCE spectra of TOPVs for different thicknesses of the TAPC:MoO_3 layer in the ICU. To extract the spectral response from the individual sub-cells, two bias lights (735 nm light from a collimated light-emitting diode (LED) for the bottom cell and 532 nm light from a laser for the top cell) are used. As predicted from the extinction coefficient of the blended films, the sub-cells are spectrally complementary and the visible region is mainly absorbed by the bottom cell (DTTz:C_{70}) and the NIR region by the top cell (DTDCTB:C_{60}). As the thickness of the TAPC:MoO_3 layer in the ICU increases, the IPCE intensity of the bottom cell at the wavelength of 540 nm is reduced whereas the wavelength of 400 nm is increased. In contrast, the IPCE intensity of the top cell at the wavelength of 730 nm is unchanged when the thickness of the TAPC:MoO_3 layer increases from 20 to 40 nm, but is reduced upon further increase of the TAPC:MoO_3 layer thickness. All the IPCE spectra are well matched with the theoretical ones calculated using the transfer matrix method.

Variation of the IPCE spectra with the thickness of the ICU can be understood by

the

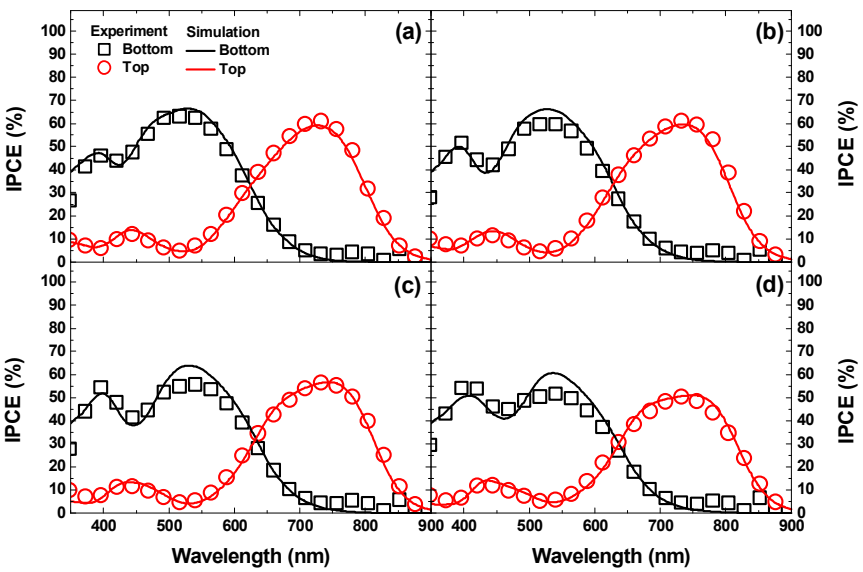

Figure 6.7 The calculated (lines) and experimental (symbols) IPCE spectra of the bottom cell (rectangular) and the top cell (circle) with different thicknesses of the TAPC:MoO_3 layer: a) 20, b) 40, c) 60, and d) 80 nm

interference effect in TOPVs. Figure 6.8 shows the distributions of the optical intensity obtained using the transfer matrix method at the wavelength of 530 nm and 730 nm, representing the selective absorption for the bottom cell and the top cell, respectively. The bottom cell and top cell are located in the peak positions of the optical intensity of their absorption wavelengths (530 nm for the bottom and 730 nm for the top cells, respectively) when the thickness of the TAPC:MoO_3 layer is 40 nm (Figure 6.8a). In contrast, the 80 nm-thick ICU (Figure 6.8b) results in lower optical intensity at the wavelength of 530 nm in the bottom cell to lower J_{SC} than the 40 nm-thick ICU. This fact demonstrates that the optical simulation with the consideration of IQEs obtained from the single junctions can be used to predict the device performance before the fabrication of devices because the ICU does not increase the electrical loss.

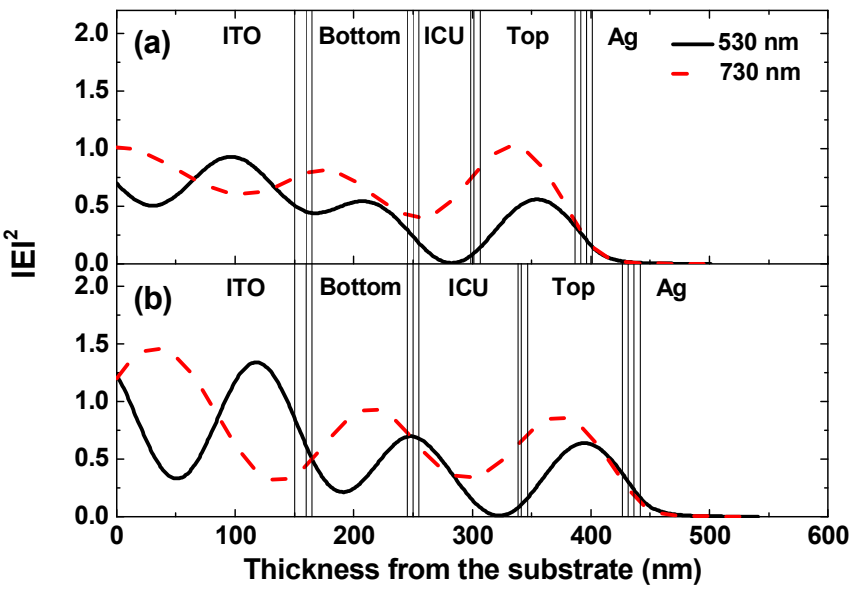

Figure 6.8 Optical intensity distributions at the wavelengths of 530 and 730 nm are presented on schematic device structures of tandem devices with different thicknesses of the TAPC:MoO_3 layer of a) 40 and b) 80 nm

6.4 Conclusion

We report efficient vacuum-deposited tandem organic photovoltaic cells with two complementary absorbing donors, DTTz for the visible absorption and DTDCTB for the near-infrared absorption. Two sub-cells are connected by the interconnection unit (ICU) composed of electron-transporting layer/metal/*p*-doped hole-transporting layer. The J_{SC} and IPCEs of the TOPVs are well matched with the theoretical calculation based on the transfer matrix method coupled with the exciton diffusion equation. The parameters for the calculation including the IQEs and the exciton diffusion lengths in the sub-cells were extracted from the single junction devices. The use of TAPC:MoO_3 as the *p*-HTL in the ICU provides large flexibility in tuning the sub-cell position and thereby maximizing J_{SC} of TOPVs without sacrificing electrical characteristics. Moreover, the *p*-HTL reduces the contact resistance for hole extraction to enhances the FF of TOPVs which is identical to one of the single junction sub-cells (DTDCTB:C_{60}) with the TAPC:MoO_3 layer and even much higher than another sub-cell (DTTz:C_{70}). All combined effect allows us to fabricate a high efficiency TOPV with PCE of 9.2%, J_{SC} of 8.7 mA cm^{-2}, V_{OC} of 1.71 V and FF of 0.62 with relatively thick active layers of 80 nm.

Chapter 7. Efficient vacuum-deposited ternary organic solar cells with broad absorption, energy transfer and enhanced hole mobility

7.1 Introduction

The performance of organic photovoltaics (OPVs) have been improved impressively in the past several years. The power conversion efficiencies (PCEs) have reached around 10% in single-junction solar cells.[2-4, 49] Despite these progress, the efficiency is still lower than inorganic counterparts, mainly due to the narrow absorption band of organic materials, resulting in lower short-circuit current density (J_{SC}).[16, 64, 112]

The concept of ternary OPVs with two donors or acceptors in the active layer has been widely studied to boost efficiencies by broadening absorption spectra with much simpler fabrication method than the tandem structures.[18, 96, 113-117] To date, ternary OPVs by the solution process using polymers have been successfully demonstrated to reach the PCE of 9.2% with more than 20% efficiency enhancement as compared to the binary devices.[17, 18, 116, 117] In the vacuum process with small molecules, however, ternary OPVs have not shown much progress although it has several advantages such as the ease of purifying materials via sublimation and no use of solvent. Especially, in the solution process, different solvents are preferred in different binary devices because the selection of the solvent affects the film morphology critically.[118-121] Therefore, it can be difficult to select a common solvent for the formation of the ternary layer where one more material needs to be dissolved in one solvent as compared to the binary layer.

Vacuum-deposited ternary OPVs are only recently reported using two donors,

chloroindium phthalocyanine (ClInPc) and boron subphthalocyanine chloride (SubPc), co-deposited with C_{60}.[122] The absorption range is successfully extended to the near-infrared (NIR) region due to the complementary absorption of two donors. However, the devices showed poor performance with the PCE of 2.08%, which is lower than that of binary systems. A few requirements need to be fulfilled to improve the device performance in ternary OPVs compared to binary devices. Firstly, two donors or acceptors should have the complementary absorption to efficiently use solar photon flux. If absorption overlap is large, the enhancement of the J_{SC} would be limited due to the optical losses. Secondly, cascade energy levels are needed to ensure efficient charge transports. If not, the charges can be trapped and recombined in the active layer due to the energetic barriers, resulting in the reduction of the J_{SC} and fill factor (FF). Especially, it is critical for charges generated in the materials with small amount in the ternary layer because the probability of the molecules surrounded by another molecules is increased. This might cause the isolation of the charges without the contribution to the current. In addition, the energy transfer to the molecules having higher mobility between two donors or acceptors in the ternary layer is favored to enhance electrical properties of the devices because charges can be transported to the electrode via the molecules with higher mobility.

In this paper, efficient vacuum-deposited ternary OPVs are demonstrated using two donors, 2-((2-(5-(4-(diphenylamino)phenyl)thieno[3,2-b]thiophen-2-yl)thiazol-5-yl)methylene)malononitrile (DTTz) for the visible absorption and 2-((7-(5-(dip-tolylamino)thiophen-2-yl)benzo[c]-[1,2,5]thiadiazol-4-yl)methylene)malononitrile (DTDCTB) for the NIR absorption, co-deposited with C_{70} in the ternary layer. The

PCE of 8.02% for the ternary device is achieved, which is 23% higher than that of the binary OPVs. To our best knowledge, this is the highest efficiency and the first demonstration to have an improvement of the device performance in the vacuum-deposited ternary OPVs, which are comparable to the solution-processed devices. This enhancement originates from incorporating two donors with the complementary absorption and increased hole mobility due to the cascade energy levels and the energy transfer from the low mobility donor to the high mobility donor, which meets all the requirements for efficient ternary OPVs.

7.2 Experimental

The 150 nm-thick ITO coated glass substrate with an insulator to define the active area was cleaned with acetone and isopropyl alcohol, and exposed to UV-O_3 before the film deposition. All the materials were thermally evaporated with a base pressure of $<10^{-7}$ Torr without breaking the vacuum. The evaporation rate was varied from 0.03 Å s^{-1} to 0.5 Å s^{-1} in order to control the compositions of ternary layers. The evaporation rate and thickness were monitored using quartz crystal monitor. After evaporation, the devices were encapsulated using an epoxy resin with glass cans in an N_2 environment before the test. The active area of each device is 4 mm^2 and more than eight devices were fabricated to average the device performance. The UV-vis absorption spectra of the films were recorded with a VARIAN Cary 5000 UV-vis spectrophotometer. In the PL measurements, a continuous wave laser (325 nm, Melles Griot) was used as an excitation source and the PL spectra were measured by a fiber optic spectrometer (Ocean Optics Maya2000). The optical constants (*n, k*) were obtained using a spectroscopic

ellipsometry. The current density-voltage (*J-V*) characteristics were measured under AM 1.5G solar simulator illumination (Newport, 91160A), and recorded using a Keithley 237 source measurement unit. The light intensity was calibrated using a standard Si-reference cell (NREL) with 100 mW cm^{-2} and kept constant for the measurement. A lock-in amplifier was used to measure the IPCE with monochromatic light from the chopped Xe lamp with 1 kHz.

7.3 Results and Discussion

Chemical structures of DTTz and DTDCTB used in the ternary OPVs are shown in Figure 7.1a and their highest occupied molecular orbital (HOMO) and lowest unoccupied molecular orbital (LUMO) energy levels are summarized in Figure 7.1b.[106, 107] Figure 7.1c displays the normalized absorption spectra of the pristine DTTz and DTDCTB films. The visible region is mainly absorbed by DTTz with the absorption peak at the wavelength of 530 nm and near-infrared by DTDCTB at 670 nm. The complementary absorption of the two donors enable the efficient use of solar photon flux from the wavelength of 300 nm to 900 nm. In the previous results, we used the two donors as sub-cells in the tandem OPVs to achieve the PCE of 9.2%.[123] The absorption profiles for ternary blend films with different compositions are shown in Figure 7.1d. The absorption at the wavelength from 450 nm to 650 nm is reduced, while the one from 650 nm to 900 nm is enhanced with increasing the DTDCTB composition in the blend films as expected.

Figure 7.2a displays the current density-voltage (*J-V*) characteristics of the binary and ternary OPVs with different compositions. The device structures are ITO/1,1-bis-(4-bis(4-methyl-phenyl)-amino-phenyl)cyclohexane (TAPC):MoO_3 (20

nm)/TAPC (3 nm)/DTDCTB (5 nm)/active layer (50 nm)/C_{70} (5 nm)/bathocuproine (BCP):C_{60} (5 nm)/BCP (5 nm)/Ag. The TAPC:MoO_3 layer with the intrinsic TAPC layer is used to enhance the hole extraction from the active layer to ITO.[124] For the

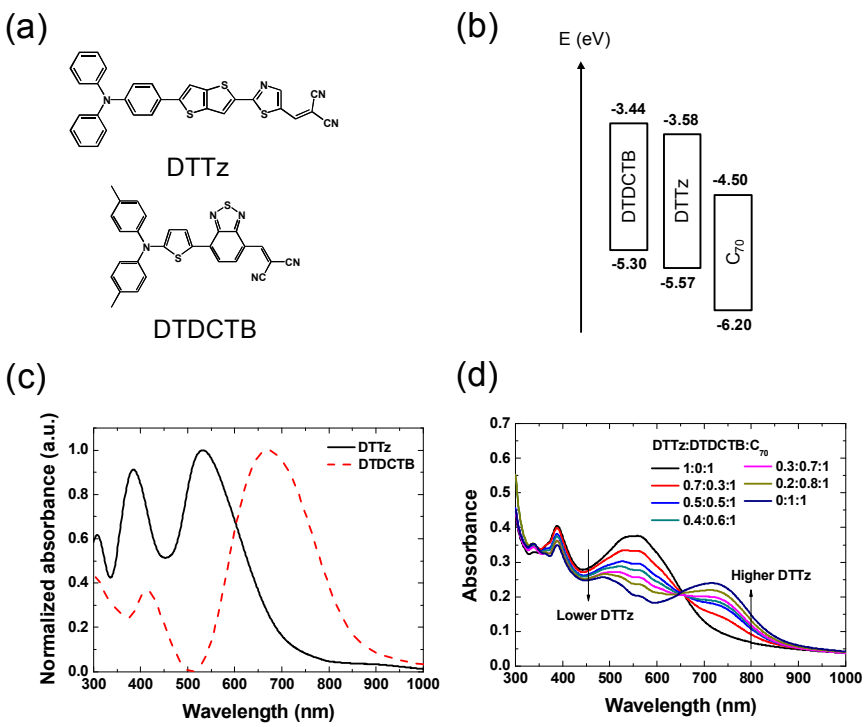

Figure 7.1 (a) Chemical structures of DTTz and DTDCTB. (b) Energy levels of DTTz, DTDCTB and C_{70}. (c) Normalized absorbance spectra of DTTz and DTDCTB. (d) Absorbance spectra of ternary films with different compositions

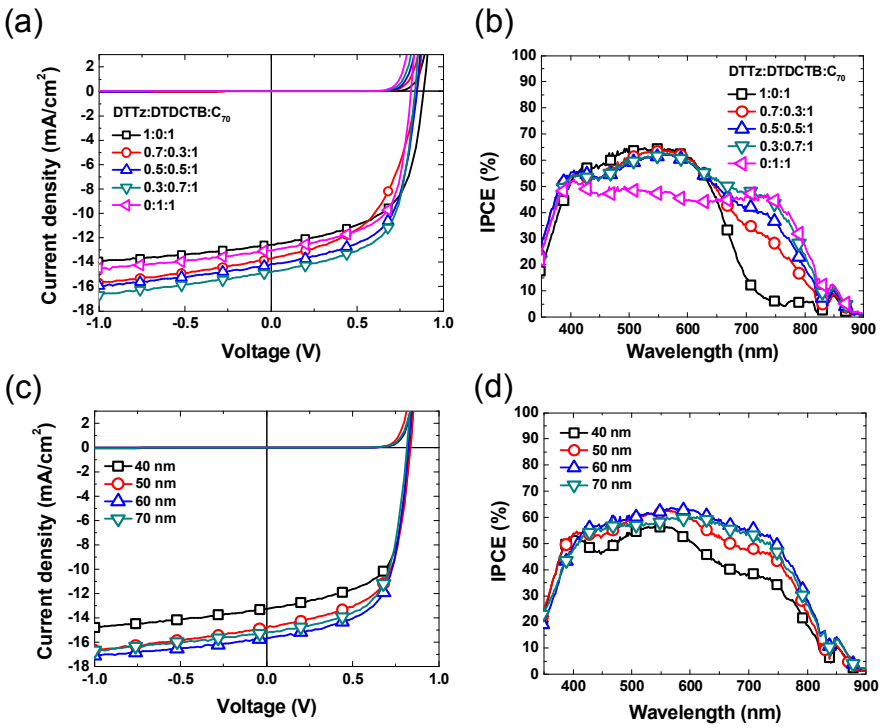

Figure 7.2 (a) *J-V* characteristics and (b) IPCE of ternary OPVs with different compositions. (c) *J-V* characteristics and (d) IPCE of the devices as a function of the ternary layer thickness

enhancement of electrical properties in the devices, the BCP:C_{60} mixed layer is also inserted between C_{70} and BCP layer.[108] The composition of C_{70} in the active layer of the ternary

OPVs is maintained with 50% because both the binary devices based on DTTz and DTDCTB are optimized at the composition of 1:1 (donor:C_{70}). The binary OPVs show similar efficiencies of 6.5% as summarized in Table 7.1. The open-circuit voltage (V_{OC}) of the DTTz:C_{70}-based OPV is higher than that of the DTDCTB:C_{70}-based OPV due to the higher gap between the HOMO level of the donor and the LUMO level of the acceptor. In the ternary devices, the J_{SC} is enhanced significantly up to 14.64 mA cm^{-2} with the gradual reduction of the V_{OC} as the composition of DTDCTB in the blend layer increases (see Figure 7.3). The change of the V_{OC} is a common phenomenon when two donors or acceptors having different HOMO or LUMO levels are used in ternary OPVs.[116, 125-127] This can be explained by the formation of electronic alloy charge-transfer states.[117, 127] When the composition of the donor with the higher HOMO level is gradually increased in the blend layer, the interfacial bandgap become smaller continuously, resulting in the reduction of the V_{OC} because V_{OC} is proportional to the interfacial bandgap between the HOMO level of the donor and the LUMO level of the acceptor. In this system, DTDCTB has the higher HOMO level than DTTz. Therefore, the V_{OC} is gradually reduced with increasing the composition of DTDCTB in the ternary layer. The enhancement of the J_{SC} originates from the additional photocurrent, generated from the complementary absorption by the DTTz and DTDCTB molecules, covering the whole visible and NIR spectra of sun light as shown in the incident photon-to-electron conversion efficiency (IPCE) spectra (Figure 7.2b). The change

Table 7.1 The device performance with different compositions of the ternary layer. The thickness of the ternary layer is 50 nm

DTTz:DTDCTB:C_{70}	PCE (%)	J_{SC} (mA cm^{-2})	J_{SC}[1)] (mA cm^{-2})	V_{OC} (V)	FF	R_S (Ωcm^2)	R_P (10^5 Ωcm^2)
1:0:1	6.52 ± 0.09	12.61 ± 0.14	11.86	0.89 ± 0.01	0.58 ± 0.01	3.05	13.95
0.7:0.3:1	5.78 ± 0.17	13.22 ± 0.29	13.21	0.86 ± 0.01	0.51 ± 0.01	2.25	0.68
0.5:0.5:1	7.04 ± 0.16	14.00 ± 0.19	13.86	0.85 ± 0.02	0.60 ± 0.01	2.62	2.54
0.3:0.7:1	7.45 ± 0.12	14.64 ± 0.18	14.56	0.83 ± 0.02	0.61 ± 0.01	2.03	16.56
0:1:1	6.52 ± 0.25	13.17 ± 0.17	12.85	0.81 ± 0.01	0.61 ± 0.02	2.28	5.45

[1)] J_{SC} is calculated from IPCE data

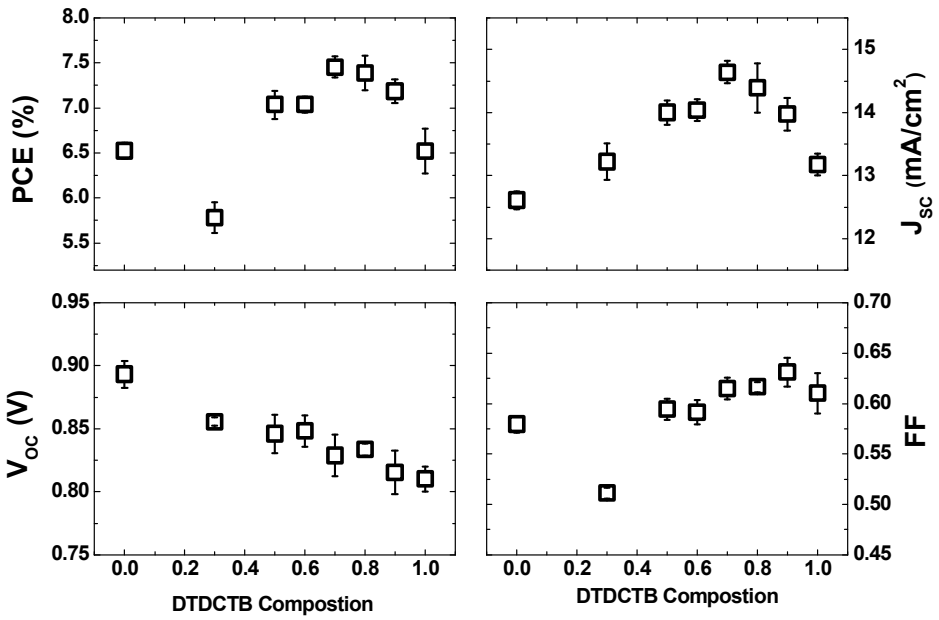

Figure 7.3 Solar cell performances as a function of DTDCTB portion in the ternary layer

is in good agreement with the absorption profiles shown in Figure 7.1d. Surprisingly, however, the IPCE at the wavelength of 400 nm to 650 nm is maintained almost constant even though the absorption by DTTz is reduced with increasing the composition of DTDCTB in the blend layer. This is related to the electrical properties of active layer with the energy transfer, which is discussed later. The device with the composition of 0.7:0.3:1 (DTTz:DTDCTB:C_{70}) shows higher field-dependent photocurrent with a low FF. This is likely due to the low hole mobility in the blend film because the composition of DTDCTB possessing higher hole mobility than DTTz is below the percolation threshold in the blend layer, which will be discussed further later. As a result, the probability of the charge recombination is increased in the blend layer under given electric field and higher electric field is required to extract charges to the electrodes.

The device structure was further optimized by varying the thickness of the ternary layer from 40 nm to 70 nm at the composition of 0.3:0.7:1 (DTTz:DTDCTB:C_{70}), and the results are shown in Figure 7.2c with the device parameters summarized in Table 7.2. The J_{SC} is enhanced up to 15.47 mA cm^{-2} when the thickness of the ternary layer is changed from 40 nm to 60 nm and decreased with further increase of the thickness, while the V_{OC} and FF are not changed significantly with the value of 0.83 V and 0.62 at the thickness of 60 nm. In the vacuum-deposited OPVs, the FF is reduced critically with increasing the thickness of the active layer due to the increase of the resistance in the film.[100, 104, 105] In this system, however, the FF remains almost constant with relatively high value of 0.63 although the thickness of the active layer is increased to 70 nm, meaning that electrical properties of the devices are not deteriorated with increasing the thickness. The optimized device

shows the PCE of

Table 7.2 The device performance with different thicknesses of the ternary layer

	PCE (%)	J_{SC} (mA cm^{-2})	J_{SC}[1)] (mA cm^{-2})	V_{OC} (V)	FF	R_S (Ωcm^2)	R_P (10^5 Ωcm^2)
40 nm	6.77 ± 0.10	13.01 ± 0.18	12.49	0.84 ± 0.01	0.62 ± 0.01	2.53	0.27
50 nm	7.45 ± 0.12	14.64 ± 0.18	14.56	0.83 ± 0.02	0.61 ± 0.01	2.03	16.56
60 nm	8.02 ± 0.09	15.47 ± 0.16	15.66	0.83 ± 0.01	0.62 ± 0.01	2.50	2.77
70 nm	7.77 ± 0.09	15.11 ± 0.16	15.03	0.82 ± 0.02	0.63 ± 0.01	2.42	0.29

[1)] J_{SC} is calculated from IPCE data

8.02%, which is 23% enhancement compared to the binary OPVs. To our best knowledge, the efficiency is the highest one in vacuum-processed OPVs and this is also the first demonstration of a ternary OPV having higher efficiency than the binary OPVs fabricated by the vacuum deposition.

The transfer matrix method was used to understand the variation of the J_{SC} of the ternary devices with the composition and thickness of the active layer.[71, 77] The refractive indices of the ternary films with different compositions were obtained using the linear combination of the binary films as shown in Figure 7.4a. The absorbance spectra of the films with different compositions calculated using the transfer matrix method with the refractive indices are well matched with the experimental ones as shown in Figure 7.5, verifying that the linear combination works well in this system. This good match also indicates that there is no additional transition state or aggregation originating from the interaction between two donors. The calculated IPCEs of the OPVs with different compositions without considering the electrical loss are shown in Figure 7.4b.The calculated IPCE is reduced at the wavelength from 450 nm to 650 nm and increased at the wavelength from 650 nm to 900 nm with the reduction of the DTTz composition in the ternary layer, which is consistent with the absorption spectra shown in Figure 7.1d. Interestingly, however, the calculated IPCEs are different from the experimental ones at the wavelength from 450 nm to 650 nm, corresponding to the absorption by the DTTz molecules. The experimental IPCE is not significantly reduced although the absorption of the active layer is decreased.

The difference between the experimental and calculated IPCEs can be understood from the energy transfer from DTTz to DTDCTB and increased hole mobility with

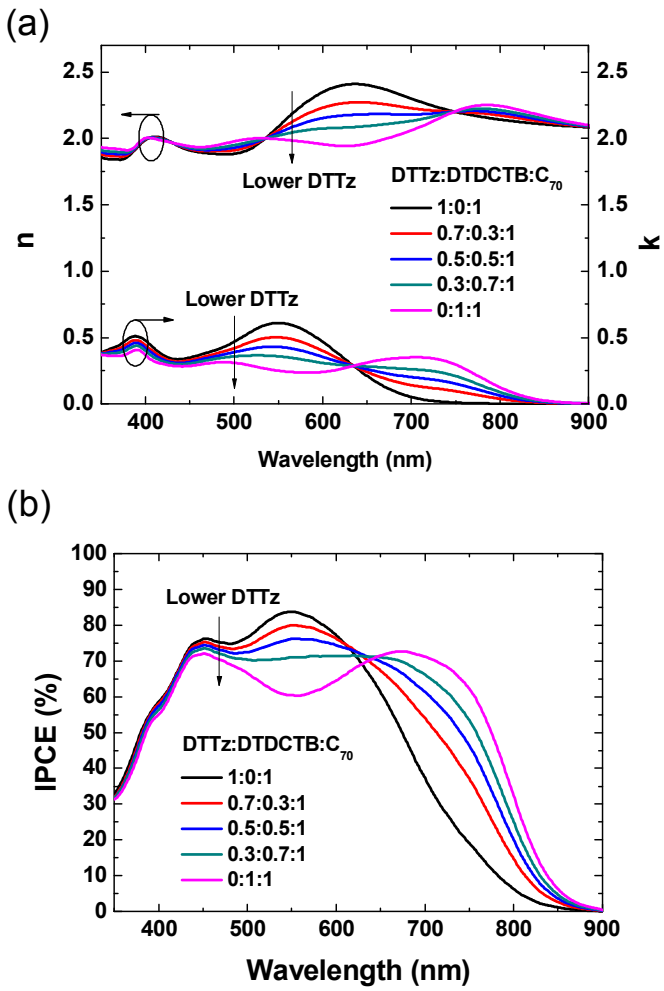

Figure 7.4 (a) Optical constants of ternary films with different compositions. (b) Calculated IPCE spectra of ternary OPVs

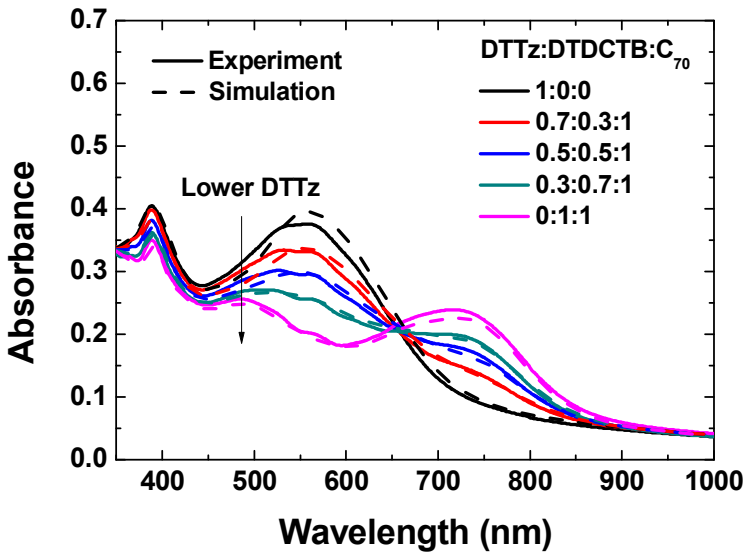

Figure 7.5 Experimental (lines) and simulated (dotted lines) absorbance of the ternary films

increasing the composition of DTDCTB in the blend layers. The photoluminescence (PL) spectra from the DTTz (30 nm), DTDCTB (70 nm) and DTTz:DTDCTB (3:7, 100 nm) films are shown in Figure 7.6. The thicknesses of the films were controlled to maintain the same number of molecules between the intrinsic and blend layers. The intrinsic DTTz film shows one PL peak at the wavelength of 780 nm, while the DTDCTB films have three peaks at 520 nm, 745 nm and 880 nm. DTDCTB has the absorption peaks at 305 nm, 415 nm and 670 nm originating from the electronic transitions from S_0 to S_4 and S_5, S_0 to S_2 and S_3 and S_0 to S_1, respectively.[107] The PL peaks might be related to these transitions in the reverse direction. When DTTz is co-deposited with DTDCTB, the peak of DTTz disappears and three peaks are shown at the wavelength of 490 nm, 745 nm and 880 nm. Compared to the PL spectra of the intrinsic DTDCTB film, the first peak is blue-shifted and the PL intensity at 880 nm is increased. The peak shift in the blend film is related to the increase of the distance between DTDCTB molecules when DTTz is mixed with DTDCTB to reduce the intermolecular interaction. The increase of the PL intensity at 880 nm and no emission from DTTz indicates that the energy transfer from DTTz to DTDCTB is efficient due to the large overlap between the emission spectrum of DTTz and the S_0 to S_1 absorption of DTDCTB.

The difference between the experimental and calculated IPCEs can be also understood from the charge mobilities of the mixed films measured by the single carrier devices. The device structures are ITO/MoO_3 (5 nm)/donor or blend layer (100 nm)/MoO_3 (10 nm)/Al and Al/ blend layer (100 nm)/LiF (1 nm)/Al for hole- and electron-only devices, respectively. The mobilities extracted from the space

charge-limited current in the pristine and blend films (See Figure 7.7) are shown in

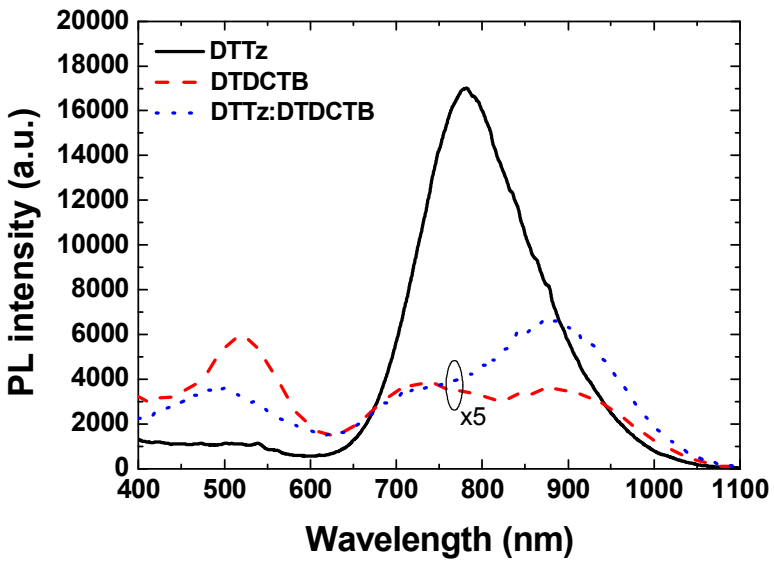

Figure 7.6 PL spectra of intrinsic and blend films excited at the wavelength of 325 nm. The PL intensities of the DTDCTB and DTTz:DTDCTB were enlarged five times for the clarity.

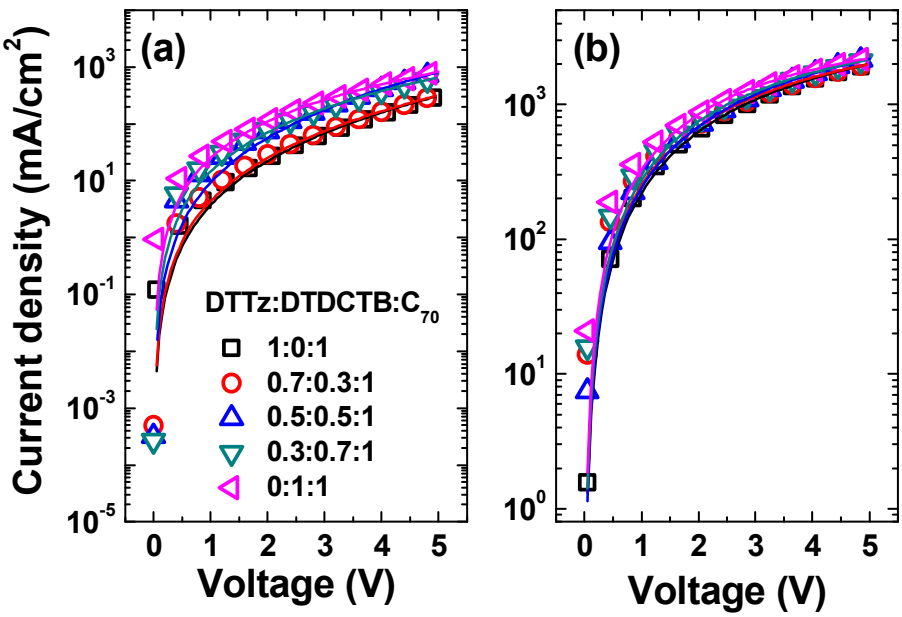

Figure 7.7 *J-V* characteristics of (a) hole-only devices and (b) electron-only devices. Solid lines are the fitted curves using SCLC model

Figure 7.8. The mobilities of pristine materials are 1.43×10^{-7} cm^2 V^{-1} s^{-1}, 9.24×10^{-5} cm^2 V^{-1} s^{-1} and 1.11×10^{-3} cm^2 V^{-1} s^{-1} for DTTz, DTDCTB and C_{70}, respectively. In the blend films the hole mobility in the DTDCTB:C_{70} film is 16 times higher than that in DTTz:C_{70}, while the electron mobility is almost the same. The high hole mobility in the DTDCTB:C_{70} film results in higher FF in the DTDCTB:C_{70}-based device than that of the DTTz:C_{70}-based device. The electron mobilities of both binary and ternary layers remain unchanged because the composition of C_{70} is the same as 50% in the layers. In contrast, the large difference in hole mobility between DTDCTB and DTTz results in gradual increase in the hole mobility in the ternary layer with increasing the DTDCTB composition. This fact indicates that holes dissociated at the interface between DTTz and C_{70} in the ternary solar cells are transferred to DTDCTB and transported along DTDCTB to the anode due to the higher lying HOMO level of DTDCTB than DTTz (Figure 7.1b). The fact that the IPCE in the wavelength of 400 nm to 650 nm is maintained almost constant with increasing the composition of DTDCTB in the blend layer even though the absorption by DTTz is reduced can be understood by the increase of the charge collection efficiency coming from the increased hole mobility, compensating the reduction of the absorption coming from the reduced number of DTTz molecules. All the facts reveal that the enhanced J_{SC} of the ternary OPVs compared to the binary devices can be ascribed to the broad absorption by using two complimentary donors covering from visible to NIR region and higher hole mobility in the ternary layer than one of the binary layers consisting of one donor and C_{70}, combined with the energy transfer from the donor with lower hole mobility to the one with higher mobility.

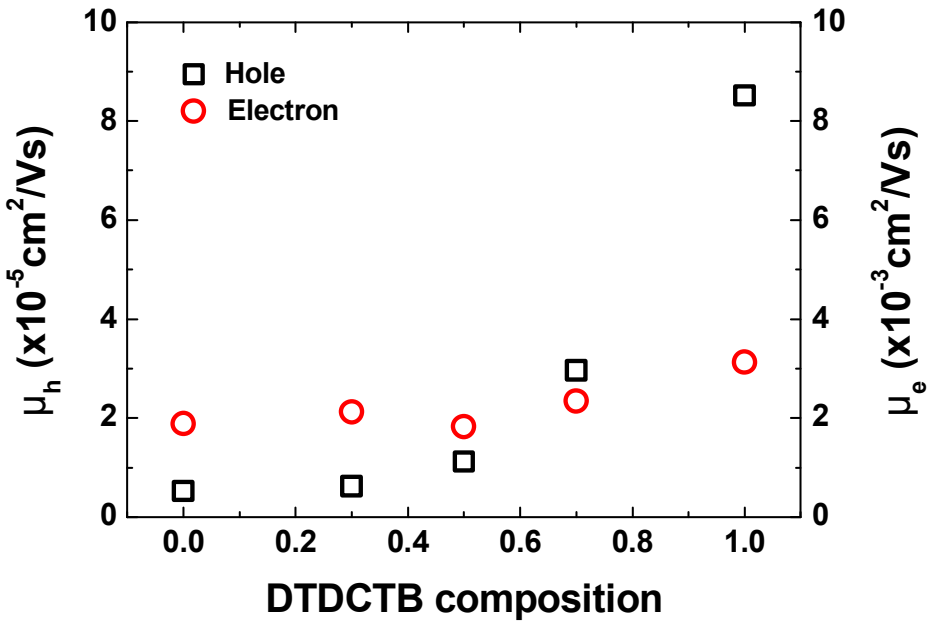

Figure 7.8 Hole and electron mobility of ternary films with different compositions

7.4 Conclusion

In summary, we have demonstrated remarkable enhancement of the device performance in vacuum-deposited ternary OPVs as compared to the binary devices. The PCE of 8.02% was achieved, which is 23% higher than that of the binary devices. The combination of DTTz and DTDCTB shows the complementary absorption covering from the wavelength of 350 nm to 900 nm and higher hole mobility in the ternary layer than one of the binary layers consisting of one donor and C_{70}, combined with the energy transfer from the donor (DTTz) with lower hole mobility to the one with higher mobility (DTDCTB), which satisfy all the requirements for efficient ternary OPVs. This system demonstrates the possibility to enhance device performance using vacuum-deposition.

Chapter 8. Summary and outlook

In the past several years, organic photovoltaics (OPVs) have shown large progress due to the low cost, ease of fabrication method and flexible applications. However, OPVs show still lower performance than the inorganic solar cells. The main difference is the absorption spectra, responding to the solar photon flux. The organic materials have the narrow absorption window, resulting in lower short-circuit current density (J_{SC}) in OPVs although the absorption coefficient is higher than inorganic materials. To overcome this limitation, advanced device structures need to be developed. In this thesis, the answers to how efficiently the solar irradiance can be used to generate electricity in the devices are suggested.

In chapter 2, the templating effect is introduced to control the crystal structure of the active material. The thin templating layer, CuI, induces increase of the crystallinity with preferred orientation of active material, PbPc, resulting in the extension of the absorption into the near-infrared (NIR) region with almost twice enhancement of the J_{SC}. The FF is also enhanced due to the formation of the better contact between ITO and the PbPc layer.

In terms of device architectures, tandem OPVs (TOPVs) which consist of two identical sub-cells connected by the interconnection unit (ICU) are one of the choices to broaden the absorption spectra of the devices as shown in chapter 3-6. For efficient TOPVs, the active materials used in the sub-cells should have complementary absorption to reduce optical losses. Moreover, the ICU should fulfill all the requirements such as the transparency in the active range, aligning energy levels of the sub-cells to reduce voltage losses and the tunable thickness

without the decrease of the conductivity for the current matching between the sub-cells. In chapter 3, newly designed ICU, electron-transporting layer (HTL)/metal/*p*-doped hole-transporting layer (*p*-HTL) is suggested. This structure meet all the requirements of the efficient ICU. Their working mechanism is demonstrated using different doping concentration of the *p*-HTL of the ICU in chapter 4. In TOPVs, the V_{OC} is related with the difference between the fermi level and the HOMO level (E_F-E_{HOMO}) of the *p*-HTL. The FF is affected by the conductivity of the *p*-HTL as well as the depletion width at the interface between metal and the *p*-HTL. In chapter 5, it is explained that the charge generation efficiency (CGE) is an important parameter to select the *p*-HTL. The higher CGE reduce the E_F-E_{HOMO} of the *p*-HTL, resulting in the decrease of the voltage loss in the ICU. From the understanding of the working mechanism of newly designed ICU, the highly efficient vacuum-deposited TOPV with power conversion efficiency of 9.2% is realized as shown in chapter 6.

In chapter 7, another device concept of ternary OPVs having two donors with an acceptor in the active layer is demonstrated. A few requirements need to be fulfilled to improve the device performance in ternary OPVs compared to binary devices. Firstly, two donors or acceptors should have the complementary absorption to efficiently use solar photon flux. Secondly, cascade energy levels are needed to ensure efficient charge transports. In addition, the energy transfer to the molecules having higher mobility between two donors or acceptors in the ternary layer is favored to enhance electrical properties of the devices. From these considerations, 23% enhancement of the efficiency in the ternary OPVs is achieved as compared to the binary systems. To our best knowledge, this is the highest efficiency and the

first demonstration to have an improvement of the device performance in the vacuum-deposited ternary OPVs, which are comparable to the solution-processed devices.

In this thesis, methods to broaden and extend the absorption spectra into NIR region are suggested by the novel design of device structures with analysis of their working mechanisms. We believe that our results are applied not only to the presented device structures but also to other systems including solution-processed devices. Moreover, the efficiency of organic solar cells can be higher than that of inorganic counterparts if the low-bandgap materials having a high mobility and proper energy levels are developed and combined with our results in the devices.

Bibliography

1. C. W. Tang, *Appl. Phys. Lett.*, 1986, 48, 183.
2. J. Subbiah, B. Purushothaman, M. Chen, T. Qin, M. Gao, D. Vak, F. H. Scholes, X. Chen, S. E. Watkins, G. J. Wilson, A. B. Holmes, W. W. Wong and D. J. Jones, *Adv. Mater.*, 2015, 27, 702.
3. Q. Zhang, B. Kan, F. Liu, G. Long, X. Wan, X. Chen, Y. Zuo, W. Ni, H. Zhang, M. Li, Z. Hu, F. Huang, Y. Cao, Z. Liang, M. Zhang, T. P. Russell and Y. Chen, *Nat. Photonics*, 2014, 9, 35.
4. L. Huo, T. Liu, X. Sun, Y. Cai, A. J. Heeger and Y. Sun, *Adv. Mater.*, 2015, 27, 2938.
5. Y. Liu, J. Zhao, Z. Li, C. Mu, W. Ma, H. Hu, K. Jiang, H. Lin, H. Ade and H. Yan, *Nat. Commun.*, 2014, 5, 5293.
6. http://www.pveducation.org/pvcdrom/pn-junction/absorption-coefficient
7. Z. Chen, P. Cai, J. Chen, X. Liu, L. Zhang, L. Lan, J. Peng, Y. Ma and Y. Cao, *Adv. Mater.*, 2014, 26, 2586.
8. M. Wang, H. Wang, T. Yokoyama, X. Liu, Y. Huang, Y. Zhang, T. Q. Nguyen, S. Aramaki and G. C. Bazan, *J. Am. Chem. Soc.*, 2014, 136, 12576.
9. K. D. Deshmukh, T. Qin, J. K. Gallaher, A. C. Y. Liu, E. Gann, K. O'Donnell, L. Thomsen, J. M. Hodgkiss, S. E. Watkins and C. R. McNeill, *Energy Environ. Sci.*, 2015, 8, 332.
10. J. Yang and D. Yan, *Chem. Soc. Rev.*, 2009, 38, 2634.
11. J. W. Kim, H. J. Kim, T.-M. Kim, T. G. Kim, J.-H. Lee, J. W. Kim and J.-J.

Kim, *Curr. Appl. Phys.*, 2013, 13, 7.

12. K. Vasseur, K. Broch, A. L. Ayzner, B. P. Rand, D. Cheyns, C. Frank, F. Schreiber, M. F. Toney, L. Froyen and P. Heremans, *ACS Appl. Mater. Interfaces*, 2013, 5, 8505.
13. T.-M. Kim, H.-S. Shim, M.-S. Choi, H. J. Kim and J.-J. Kim, *ACS Appl. Mater. Interfaces*, 2014, 6, 4286.
14. M. Riede, C. Uhrich, J. Widmer, R. Timmreck, D. Wynands, G. Schwartz, W.-M. Gnehr, D. Hildebrandt, A. Weiss, J. Hwang, S. Sundarraj, P. Erk, M. Pfeiffer and K. Leo, *Adv. Funct. Mater.*, 2011, 21, 3019.
15. W. Li, A. Furlan, K. H. Hendriks, M. M. Wienk and R. A. Janssen, *J. Am. Chem. Soc.*, 2013, 135, 5529.
16. K. Cnops, B. P. Rand, D. Cheyns, B. Verreet, M. A. Empl and P. Heremans, *Nat. Commun.*, 2014, 5, 3406.
17. L. Lu, T. Xu, W. Chen, E. S. Landry and L. Yu, *Nat. Photonics*, 2014, 8, 716.
18. Y. Yang, W. Chen, L. Dou, W.-H. Chang, H.-S. Duan, B. Bob, G. Li and Y. Yang, *Nat. Photonics*, 2015, 9, 190.
19. B. Verreet, R. Müller, B. P. Rand, K. Vasseur and P. Heremans, *Org. Electron.*, 2011, 12, 2131.
20. K. Vasseur, B. P. Rand, D. Cheyns, L. Froyen and P. Heremans, *Chem. Mater.*, 2011, 23, 886.
21. D. Placencia, W. Wang, R. C. Shallcross, K. W. Nebesny, M. Brumbach and N. R. Armstrong, *Adv. Funct. Mater.*, 2009, 19, 1913.
22. W. Wang, D. Placencia and N. R. Armstrong, *Org. Electron.*, 2011, 12, 383.

23. T.-M. Kim, H. J. Kim, H.-S. Shim, M.-S. Choi, J. W. Kim and J.-J. Kim, *J. Mater. Chem. A*, 2014, 2, 8730.

24. J. Yang, R. Zhu, Z. Hong, Y. He, A. Kumar, Y. Li and Y. Yang, *Adv. Mater.*, 2011, 23, 3465.

25. P. Peumans, S. Uchida and S. R. Forrest, *Nat.* 2003, 425, 158.

26. D. Cheyns, M. Kim, B. Verreet and B. P. Rand, *Appl. Phys. Lett.*, 2014, 104, 093302.

27. B. P. Rand, J. Xue, F. Yang and S. R. Forrest, *Appl. Phys. Lett.*, 2005, 87, 233508.

28. J. Dai, X. Jiang, H. Wang and D. Yan, *Appl. Phys. Lett.*, 2007, 91, 253503.

29. L. Shen, Y. Xu, X. Zhang, F. Meng, S. Ruan and W. Chen, *Sol. Energy Mater. Sol. Cells*, 2010, 94, 2451.

30. T. Kaji, M. Zhang, S. Nakao, K. Iketaki, K. Yokoyama, C. W. Tang and M. Hiramoto, *Adv. Mater.*, 2011, 23, 3320.

31. M. Hiramoto, K. Kitada, K. Iketaki and T. Kaji, *Appl. Phys. Lett.*, 2011, 98, 023302.

32. A. Miyamoto, K. Nichogi, A. Taomoto, T. Nambu and M. Murakami, *Thin Solid Films*, 1995, 256, 64.

33. L. Ottaviano, L. Lozzi, A. R. Phani, A. Ciattoni, S. Santucci and S. D. Nardo, *Appl. Surf. Sci*., 1998, 136, 81.

34. K. Mizoguchi, K. Mizui, D. Kim and M. Nakayama, *Jpn. J. Appl. Phys.*, 2002, 41, 6421.

35. G. D. Sharma, V. S. Choudhary and M. S. Roy, *Sol. Energy Mater. Sol. Cells*, 2007, 91, 1087.

36. T. Sakurai, T. Ohashi, H. Kitazume, M. Kubota, T. Suemasu and K. Akimoto, *Org. Electron.*, 2011, 12, 966.

37. W. Zhao, J. P. Mudrick, Y. Zheng, W. T. Hammond, Y. Yang and J. Xue, *Org. Electron.*, 2012, 13, 129.

38. J.-H. Lee, D.-S. Leem, H.-J. Kim and J.-J. Kim, *Appl. Phys. Lett.*, 2009, 94, 123306.

39. C. H. Cheng, J. Wang, G. T. Du, S. H. Shi, Z. J. Du, Z. Q. Fan, J. M. Bian and M. S. Wang, *Appl. Phys. Lett.*, 2010, 97, 083305.

40. J. W. Kim, H. J. Kim, H. H. Lee, T. Kim and J.-J. Kim, *Adv. Funct. Mater.*, 2011, 21, 2067.

41. H. J. Kim, J. W. Kim, H. H. Lee, T.-M. Kim, J. Jang and J.-J. Kim, *J. Phys. Chem. Lett.*, 2011, 2, 1710.

42. H. J. Kim, J. W. Kim and J.-J. Kim, *Electron. Mater. Lett.*, 2011, 7, 93.

43. H. J. Kim, H. H. Lee, J. W. Kim, J. Jang and J.-J. Kim, *J. Mater. Chem.*, 2012, 22, 8881.

44. J. Lee, S.-Y. Kim, C. Kim and J.-J. Kim, *Appl. Phys. Lett.*, 2010, 97, 083306.

45. R. R. Lunt, J. B. Benziger and S. R. Forrest, *Adv. Mater.*, 2010, 22, 1233.

46. S.-B. Rim, R. F. Fink, J. C. Schöneboom, P. Erk and P. Peumans, *Appl. Phys. Lett.*, 2007, 91, 173504.

47. W.-I. Jeong, J. Lee, S.-Y. Park, J.-W. Kang and J.-J. Kim, *Adv. Funct. Mater.*, 2011, 21, 343.

48. W.-I. Jeong, Y. E. Lee, H.-S. Shim, T.-M. Kim, S.-Y. Kim and J.-J. Kim, *Adv. Funct. Mater.*, 2012, 22, 3089.

49. L. Dou, J. You, J. Yang, C.-C. Chen, Y. He, S. Murase, T. Moriarty, K. Emery, G. Li and Y. Yang, *Nat. Photonics*, 2012, 6, 180.

50. B. Joon Lee, H. Jung Kim, W.-i. Jeong and J.-J. Kim, *Sol. Energy Mater. Sol. Cells*, 2010, 94, 542.

51. R. Schueppel, R. Timmreck, N. Allinger, T. Mueller, M. Furno, C. Uhrich, K. Leo and M. Riede, *J. Appl. Phys.*, 2010, 107, 044503.

52. D. Cheyns, B. P. Rand and P. Heremans, *Appl. Phys. Lett.*, 2010, 97, 033301.

53. M. Zhang, H. Wang and C. W. Tang, *Org. Electron.*, 2012, 13, 249.

54. B. E. Lassiter, J. D. Zimmerman, A. Panda, X. Xiao and S. R. Forrest, *Appl. Phys. Lett.*, 2012, 101, 063303.

55. J. Li, Q.-Y. Bao, H.-X. Wei, Z.-Q. Xu, J.-P. Yang, Y.-Q. Li, S.-T. Lee and J.-X. Tang, *J. Mater. Chem.*, 2012, 22, 6285.

56. J. Yang, W. Chen, B. Yu, H. Wang and D. Yan, *Org. Electron.*, 2012, 13, 1018.

57. J. A. Macko, R. R. Lunt, T. P. Osedach, P. R. Brown, M. C. Barr, K. K. Gleason and V. Bulovic, *Phys. Chem. Chem. Phys.*, 2012, 14, 14548.

58. B. Lüssem, M. Riede and K. Leo, *Phys. Status Solidi A*, 2013, 210, 9.

59. R. Timmreck, S. Olthof, K. Leo and M. K. Riede, *J. Appl. Phys.*, 2010, 108, 033108.

60. D.-S. Leem, J.-H. Lee, J.-J. Kim and J.-W. Kang, *Appl. Phys. Lett.*, 2008, 93, 103304.

61. H. Kanno, R. J. Holmes, Y. Sun, S. Kena-Cohen and S. R. Forrest, *Adv. Mater.*, 2006, 18, 339.

62. Y.-E. Lee, S.-Y. Kim, W.-I. Jeong and J.-J. Kim, *Sol. Energy Mater. Sol. Cells*, 2013, 114, 59.

63. K. H. An, B. O'Connor, K. P. Pipe and M. Shtein, *Org. Electron.*, 2009, 10, 1152.

64. H.-S. Shim, H. J. Kim, J. W. Kim, S.-Y. Kim, W.-I. Jeong, T.-M. Kim and J.-J. Kim, *J. Mater. Chem.*, 2012, 22, 9077.

65. J.-H. Lee, P.-S. Wang, H.-D. Park, C.-I. Wu and J.-J. Kim, *Org. Electron.*, 2011, 12, 1763.

66. S. Lee, J.-H. Lee, J.-H. Lee and J.-J. Kim, *Adv. Funct. Mater.*, 2012, 22, 855.

67. D.-H. Kim, T.-M. Kim, W.-I. Jeong and J.-J. Kim, *Appl. Phys. Lett.*, 2012, 101, 153303.

68. H. Jung Kim, H.-S. Shim, J. Whan Kim, H. Hwi Lee and J.-J. Kim, *Appl. Phys. Lett.*, 2012, 100, 263303.

69. J.-H. Lee, D.-S. Leem and J.-J. Kim, *Org. Electron.*, 2010, 11, 486.

70. L. Cattin, F. Dahou, Y. Lare, M. Morsli, R. Tricot, S. Houari, A. Mokrani, K. Jondo, A. Khelil, K. Napo and J. C. Bernède, *J. Appl. Phys.*, 2009, 105, 034507.

71. L. A. A. Pettersson, L. S. Roman and O. Inganäs, *J. Appl. Phys.*, 1999, 86, 487.

72. P. Peumans, A. Yakimov and S. R. Forrest, *J. Appl. Phys.*, 2003, 93, 3693.

73. M. Riede, T. Mueller, W. Tress, R. Schueppel and K. Leo, *Nanotechnology*, 2008, 19, 424001.

74. M. He, F. Qiu and Z. Lin, *J. Phys. Chem. Lett.*, 2013, 4, 1788.

75. T. Ameri, N. Li and C. J. Brabec, *Energy Environ. Sci.*, 2013, 6, 2390.

76. J. You, L. Dou, K. Yoshimura, T. Kato, K. Ohya, T. Moriarty, K. Emery, C. C. Chen, J. Gao, G. Li and Y. Yang, *Nat. Commun.*, 2013, 4, 1446.

77. H.-S. Shim, S.-Y. Kim, J. Whan Kim, T.-M. Kim, C.-H. Lee and J.-J. Kim, *Appl. Phys. Lett.*, 2013, 102, 203903.

78. E. New, T. Howells, P. Sullivan and T. S. Jones, *Org. Electron.*, 2013, 14, 2353.

79. J.-H. Lee and J.-J. Kim, *Phys. Status Solidi A*, 2012, 209, 1399.

80. M. Kröger, S. Hamwi, J. Meyer, T. Dobbertin, T. Riedl, W. Kowalsky and H.-H. Johannes, *Phys. Rev. B*, 2007, 75.

81. V. I. Adamovich, S. R. Cordero, P. I. Djurovich, A. Tamayo, M. E. Thompson, B. W. D'Andrade and S. R. Forrest, *Org. Electron.*, 2003, 4, 77.

82. S.-J. Yoo, J.-H. Lee, J.-H. Lee and J.-J. Kim, *Appl. Phys. Lett.*, 2013, 102, 183301.

83. W. Tress, K. Leo and M. Riede, *Adv. Funct. Mater.*, 2011, 21, 2140.

84. J. D. Zimmerman, B. E. Lassiter, X. Xiao, K. Sun, A. Dolocan, R. Gearba, D. A. V. Bout, K. J. Stevenson, P. Wickramasinghe, M. E. Thompson and S. R. Forrest, *ACS NANO*, 2013, 7, 9268.

85. H.-S. Shim, J.-H. Chang, S.-J. Yoo, C.-I. Wu and J.-J. Kim, *J. Mater. Chem. A*, 2014, 2, 5450.

86. I. Salzmann, G. Heimel, S. Duhm, M. Oehzelt, P. Pingel, B. M. George, A. Schnegg, K. Lips, R. P. Blum, A. Vollmer and N. Koch, *Phys. Rev. Lett.*, 2012, 108, 035502.

87. P. Pingel and D. Neher, *Phys. Rev. B*, 2013, 87.

88. M. L. Tietze, L. Burtone, M. Riede, B. Lüssem and K. Leo, *Phys. Rev. B*, 2012, 86.

89. I. W. Wu, Y.-H. Chen, P.-S. Wang, C.-G. Wang, S.-H. Hsu and C.-I. Wu, *Appl. Phys. Lett.*, 2010, 96, 013301.

90. N. Wang, J. Yu, Y. Zheng, Z. Guan and Y. Jiang, *J. Phys. Chem. C*, 2012, 116, 5887.

91. S. W. Liu, W. C. Su, C. C. Lee, C. F. Lin and C. H. Yuan, *J. Electrochem. Soc.*, 2012, 159, H871.

92. A. K. Kyaw, D. H. Wang, D. Wynands, J. Zhang, T. Q. Nguyen, G. C. Bazan and A. J. Heeger, *Nano Lett.*, 2013, 13, 3796.

93. S. Woo, W. Hyun Kim, H. Kim, Y. Yi, H.-K. Lyu and Y. Kim, *Adv. Energy Mater.*, 2014, 4, 1301692.

94. B. Kan, Q. Zhang, M. Li, X. Wan, W. Ni, G. Long, Y. Wang, X. Yang, H. Feng and Y. Chen, *J. Am. Chem. Soc.*, 2014, 136, 15529.

95. Y. H. Chen, L. Y. Lin, C. W. Lu, F. Lin, Z. Y. Huang, H. W. Lin, P. H. Wang, Y. H. Liu, K. T. Wong, J. Wen, D. J. Miller and S. B. Darling, *J. Am. Chem. Soc.*, 2012, 134, 13616.

96. T. Ameri, T. Heumüller, J. Min, N. Li, G. Matt, U. Scherf and C. J. Brabec, *Energy Environ. Sci.*, 2013, 6, 1796.

97. A. R. bin Mohd Yusoff, S. J. Lee, H. P. Kim, F. K. Shneider, W. J. da Silva and J. Jang, *Adv. Funct. Mater.*, 2014, 24, 2240.

98. C. C. Chen, W. H. Chang, K. Yoshimura, K. Ohya, J. You, J. Gao, Z. Hong and Y. Yang, *Adv. Mater.*, 2014, 26, 5670.

99. X. Che, X. Xiao, J. D. Zimmerman, D. Fan and S. R. Forrest, *Adv. Energy*

Mater., 2014, 4, 1400568.

100. R. Pandey, A. A. Gunawan, K. A. Mkhoyan and R. J. Holmes, *Adv. Funct. Mater.*, 2012, 22, 617.

101. X. Xiao, J. D. Zimmerman, B. E. Lassiter, K. J. Bergemann and S. R. Forrest, *Appl. Phys. Lett.*, 2013, 102, 073302.

102. W. Li , K. H. Hendriks , W. S.C. Roelofs , Y. Kim , M. M. Wienk and R. A. J. Janssen, *Adv. Mater.*, 2013, 25, 3182.

103. B. Verreet, P. Heremans, A. Stesmans and B. P. Rand, *Adv. Mater.*, 2013, 25, 5504.

104. Y.-Q. Zheng, W. J. Potscavage, T. Komino, M. Hirade, J. Adachi and C. Adachi, *Appl. Phys. Lett.*, 2013, 102, 143304.

105. G. Chen, H. Sasabe, Z. Wang, X. F. Wang, Z. Hong, Y. Yang and J. Kido, *Adv. Mater.*, 2012, 24, 2768.

106. J. Kim, H.-S. Shim, H. Lee, M.-S. Choi, J.-J. Kim and Y. Seo, *J. Phys. Chem. C*, 2014, 118, 11559.

107. L. Y. Lin, Y. H. Chen, Z. Y. Huang, H. W. Lin, S. H. Chou, F. Lin, C. W. Chen, Y. H. Liu and K. T. Wong, *J. Am. Chem. Soc.*, 2011, 133, 15822.

108. X. Xiao, K. J. Bergemann, J. D. Zimmerman, K. Lee and S. R. Forrest, *Adv. Energy Mater.*, 2014, 4, 1301557.

109. B. E. Lassiter, C. Kyle Renshaw and S. R. Forrest, *J. Appl. Phys.*, 2013, 113, 214505.

110. H.-S. Shim, J.-H. Chang, C.-I. Wu and J.-J. Kim, *Org. Electron.*, 2014, 15, 1805.

111. Y.-H. Chen, C.-W. Chen, Z.-Y. Huang, K.-T. Wong, L.-Y. Lin, F. Lin and

H.-W. Lin, *Org. Electron.*, 2014, 15, 1828.

112. S.-Y. Kim, J.-H. Lee, H.-S. Shim and J.-J. Kim, *Org. Electron.*, 2013, 14, 1496.

113. H. C. Hesse, J. Weickert, C. Hundschell, X. Feng, K. Müllen, B. Nickel, A. J. Mozer and L. Schmidt-Mende, *Adv. Energy Mater.*, 2011, 1, 861.

114. H. Cha, D. S. Chung, S. Y. Bae, M.-J. Lee, T. K. An, J. Hwang, K. H. Kim, Y.-H. Kim, D. H. Choi and C. E. Park, *Adv. Funct. Mater.*, 2013, 23, 1556.

115. S.-J. Ko, W. Lee, H. Choi, B. Walker, S. Yum, S. Kim, T. J. Shin, H. Y. Woo and J. Y. Kim, *Adv. Energy Mater.*, 2015, 5, 1401687.

116. Y. Zhang, D. Deng, K. Lu, J. Zhang, B. Xia, Y. Zhao, J. Fang and Z. Wei, *Adv. Mater.*, 2015, 27, 1071.

117. L. Lu, W. Chen, T. Xu and L. Yu, *Nat. Commun.*, 2015, 6, 7327.

118. Y. Chen, S. Zhang, Y. Wu and J. Hou, *Adv. Mater.*, 2014, 26, 2744.

119. N. Zhou, H. Lin, S. J. Lou, X. Yu, P. Guo, E. F. Manley, S. Loser, P. Hartnett, H. Huang, M. R. Wasielewski, L. X. Chen, R. P. H. Chang, A. Facchetti and T. J. Marks, *Adv. Energy Mater.*, 2014, 4, 1300785.

120. W. Cai, P. Liu, Y. Jin, Q. Xue, F. Liu, T. P. Russell, F. Huang, H.-L. Yip and Y. Cao, *Adv. Sci.*, 2015, DOI: 10.1002/advs.201500095.

121. H. Choi, S. J. Ko, T. Kim, P. O. Morin, B. Walker, B. H. Lee, M. Leclerc, J. Y. Kim and A. J. Heeger, *Adv. Mater.*, 2015, 27, 3318.

122. G. Williams and H. Aziz, *Org. Electron.*, 2015, 17, 229.

123. H.-S. Shim, F. Lin, J. Kim, B. Sim, T.-M. Kim, C.-K. Moon, C.-K. Wang, Y. Seo, K.-T. Wong and J.-J. Kim, *Adv. Energy Mater.*, 2015, 5, 1500228.

124. M.-S. Choi, T.-M. Kim, H.-S. Shim, B.-S. Kim, H. J. Kim and J.-J. Kim,

ACS Appl. Mater. Interfaces, 2015, 7, 9134.

125. R. A. Street, D. Davies, P. P. Khlyabich, B. Burkhart and B. C. Thompson, *J. Am. Chem. Soc.*, 2013, 135, 986.

126. P. Cheng, Y. Li and X. Zhan, *Energy Environ. Sci.*, 2014, 7, 2005.

127. R. A. Street, P. P. Khlyabich, A. E. Rudenko and B. C. Thompson, *J. Phys. Chem. C*, 2014, 118, 26569.

초 록

유기태양전지는 최근 몇 년 동안 눈부신 발전을 이루었다. 그러나 무기물에 비해 유기물은 좁은 흡수 영역을 가지고 있기 때문에, 유기태양전지는 무기태양전지 대비 상대적으로 낮은 에너지변환효율을 보이고 있다. 따라서, 효율을 증대시키기 위해서는 소자의 흡수 영역을 근적외선 영역까지 넓혀 보다 넓은 파장범위의 빛을 전류로 변환시키는 것이 필요하다. 본 학위논문에서는 새로운 소자구조 설계를 통해 흡수 영역을 늘리고, 각 소자구조의 작동원리에 대한 연구 결과를 기술하였다.

제 2장에서는 copper iodide (CuI)와 lead phthalocyanine (PbPc)를 탬플릿층과 광활성층으로 사용하여 탬플릿층에 의해 광활성화층의 결정구조를 조절하는 탬플릿 효과에 대하여 논의하였다. ITO와 PbPc층 사이에 삽입된 CuI는 PbPc의 결정도를 향상시키고 방위배열 (方位配列, preferred orientation)을 유도하였다. 또한 엑시톤 확산거리를 증가시켜 전류 생성에 기여하는 엑시톤의 수를 늘렸고 이를 통해 단락전류가 향상되었다. 또한, 탬플릿층으로 사용된 CuI는 ITO와 PbPc층 사이에 전위장벽을 줄여주는 역할을 하여 접촉저항을 줄임으로 써, 충진률을 향상시켰다. 위 결과를 통해 소자의 흡수 영역은 1000nm의 파장까지 증대되었고, 에너지변환효율은 2배 가까이 증가하였다.

2개의 단위소자가 중간전극을 통해 전기적으로 연결되어있는 적층형 유기태양전지에 대해 제3-6장에서 논의하였다. 2개의 단위 소자가 상호보완적인 흡수를 가지고 있다면, 적층형 유기태양전지는 넓은 범위의 파장

을 전류변환에 이용할 수 있는 장점을 가지고 있다. 효과적인 적층형 유기태양전지를 구현하기 위해서는 중간전극의 역할이 무엇보다 중요하다. 중간전극의 요구사항으로는 (1) 광학손실을 줄이기 위해 단위소자가 흡수하는 영역에서는 투명해야 하고, (2) 전압손실을 줄이기 위해 두 단위소자간 에너지준위를 맞춰주어야 한다. 또한, (3) 두 단위소자간 전류를 맞춰주는 광학 스페이서 역할을 위해 전기적 손실 없이 두께 조절이 가능해야 한다. 제 3장에서는 새로운 중간전극구조 (전자수송층/메탈/*p*-도핑된 홀수송층)을 제안하였다. 이 구조는 중간전극의 모든 요구사항 충족하였고, 이를 실험적으로 검증하였다. 제 4장에서는 새로 제안한 중간전극의 작동원리를 규명하였다. 중간전극내 *p*-도핑층의 페르미준위와 HOMO 준위의 차이가 적층형 유기태양전지에서 개방전압을 결정짓는 중요한 요소라는 것을 실험적으로 입증하였고, 충진률은 *p*-도핑층의 전기전도도와 메탈과 *p*-도핑층 사이에 생성되는 공핍층의 두께 (depletion width)와 관련 있다는 사실을 밝혔다. 제 5장에서는 전하생성효율이 다른 3가지 도펀트를 중간전극 내의 *p*-도핑층에 사용해 적층형 유기태양전지를 제작하였고, 전하생성효율이 높을수록 개방전압의 손실이 줄어든다는 것을 보였다. 이는 중간전극 내의 *p*-도핑층을 선정할 때 전하생성효율을 고려해야 한다는 것을 보여준다. 제 6장에서는 새로 제안된 중간전극의 작동원리에 대한 이해를 바탕으로, 중간전극과 상호보완적인 흡수를 가지고 있는 2가지 물질 (DTTz:C_{70}, DTDCTB:C_{60})을 단위소자로 사용하여 9.2%라는 높은 효율의 적층형 유기태양전지를 구

현하였다.

흡수영역을 늘릴 수 있는 또 다른 소자구조인 3종혼합 유기태양전지에 대한 연구 및 결과를 제 7장에서 기술하였다. 3종혼합 유기태양전지는 기존 소자와 달리 2개 이상의 도너 혹은 억셉터를 광활성층에 사용한 구조로써, 각 물질이 상호보완적인 흡수를 가지고 있다면 기존 소자보다 넓은 파장범위의 태양광을 효과적으로 사용할 수 있는 장점과 소자를 구성하는 층의 수가 적층형 유기태양전지보가 적기 때문에 적층형 유기태양전지보다 제작이 용이하다는 장점을 가지고 있다. 본 연구에서는 DTTz와 DTDCTB라는 2가지 도너와 C_{70}를 억섭터로 사용하여 3종혼합 유기태양전지를 구성하였고, 8.02%라는 에너지변환효율을 달성하여, 세계 최초로 진공증착을 통해 제작한 기존 소자구조인 2종혼합 유기태양전지 대비 23% 향상된 결과를 구현하였다. 3종혼합 유기태양전지의 효율이 증대된 원인은 2개의 도너가 상호보완적인 흡수를 가지고 있어서 350 nm 부터 900 nm의 넓은 파장의 태양광을 사용할 수 있었고, DTTz로부터 DTDCTB로 에너지 전달과 정공 이동을 통해 정공이동도가 더 빠른 DTDCTB 분자를 따라서 생성된 정공이 전극으로 이동할 수 있었기 때문이다.

본 학위본문에서는, 다양한 구조 설계 및 작동원리 규명을 통해 소자의 흡수 영역을 근적외선까지 늘릴 수 있는 방법에 대한 연구결과를 기술하였다. 이 결과는 용액공정 및 다양한 유기태양전지 분야에 응용될 수 있고, 높은 전하이동도 및 작은 밴드갭을 가지는 새로운 유기물이 개발되

어 본 연구결과와 결합된다면, 더 높은 효율을 가지는 유기태양전지를 제작할 수 있을 것으로 기대된다.

주요어: 유기태양전지, 탬플릿층, 중간전극, 적층형 유기태양전지, 3종혼합 유기태양전지

학번: 2010-22760

List of Publications

1. **Hyun-Sub Shim**, Chang-Ki Moon, Jihun Kim, Chun-Kai Wang, Bomi Sim, Francis Lin, Ken-Tsung Wong, Yongsok Seo and Jang-Joo Kim, Efficient Vacuum-Deposited Ternary Organic Solar Cells by Broad Absorption with Energy Transfer and Enhanced Hole Mobility, *ACS Applied Materials & Interfaces*, Online published. 2015

2. **Hyun-Sub Shim**, Francis Lin, Jihun Kim, Bomi Sim, Tae-Min Kim, Chang-Ki Moon, Chun-Kai Wang, Yongsok Seo, Ken-Tsung Wong, and Jang-Joo Kim, Efficient Vacuum-Deposited Tandem Organic Solar Cells with Fill Factors Higher Than Single-Junction Subcells, *Advanced Energy Materials*, 5, 1500228, 2015.

3. Min-Soo Choi, Tae-Min Kim, **Hyun-Sub Shim**, Beom-Soo Kim, Hyo Jung Kim, and Jang-Joo Kim, Enhancement of the Fill Factor through an Increase of the Crystallinity in Fullerene-Based Small-Molecule Organic Photovoltaic Cells, *ACS Applied Materials & Interfaces*, 7, 9134, 2015.

4. Beom-Soo Kim, Tae-Min Kim, Min-Soo Choi, **Hyun-Sub Shim**, Jang-Joo Kim, Fully Vacuum-Processed Perovskite Solar Cells with High Open Circuit Voltage Using MoO_3/NPB as Hole Extraction Layers, *Organic Electronics*, 17, 102 2015.

5. Dae-Ho Kim, Kyu-Sik Kim, **Hyun-Sub Shim**, Chang-Ki Moon, Yong Wan Jin, and Jang-Joo Kim, A High Performance Semitransparent Organic Photodetector with Green Color Selectivity, *Applied Physics Letters*, 105,

213301, 2014.

6. **Hyun-Sub Shim**, Jung-Hung Chang, Chih-I. Wu, Jang-Joo Kim, Effect of Different *p*-dopants in an Interconnection Unit on the Performance of Tandem Organic Solar Cells, *Organic Electronics*, 15, 1805, 2014.

7. Jihun Kim†, **Hyun-Sub Shim**†, Horim Lee, Min-Soo Choi, Jang-Joo Kim, and Yongsok Seo, Highly Efficient Vacuum-Processed Organic Solar Cells Containing Thieno[3,2-b]thiophene-thiazole, *The Journal of Physical Chemistry C*, 118, 11559, 2014 (†equal contribution).

8. Tae-Min Kim, Hyo Jung Kim, **Hyun-Sub Shim**, Min-Soo Choi, Ji Whan Kim and Jang-Joo Kim, The Epitaxial Growth of Lead Phthalocyanine on Copper Halogen Compounds as the Origin of Templating Effects, *Journal of Materials Chemistry A*, 2, 8730, 2014.

9. Tae-Min Kim, **Hyun-Sub Shim**, Min-Soo Choi, Hyo Jung Kim and Jang-Joo Kim, Multilayer Epitaxial Growth of Lead Phthalocyanine and C_{70} Using CuBr as a Templating Layer for Enhancing the Efficiency of Organic Photovoltaic Cells, *ACS Applied Materials & Interfaces*, 6, 4286, 2014.

10. **Hyun-Sub Shim**, Jung-Hung Chang, Seung-Jun, Yoo Chih-I Wu, Jang-Joo Kim, Correlation of the Electronic Structure of an Interconnection Unit with the Device Performance of Tandem Organic Solar Cells, *Journal of Materials Chemistry A*, 2, 5450, 2014.

11. **Hyun-Sub Shim**, Sei-Yong Kim, Ji Whan Kim, Tae-Min Kim, Chang-

Heon Lee, Jang-Joo Kim, An Efficient Interconnection Unit Composed of Electron-Transporting Layer/Metal/*p*-doped Hole-transporting Layer for Tandem Organic Photovoltaics, *Applied Physics Letters*, 102, 203903, 2013.

12. Sei-Yong Kim, Jeong-Hwan Lee, **Hyun-Sub Shim** and Jang-Joo Kim, Optical Analysis of Organic Photovoltaic Cells Incorporating Graphene as a Transparent Electrode, *Organic Electronics*, 14, 1496 , 2013.

13. Tae-Min Kim[+], Ji Whan Kim[+], **Hyun-Sub Shim** and Jang-Joo Kim, High Efficiency and High Photo-Stability Zinc-Phthalocyanine Based Planar Heterojunction Solar Cells with a Double Interfacial Layer, *Applied Physics Letter*, 101, 113301, 2012.

14. Hyo Jung Kim, **Hyun-Sub Shim**, Ji Whan Kim, Hyun Hwi Lee and Jang-Joo Kim, CuI Interlayer in Lead Phthalocyanine Thin Films Enhance Near-Infrared Light Absorption, *Applied Physics Letter* 100, 263303, 2012.

15. Won-Ik Jeong, Yang Eun Lee, **Hyun-Sub Shim**, Tae-Min Kim, Sei-Yong Kim and Jang-Joo Kim, Photoconductivity of C_{60} as an Origin of Bias-Dependent Photocurrent in Organic Photovoltaics, *Advanced Functional Materials*, 22, 3089, 2012.

16. **Hyun-Sub Shim**, Hyo Jung Kim, Ji Whan Kim, Sei-Yong Kim, Won-Ik Jeong, Tae-Min Kim and Jang-Joo Kim, Enhancement of Near-Infrared Absorption with High Fill Factor in Lead Phthalocyanine-Based Organic Solar Cells, *Journal of Materials Chemistry*, 22, 9077, 2012.

List of Presentations

International conference

1. **Hyun-Sub Shim**, Chang-Ki Moon, Jihun Kim, Chun-Kai Wang, Bomi Sim, Francis Lin, Ken-Tsung Wong, Yongsok Seo, Jang-Joo Kim, Efficient vacuum-deposited ternary organic solar cells with borad absorption, energy transfer and enhanced hole mobility, The 7th International Workshop on Flexible & Printable Electronics 2015 (IWFPE 2015), November 4-6, 2015, Korea.

2. Min-Soo Choi, Tae-Min Kim, **Hyun-Sub Shim**, Beom-Soo Kim, Hyo Jung Kim, and Jang-Joo Kim, Enhancement of fill factor through increase of crystallinity in fullerene based small molecule organic photovoltaic cells, The 7th International Workshop on Flexible & Printable Electronics 2015 (IWFPE 2015), November 4-6, 2015, Korea.

3. Beom-Soo Kim, Tae-Min Kim, Min-Soo Choi, **Hyun-Sub Shim**, Jang-Joo Kim, Fully vacuum co-deposited CH3NH3PbI3 perovskite solar cell with 1.12 V of circuit voltage employing MoO3/NPB layers as a hole transport layers, The 7th International Workshop on Flexible & Printable Electronics 2015 (IWFPE 2015), November 4-6, 2015, Korea.

4. **Hyun-Sub Shim**, Francis Lin, Jihun Kim, Bomi Sim, Tae-Min Kim, Chang-Ki Moon, Yongsok Seo, Chun-Kai Wang, Ken-Tsung Wong, Jang-Joo Kim, Efficient vacuum-deposited tandem organic solar cells with fill factor higher than single junction subcells, KJF 2015, September 6-9, 2015,

Jeju, Korea.

5. Min-Soo Choi, Tae-Min Kim, **Hyun-Sub Shim**, Beom-Soo Kim, Hyo Jung Kim, and Jang-Joo Kim, Enhancement of fill factor through increase of crystallinity in fullerene based small molecule organic photovoltaic cells, KJF 2015, September 6-9, 2015, Jeju, Korea.

6. Beom-Soo Kim, Tae-Min Kim, Min-Soo Chol, **Hyun-Sub Shim** and Jang-Joo Kim, Fully vacuum-processed CH3NH3Pb3I3 perovskite solar cells with high open circuit voltage using MoO3/NPB layer, KJF 2015, September 6-9, 2015, Jeju, Korea.

7. Dae-Ho Kim, Kyu-Sik Kim, **Hyun-Sub Shim**, Chang-Ki Moon, Yong Wan Jin, Jang-Joo Kim, A high performance semitransparent organic photodetector with green color selectivity using 1,4,5,8,9,11-hexaazatriphenylenehexacarbonitrile as an organic buffer layer, SPIE Optics+Photonics 2015, August 9-13, 2015, San Diego, USA.

8. **Hyun-Sub Shim**, Francis Lin, Jihun Kim, Bomi Sim, Tae-Min Kim, Chang-Ki Moon, Yongsok Seo, Chun-Kai Wang, Ken-Tsung Wong, Jang-Joo Kim, Efficient vacuum-deposited tandem organic solar cells with fill factor higher than single junction subcells, SPIE Optics+Photonics 2015, August 9-13, 2015, San Diego, USA.

9. Dae-Ho Kim, Kyu-Sik Kim, **Hyun-Sub Shim**, Chang-Ki Moon, Yong Wan Jin, and Jang-Joo Kim, A high performance semitransparent organic photodetector with green color selectivity using 1,4,5,8,9,11-hexaazatriphenylenehexacarbonitrile as an organic buffer layer, 26th

International Conference on Molecular Electronics and Devices (IC ME&D 2015), May 21-22, 2015, Korea.

10. Min-Soo Choi, Tae-Min Kim, **Hyun-Sub Shim**, Beom-Soo Kim, Hyo Jung Kim, and Jang-Joo Kim, Enhancement of fill factor through increase of crystallinity in fullerene based small molecule organic photovoltaic cells, 26th International Conference on Molecular Electronics and Devices (IC ME&D 2015), May 21-22, 2015, Korea.

11. Beom-Soo Kim, Tae-Min Kim, Min-Soo Choi, **Hyun-Sub Shim** and Jang-Joo Kim, Fully vacuum-processed CH3NH3Pb3I3 perovskite solar cells with high open circuit voltage using MoO3/NPB layer, International Conference on Hybrid and Organic Photovoltaics 2015 (HOPV15), May 10-13, 2015, Italy.

12. Min-Soo Choi, Tae-Min Kim, **Hyun-Sub Shim**, Beom-Soo Kim and Jang-Joo Kim, Enhancement of Fill Factor via Increase of Crystallinity in Fullerene Based Small Molecule Organic Photovoltaic Cells Using Copper Iodide as a Templating Layer, The 6th Asian Conference on Organic Electronics (A-COE 2014), November 12-14, 2014, Taiwan.

13. Beom-Soo Kim, Tae-Min Kim, Min-Soo Choi, **Hyun-Sub Shim** and Jang-Joo Kim, Fully-Vacuum Processed Perovskite Solar Cells with High Open Circuit Voltage Using MoO3/NPB Layers, The 6th Asian Conference on Organic Electronics (A-COE 2014), November 12-14, 2014, Taiwan.

14. **Hyun-Sub Shim**, Jung-Hung Chang, Seung-Jun Yoo, Chih-I Wu, and Jang-Joo Kim, An efficient interconnection unit composed of electron-

transporting layer/metal/*p*-doped hole transporting layer and its operation mechanism in tandem organic solar cells, SPIE Optics+Photonics 2014, Aug 17-21, 2014, San Diego, USA.

15. Tae-Min Kim, **Hyun-Sub Shim**, Min-Soo Choi, Hyo Jung Kim and Jang-Joo Kim, Multi-layer Epitaxial Growth of Lead-Phthalocyanine and C70 Using CuBr as a Templating Layer for Enhancing the Efficiency of Organic Photovoltaic Cells, 10th International Conference on Electroluminescence and Organic Optoelectronics (ICEL), August 31-September 3, 2014, Germany.

16. **Hyun-Sub Shim**, Sei-Yong Kim, Ji Whan Kim, Tae-Min Kim, Chang-Heon Lee, Jang-Joo Kim, An efficient interconnection unit composed of electron-transporting layer/metal/*p*-doped hole-transporting layer for tandem organic photovoltaics, 2014 Korea-Germany IRTG Symposium, February 17-22, 2014, Korea.

17. **Hyun-Sub Shim**, Jung-Hung Chang, Seung-Jun Yoo, Chih-I Wu, and Jang-Joo Kim, An efficient interconnection unit composed of electron-transporting layer/metal/*p*-doped hole transporting layer and its operation mechanism in tandem organic solar cells, The 5th International Workshop on Flexible & Printable Electronics 2013 (IWFPE 2013), November 20-22, 2013, Korea.

18. Tae-Min Kim, **Hyun-Sub Shim**, Min-Soo Choi, and Jang-Joo Kim, Multi-layer epitaxial growth of lead-phthalocyanine and C70 using CuBr as a templating layer for the efficiency enhancement of organic photovoltaic

cells, 5th Asian Conference on Organic Electronics (A-COE 2013), November 13-15, 2013, Korea.

19. **Hyun-Sub Shim**, Jung-Hung Chang, Chih-I Wu, and Jang-Joo Kim, An efficient interconnection unit composed of electron-transporting layer/metal/*p*-doped hole transporting layer and its operation mechanism in tandem organic solar cells, 5th Asian Conference on Organic Electronics (A-COE 2013), November 13-15, 2013, Korea.

20. Tae-Min Kim, **Hyun-Sub Shim**, Min-Soo Choi, and Jang-Joo Kim, Heteroepitaxial growth of lead-phthalocyanine and C70 using CuBr as a templating layer for the efficieny enhancement of organic photovoltaic cells, IRTG 2013 (8th German-Korean Polymer Symposium), August 26-29, 2013, Germany.

21. **Hyun-Sub Shim**. Sei-Yong Kim, Ji Whan Kim, Tae-Min Kim, Chang-Heon Lee, and Jang-Joo Kim, An efficient interconnection unit composed of electron-transporting layer/metal/*p*-doped hole transporting layer for tandem organic photovoltaics, IRTG 2013 (8th German-Korean Polymer Symposium), August 26-29, 2013, Germany.

22. Won-Ik Jeong, Yang-Eun Lee, **Hyun-sub Shim**. Tae-Min Kim, Sei-Yong Kim, Jang-Joo Kim, Photoconductivity of C60 as an Origin of Bias-Dependent Photocurrent in Organic Photovoltaics, IRTG 2013, February 25-28, 2013, Korea.

23. **Hyun-Sub Shim**, Hyo Jung Kim, Ji Whan Kim, Sei-Yong Kim, Won-Ik Jeong, Tae-Min Kim and Jang-Joo Kim, Near-infrared absorbing small

molecular organic solar cells, The 8th TU-UT-SNU-TJU Student Workshop, October 17-20, 2012, China.

24. Tae-Min Kim, Ji Whan Kim, **Hyun-Sub Shim**, Jang-Joo Kim, High efficiency and high photo-stability zinc-phthalocyanine based planar heterojunction solar cells with a double interfacial layer, ILCC 2012, August 19~24, 2012, Germany.

25. Tae-Min Kim, Ji Whan Kim, **Hyun-Sub Shim**, Jang-Joo Kim, High efficiency and high photo-stability zinc-phthalocyanine based planar heterojunction solar cells with a double interfacial layer, 2nd ENGE 2012, September. 17, 2012, Korea.

26. **Hyun-Sub Shim**, Hyo Jung Kim, Ji Whan Kim, Sei-Yong Kim, Won-Ik Jeong, Tae-Min Kim and Jang-Joo Kim, Enhancement of Near-Infrared absorption with high fill factor in lead phthalocyanine based organic solar cells, IMID 2012, August. 28, 2012, Korea.

27. **Hyun-Sub Shim**, Jang-Joo Kim, Hyo Jung Kim, Ji Whan Kim, Sei-Yong Kim, Won-Ik Jeong, Tae-Min Kim, Enhanced sensitivity to near-infrared with high fill factor in small molecular organic solar cells, SPIE 2012, August 12 2012, USA.

28. Tae-Min Kim, Ji Whan Kim, **Hyun-Sub Shim** and Jang-Joo Kim, High Efficiency and high photo-stability zinc-phthalocyanine based planar heterojunction solar cells with a double interfacial layer, MRS 2012, April 12, 2012, USA.

29. Tae-Min Kim, Ji Whan Kim, **Hyun-Sub Shim** and Jang-Joo Kim, High efficiency and high photo-stability zinc-phthalocyanine based planar heterojunction solar cells with a double interfacial layer, The 3rd Asian Conference on Organic Electronics, November. 4-6, 2011, Taiwan.

Domestic conference

1. Min-Soo Choi, Tae-Min Kim, **Hyun-Sub Shim**, Beom-Soo Kim, Hyo Jung Kim, and Jang-Joo Kim, Enhancement of fill factor through an increase of crystallinity in fullerene-based small molecule organic photovoltaic cells, 2015 Materials Fair, October 1, 2015, Korea.

2. 최민수, 김태민, **심현섭**, 김범수, 김효정, 김장주, Enhancement of fill factor via increase of crystallinity in fullerene based small molecule organic photovoltaic cells using copper iodide as a templating layer, 2015 한국고분자학회 춘계학술대회, April 8-10 (April 9), 2015, Korea.

3. 김범수, 김태민, 최민수, **심현섭**, 김장주, Fully vacuum-processed perovskite solar cells with V_{OC} of 1.12 V employing MoO3/NPB layer, 2015 한국고분자학회 춘계학술대회, April 8-10 (April 9), 2015, Korea.

4. 김대호, 김규식, **심현섭**, 문창기, 진용완, 김장주, A high performance semitransparent organic photodetector with green color selectivity using an organic buffer layer, 2015 한국고분자학회 춘계학술대회, April 8-10 (April 9), 2015, Korea.

5. **심현섭**, Jung-Hung Chang, 유승준, Chih-I Wu, 김장주, An efficient

interconnection unit composed of electron-transporting layer/metal/*p*-doped hole transporting layer and its operation mechanism in tandem organic solar cells, 2014 Materials Fair, September 25, 2014, Korea.

6. **Hyun-Sub Shim**, Jung-Hung Chang, Seung-Jun Yoo, Chih-I Wu and Jang-Joo Kim, An efficient interconnection unit composed of electron-transporting layer/metal/*p*-doped hole-transporting layer and its operation mechanism in tandem organic solar cells, 2014 Joint Symposium of Korean Society of Photoscience - Korea Organic Solar Cell Society, Jun 20-21, 2014, Korea.

7. Tae-Min Kim, **Hyun-Sub Shim**, Min-Soo Choi, Hyo Jung Kim and Jang-Joo Kim, Multilayer Epitaxial Growth of Lead Phthalocyanine and C70 Using CuBr as a Templating Layer for Enhancing the Efficiency of Organic Photovoltaic Cells, 2014 Joint Symposium of Korean Society of Photoscience - Korea Organic Solar Cell Society, Jun 20-21, 2014, Korea.

8. 심현섭, 김효정, 김지환, 김세용, 정원익, Enhancement of near-infrared absorption with high fill factor in lead phthalocyanine-based organic solar cells, 2013 한국고분자학회 춘계학술대회, April 11-12, 2013, Korea.

9. 김태민, 김지환, 심현섭, 김장주 High efficiency and high photo-stability zinc-phthalocyanine based planar heterojunction solar cells with a double interfacial layer, 2013 한국고분자학회 춘계학술대회, April 11-12, 2013, Korea.

10. Won-Ik Jeong, Yang Eun Lee, **Hyun-Sub Shim**, Tae-Min Kim, Sei-Yong Kim and Jang-Joo Kim, Photoconductivity of C_{60} as an origin of bias-dependent photocurrent in organic photovoltaics, 한국 유기태양전지학회 2012 하계 심포지엄, June 27, 2012, Korea.

11. Tae-Min Kim, Ji Whan Kim, **Hyun-Sub Shim** and Jang-Joo Kim, High efficiency and high photo-stability zinc-phthalocyanine based planar heterojunction solar cells with a double interfacial layer, 한국 유기태양전지학회 2012 하계 심포지엄, June 27, 2012, Korea.

12. Won-Ik Jeong, Yang Eun Lee, **Hyun-Sub Shim**, Tae-Min Kim, Sei-Yong Kim, Jang-Joo Kim, Photoconductivity of C_{60} as an origin of bias dependent photocurrent in organic photovoltaics, 제17회 유기태양전지 심포지엄, Dec. 15-16, 2011, Korea.

13. 정원익, 김태민, **심현섭**, 이양은, 김세용, 김장주, Bias dependent photocurrent originated from the photoconductivity of C_{60} in organic photovoltaics, 2011 한국태양광학술대회 및 제 6회 한중일 태양광발전 국제공동 심포지움, Sep. 28-30, 2011, Korea.

14. **심현섭**, 김태민, 김장주, The effect of buffer layer in small molecular near-infrared photodetector, 2011 한국고분자학회 춘계 학술대회, April 7-8, 2011, Korea.

List of Patents

1. 김장주, **심현섭**, 연결 유닛을 포함하는 적층형 유기태양전지, 출원번호 10-2014-0044799, 등록번호 10-1534767 (2015.07.01)

2. Jang-Joo Kim and **Hyun-Sub Shim**, STACKED ORGANIC SOLAR CELL INCLUDING INTERCONNECTION UNIT, PCT/KR2014/003284 (2014.04.16)